Dissertation

submitted to the
Combined Faculties for the Natural Sciences and for Mathematics
of the Ruperto-Carola University of Heidelberg, Germany
for the degree of
Doctor of Natural Sciences

presented by

Diplom-Physicist Ilaria Pascucci
born in: Pesaro, Italy

Oral examination: 26$^{\text{th}}$ May 2004

Massive Star Formation at High Spatial Resolution

Referees: **Prof. Dr. Thomas Henning**
Prof. Dr. Wolfgang Duschl

Zusammenfassung

Thema der Dissertationsschrift ist die Frühphase der Entstehung massereicher Sterne sowie deren Einfluss auf ihre Umgebung. Weiterhin wird die Anwendung von Kontinuumsstrahlungstransportsimulationen zur Interpretation der Beobachtungsdaten untersucht. Die wichtigsten Ergebnisse der Arbeit sind: 1) Die Beziehung zwischen heissen Molekülwolkenkernen und ultrakompakten HII-Gebieten wurde für zwei Sternenstehungsgebiete untersucht. Die thermische Strahlung der ultrakompakten HII-Gebieten konnte räumlich aufgelöst und Der Spektraltyp der jeweiligen Ionisationsquelle bestimmt werden. Die heissen Molekülwolkenkernen konnten nicht entdeckt werden, sodass sich eine Extinktion von mehr als 200 Größ-enklassen im Sichtbaren abschätzen lässt. 2) Zum ersten mal konnte mit Hilfe interferometrischer Beobachtungen im thermischen Infrarot die Strahlung von Scheiben um massereiche junge Sterne auf Skalen von 30-50 AU aufgelst werden. Die Visibility-Kurve unterscheidet sich dabei von Sternen mittlerer Masse. 3) Die nähere Umgebung des Sterns Θ^1 C Ori wurde mit dem Adaptive-Optik-Instrument NACO abgebildet. Die Doppelscheibe Orion 168-326 wurde räumlich aufgelöst. Auch wurde die einzige voll in Aufsicht erscheinende Proplyd entdeckt. 4) Der erste Leistungsvergleich für zwei-dimenisonale Strahlungstransport-Programme wurde durchgeführt. Dazu wurden fünf Strahlungstransport-Programme an einer Scheibenkonfiguration getestet und die Ergebnisse miteinander verglichen. Für eine deformierte Scheibe wurde Bilder und die Visibilities erzeugt. Schliesslich wurden die Parameterbereiche untersucht, bei denen eine Deformation einer Scheibe mit MIDI detektierbar wäre.

Abstract

This thesis studies the early phases of massive stars and their impact on the surrounding. The capabilities of continuum radiative transfer (RT) codes to interpret the observations are also investigated. The main results of this work are: 1) Two massive star-forming regions are observed in the infrared. The thermal emission from the ultra-compact H II regions is resolved and the spectral type of the ionizing stars is estimated. The hot cores are not detected thus implying line-of-sight extinction larger than 200 visual magnitude. 2) The first mid-infrared interferometric measurements towards a young massive star resolve thermal emission on scales of 30-50 AU probing the size of the predicted disk. The visibility curve differs from those of intermediate-mass stars. 3) The close vicinity of Θ^1 C Ori are imaged using the NACO adaptive optics system. The binary proplyd Orion 168-326 and its interaction with the wind from Θ^1 C Ori are resolved. A proplyd uniquely seen face-on is also identified. 4) Five RT codes are compared in a disk configuration. The solutions provide the first 2D benchmark and serve to test the reliability of other RT codes. The images/visibilities from two RT codes are compared for a distorted disk. The parameter range in which such a distortion is detectable with MIDI is explored.

Contents

Chapter 1

Introduction

Although the formation and evolution of massive stars occur on short timescales (about 1–10 Myr), their impact on the interstellar medium and on the evolution of the galaxies as a whole is profound. While still accreting, massive protostars begin burning their nuclear fuel and emit enormous amount of ultraviolet radiation that initiates chemical reactions in their surroundings leading to complex molecules. In the course of time, their powerful stellar winds destroy the natal molecular cloud and regulate the formation of new stars. At the end of their life, massive stars die violently and enrich the interstellar medium with metals that could not be produced in the early Universe.
In spite of their importance, our understanding of the formation and early phases of high-mass stars is still rather limited. Accessing young massive stars is made difficult by their larger distances in comparison to low-mass stars, their fast evolution in heavily obscured dust cocoons and their tendency to form in clusters.
It is the aim of this thesis to investigate massive (proto)stars and their surroundings by means of observing techniques able to attain high sensitivity and high spatial resolution. Such observations provide firm basis for modeling and understanding the close vicinity of massive stars.

1.1 From hot molecular cores to classical H II regions

In this section, we summarize the current knowledge on the main phases of massive star formation. For a more complete picture we refer to Garay and Lizano (1999).
The formation of high-mass stars begins in massive clumps ($> 10^3\,M_\odot$) within Giant Molecular Clouds (Elmegreen 1991). Gravitational instabilities and turbulence may lead to gravitationally bound dense cores, that eventually collapse at the free-fall rate. It is expected, but never observed, that the gravitational collapse rapidly builds up a massive protostar. Although the formation of the massive protostars is not understood, observations have identified the probable next stage in the form of hot molecular cores (HMCs).
Hot molecular cores have been defined by Kurtz et al. (2000) as molecular cloud cores having diameters smaller than 0.1 pc, densities larger than $10^7\,cm^{-3}$ and temperatures above 100 K, much larger than in the surrounding dense material cloud. Observationally, they are characterized by the presence of complex and rare molecular species, many of which can only form in gas phase reactions from grain mantle species (Charnley 1995). Based on the only twenty objects classified as HMCs and assuming a massive star formation rate of $10^{-2}\,yr^{-1}$ in our

galaxy, the lifetime of HMCs is expected be less than 10^4 yr (Kurtz et al. 2000). The key question in confirming the HMCs as the stage following the gravitational collapse is to prove that massive protostars have formed inside them. Currently, there are two approaches to this challenge: One is to identify massive outflows and circumstellar disks in the HMCs (see e.g. Sridharan et al. 2002; Beltrán et al. 2004); The other is to show that HMCs are internally heated (e.g. De Buizer et al. 2003).

As soon as the massive protostar reaches the main sequence, its copious amount of Lyman continuum radiation ionizes its surrounding (Strömgren 1939). This phase, in which newly born massive stars are surrounded by a compact (diameters ≤ 0.1 pc), dense (electron densities $\geq 10^4$ cm^{-3}) bubble of ionized gas, is easily identified in the radio continuum and is referred to as *ultra-compact H II region*. The transition from hot cores to ultra-compact H II regions is a much disputed and poorly known process (Kurtz et al. 2000). In contrast, the ultracompact H II phase has been studied in detail: their morphology, main properties and distribution in the Milky Way have been largely investigated by interferometric radio surveys with the Very Large Array Telescope (e.g. Wood and Churchwell 1989; Garay et al. 1993; Kurtz et al. 1994).

In about 10^5 yr the ionized gas expands and reaches the pressure equilibrium with the ambient neutral medium (Dyson and Williams 1980). By this time, the ultra-compact H II regions have expanded typically to a hundred times of their original sizes and their densities have dropped by a similar factor (for a comparison of properties of H II regions see e.g. Table 1 from Kurtz and Franco 2002). The lower extinction towards these more extended ionized regions, also known as *classical H II regions*, usually allows the optical identification of the massive stars within them. The most famous example for this class of objects is the Orion Nebula.

1.2 Observational strategy and tools

The difficulties in exploring the young massive stars are their large distances and extinction and their tendency to form in complex environment. Thus, observationally addressing the unanswered questions about their formation requires high angular resolution, high sensitivity and capability of correctly modeling the observational results.

The infrared regime is a natural choice to penetrate the hundreds of magnitudes of visual extinction that usually characterize the early phases. The recent development of infrared observations allow sensitive single-dish measurements at the level of few milli-Janskies even from ground-based telescopes (Apai et al. 2002). Adaptive optics techniques are successful in overcoming the resolution limit imposed by atmospheric turbulence and allow reaching the diffraction limit at near-infrared wavelengths (e.g. Rousset et al. 2003). Long-baseline interferometry in the infrared regime provides less sensitive measurements but angular resolutions at least ten times better than the best single-dish imaging (e.g. Leinert et al. 2003a). Such a high resolution is sufficient to directly probe the spatial scales at which massive disks are expected (Yorke and Sonnhalter 2002).

Interpreting complex environments requires also careful modeling. Especially in the case of dust-enshrouded objects, the correct interpretation of their observables (spectral energy distributions, visibilities, intensity and polarization maps) requires detailed calculations of the photon transport. Such calculations can only be done by developing sophisticated radiative transfer (RT) codes that solve the RT equation numerically (e.g. Henning 2001). Validating

multi-dimensional radiative transfer codes is a prerequisite for understanding young massive stars and the environment in which they form.

1.3 Outline

This thesis focuses on the study of the early phases of massive star formation and on the impact that massive stars have on their surroundings. Emphasis is also on the development of reliable tools to interpret upcoming high-resolution observations of the immediate vicinity of young massive stars.
Chapter 2 presents our infrared campaign toward two massive star-forming regions aiming to identify the early embedded massive (proto)stars. We investigate the relation between hot molecular cores and ultra-compact H II regions. The possibility that hot cores are internally heated and thus represent the precursors of ultra-compact H II regions is studied by detecting their thermal dust emission. These observations demonstrate the importance of high angular resolution to disentangle the usually crowded regions where massive stars are born.
Aiming to resolution unachievable even with the largest single-dish telescopes, in Chapter 3 we introduce the new mid-infrared instrument for the Very Large Telescope Interferometer. We present the first mid-infrared interferometric observations of a young massive B0 type star aiming to detect and characterize the predicted circumstellar disk around it. Our interferometric data resolve the thermal dust emission at scales smaller than 50 AU. Constraining the geometry of the circumstellar material will require other visibility measurements and detailed radiative transfer simulations.
The impact of massive stars on their surroundings is discussed in Chapter 4 on the example of Θ^1 C Ori in the Orion Nebula. We present high-resolution near-infrared images that show in great detail how the strong ultraviolet radiation and wind from Θ^1 C Ori shape the dust and gas envelopes of nearby young low-mass stars. The nature of numerous sources identified close to the massive star is discussed in detail.
In Chapter 5 we explore the current capabilities of continuum radiative transfer codes in modeling circumstellar disks. By comparing the output of five different codes for a set of well-defined problems we provide the first benchmark tests and solutions for disk configurations. This work has key importance for the verification of radiative transfer codes and for their correct use in modeling observations. In the last section of this chapter, we show how radiative transfer codes can be used to predict and interpret interferometric observations on the example of a simulated circumstellar disk distorted by disk/star encounters.
The last Chapter summarizes the main results of this work and future prospects.

Chapter 2

Young Embedded Massive Stars

In this Chapter, we demonstrate the capabilities of mid-infrared (MIR) imaging and spectroscopy in identifying the early embedded phases of massive star formation. We focus on hot molecular cores (HMC), ultra-compact H II (UCH II) regions and on their relation.
Sub-arcsecond maps of molecular transitions towards HMCs found only in three cases convincing evidence of internally heated and centrally dense cores as expected from the cloud core collapse: These are the HMCs in G31.41+0.31 and G29.96-0.02 (Watt et al. 1999; Maxia et al. 2001) and the prototype of HMCs in Orion (Kaufman et al. 1998; de Vicente et al. 2002). The case of G34.26+0.15 points towards a completely different scenario in which the HMC is externally heated by interaction with the nearby cometary UCH II region (Watt and Mundy 1999).
A different approach to unveil embedded massive protostars is to detect thermal emission from the surrounding dust. Very recently a number of groups tried to detect the MIR counterparts of HMCs (Stecklum et al. 2002; De Buizer et al. 2003; Linz et al. 2003). These studies demonstrated the importance of establishing a reliable and precise astrometry to correctly interpret the infrared data. Due to the lack of MIR sources with near-infrared/visible counterparts, the astrometry of MIR images is often set by the telescope pointing accuracy (typically a couple of arcseconds) or by using the location and the morphology of radio sources and/or maser sites whose connection with the MIR emission is not yet clarified. Up to now, only three out of nine HMC candidates have been detected in the mid-infrared regime (De Buizer et al. 2002; Stecklum et al. 2002; De Buizer et al. 2003).
In the following, we present infrared imaging and spectroscopy of the two complex high-mass star-forming regions G10.47+0.03 and W3(OH). First, we discuss G10.47+0.03 where three UCH II regions are found to be still embedded in the HMC (Sect. 2.1). Here, particular importance is given to establishing a reliable astrometric frame (Sect. 2.3). The second region W3(OH) harbours a hot molecular core well separated from the UCH II region and is discussed in Sects. 2.7–2.11.

2.1 Ultra-compact H II regions embedded in hot cores

G10.47+0.03 represents a promising site to search for the connection between the HMC and the UCH II phases: Four UCH II regions have been detected at radio wavelengths (Wood and Churchwell 1989, hereafter WC89 and Cesaroni et al. 1998, hereafter CHWC98), three of them are found to be still embedded in the HMC traced by ammonia and methyl cyanide emission

(CHWC98, Olmi et al. 1996a). Many other complex molecular species (Olmi et al. 1996b; Hatchell et al. 1998; Wyrowski et al. 1999a) and strong maser emission of OH, CH_3OH and H_2O (Caswell et al. 1995; Hofner and Churchwell 1996; Walsh et al. 1998) have been detected towards the region of the HMC and the embedded UCH II regions. Recent interferometric millimeter observations show that the emission of a clump of cold dust peaks at the location of the two most embedded UCH II regions (Gibb et al. 2002).

Based on astrometric accuracy at the level of $0\farcs3$, we aim to study in detail the relationship between the UCH II regions, the HMC and the MIR emission from G10.47+0.03. In our discussion we adopt a distance of 5.8 kpc for the massive star-forming region, as determined by Churchwell et al. (1990) from their measured ammonia velocity and the rotation curve of Brand (1986). In Sect. 2.2 we describe the observations and data reduction. Two independent methods are considered to establish the astrometric reference frame of our mid-infrared images (Sect. 2.3). The results and their interpretation are presented in Sects. 2.4 and 2.5. Our findings are summarized in Sect. 2.6.

2.2 Observations of G10.47+0.03 and data reduction

The mid-infrared observations presented in this thesis were obtained at different wavelengths and with different instruments. An additional Ks image was taken at the Very Large Telescope with the ISAAC camera to calibrate the astrometry of our MIR images. The 1 σ sensitivities of the different observations are collected in Table 2.1.

2.2.1 SpectroCam10 imaging

The first observations were carried out in June 1999 using SpectroCam–10 (Hayward et al. 1993), the 10 μm spectrograph and camera for the 5-m Hale telescope[1]. SpectroCam–10 is optimized for wavelengths from 8 to 13 μm and has a Rockwell 128×128 Si:As Back Illuminated Blocked Impurity Band (BIBIB) detector with a plate scale of $0\farcs25$ per pixel. In imaging mode the unvignetted field of view is $15''$.

During the observations, we applied filters with central wavelengths at 8.8, 11.7, and 17.9 μm and bandwidths of 1 μm. We used the chopping/nodding technique with a chopper throw of $20''$ in north-south direction. The 11.7 μm field has been slightly enlarged by observing at 3 different positions: the first one centered on the radio source (WC89), and the other two positions offset by few arcseconds. The total on-source integration time amounts to 5, 8, and 3 minutes for the 8.8, 11.7, and 17.9 μm filters, respectively. The source δ Oph has been observed immediately after our target and we use it as reference star for the flux calibration (fluxes are taken from Cohen et al. 1999).

The data reduction was performed using self-developed IDL scripts in the standard fashion: the off–source beams of the chopping and nodding were used to remove the sky background and its gradients. We also improved our signal-to-noise ratio by applying the wavelet filtering algorithm of Pantin and Starck (1996), a flux-conservative method useful to search for faint extended emission.

[1]Observations at the Palomar Observatory made as part of a continuing collaborative agreement between the California Institute of Technology and Cornell University.

Table 2.1: 1 σ sensitivities of the different observations in mJy/beam.

Camera	λ [μm]	1 σ [mJy/beam]
SpectroCam-10	8.8	21
	11.7	9
	17.9	1584
TIMMI2(May 2001)	9.8	35
	11.9	8
	12.9	9
	20.0	420
TIMMI2(March 2003)	11.9	6
	12.9	4
	[NeII]	11
ISAAC	2.16	0.017

2.2.2 TIMMI2 imaging

Further mid-infrared observations were performed with the Thermal Infrared Multimode Instrument TIMMI2 mounted on the ESO 3.6m telescope (Relke et al. 2000). TIMMI2 can operate like a spectrograph and imager in the M(5 μm), N(10 μm) and Q(20 μm) atmospheric bandpasses. The detector is a 320×240 Si:As High-Background Impurity Band Conduction array with a pixel scale of $0\farcs2$ in the N and Q imaging modes.
The observations took place in two periods: In May 2001 we imaged the region at 9.8, 11.9, 12.9 and 20.0 μm with total integration times of 7, 22, 9, and 14 minutes, respectively; In March 2003 we obtained deeper images in the 11.9, 12.9 and [NeII] filters for a total on-source time of 36, 36, and 30 minutes. During the first run, chop (north-south) and nod (east-west) throws of $10''$ have been used. In order to enlarge the field of view and thus improve our astrometry (see Sect. 2.3), we applied a larger chop/nod throw of $20''$ during the observations of March 2003. The standard stars HD 169916 and HD 81797 have been used to flux calibrate the data set from May 2001: HD 169916 at the 11.9 and 12.9 μm wavelengths, while HD 81797 for the 9.8 μm and Q the band filters. During the second run, we observed the flux calibrator stars HD 123139 at 11.9 μm and HD 133774 at 12.9 μm and in the [NeII] filter immediately before and after our target. The corresponding flux densities of all the standards are taken from Cohen et al. (1999).
The data reduction was performed as described in Sect. 2.2.1. The 11.9 μm image obtained from the reduction of the March 2003 dataset is shown in Fig. 2.1.

2.2.3 TIMMI2 spectroscopy

N-band spectroscopy of sources II and III (see Fig. 2.1) was obtained with TIMMI2 on 31 May 2003. A slit width of $1\farcs2$ was applied yielding to a resolving power of ∼170 at 10 μm. We used the standard chopping/nodding technique along the slit with a throw of $10''$. The

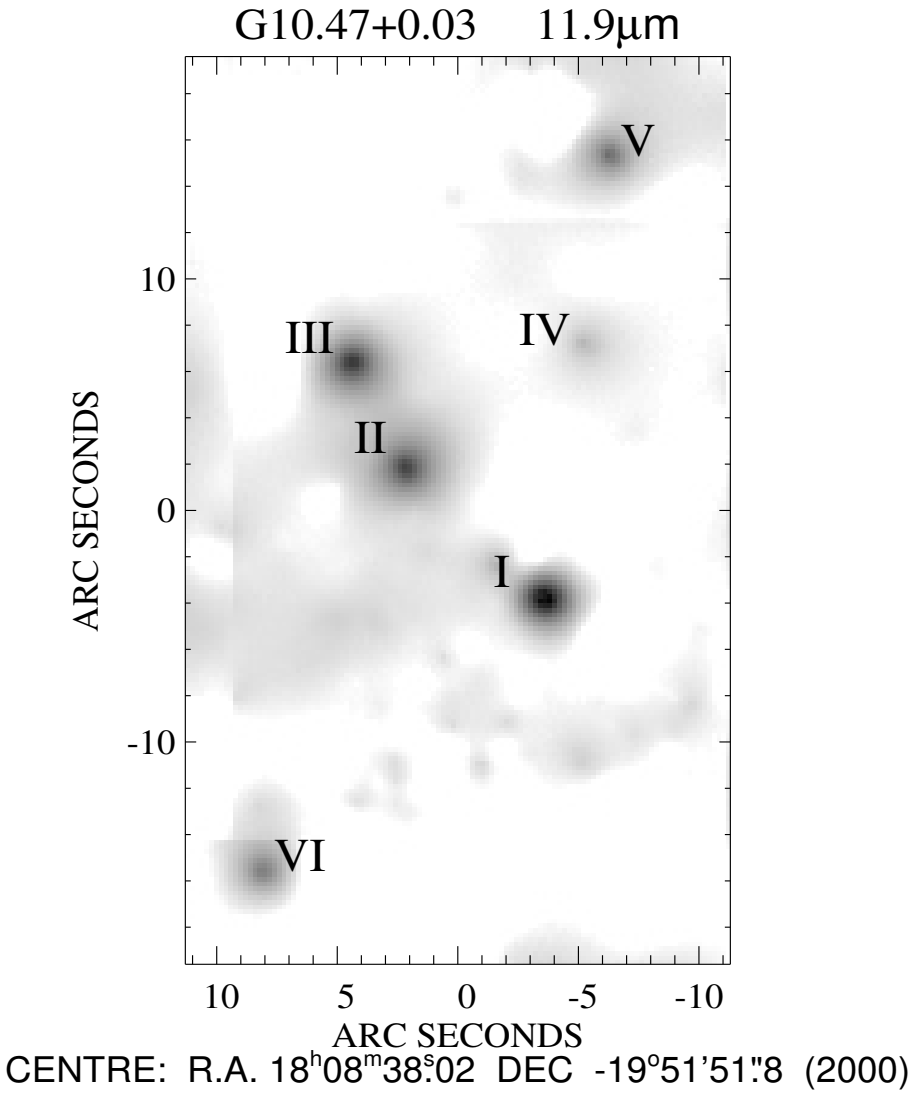

Figure 2.1: TIMMI2 image at 11.9 μm with source labeling. Only the positive beams are shown in the figure. The wavelet filtering algorithm of Pantin and Starck (1996) has been applied to enhance the image quality. Source VII does not belong to the G10.47+0.03 region and is let out of the figure (see Sect. 2.4).

on-source integration time amounted to 43 minutes for object II and 32 minutes for object III. Both sources were observed at an airmass of ∼1.02 during almost photometric conditions. The standard star HD178524 was observed at the same airmass as the targets.
The data reduction was performed using a modified version of the IDL pipeline kindly provided by R. Siebenmorgen (Siebenmorgen et al. 2004). The flux calibration of the spectra was tied to the results of our 12.9 μm measurements with TIMMI2.

2.2.4 ISAAC imaging

We obtained deep Ks-band images using the ISAAC detector mounted on the Antu unit (UT1) of ESO's Very Large Telescope at Cerro Paranal, Chile. The observations took place on the 20th July 2002 in visitor mode in the ESO-programme 69.C-0189(A). The goal of the observations was to establish a reliable astrometric reference frame to align the MIR detections. Therefore only images at the Ks-band were taken. Due to instrumental problems the long wavelength arm (ALADDIN Array) was used. To avoid the saturation of the bright stars in the field, the shortest possible integration time (0.34s) was applied with a five times repetition at each of the 20 positions. The resulting total observational time was approximately 34 seconds. The field of view was $2.5' \times 2.5'$. The observations were conducted at an airmass of 1.3 and a (visual) seeing of $0\farcs75$.
We applied the standard near-infrared (NIR) reduction method to the obtained data as follows: flat fields, bad pixel masking and 'moving sky' subtraction. The photometry of the resulting image has been carried out by placing an aperture with a radius equal to $2\farcs25$ on the individual sources. The flux calibration was performed using the standard star 9149 from Persson et al. (1998) which was observed at the beginning of the night. We checked the resulting photometry on 10 bright stars also present in the 2MASS database. The estimated error on the photometry is 0.1 magnitude.

2.3 Astrometric reference frame for G10.47+0.03

An accurate astrometry is essential to understand the relation between the mid-infrared emission, the HMC and the UCH II regions. Interferometric radio continuum maps have good absolute astrometry, usually at the subarcsecond level[2]. However, since the connection between the radio and MIR emission is unknown, the MIR astrometry should be determined independently from radio measurements.
The detection of up to seven MIR sources in our 11.9 μm image of March 2003 allows us, for the first time, to establish an independent and accurate astrometric reference frame for the HMC and the UCH II regions. Two different approaches have been tested: One approach (Method A) is based on the 2MASS Second Release Point Source Catalogue (PSC); The other approach (Method B) is based on the USNO2 catalogue combined with our Ks ISAAC image. Both approaches provide a consistent astrometry and are briefly described below.

Method A
Three presumably stellar MIR sources, namely I, IV, and V (see Fig. 2.1), have near-infrared

[2]in the case of G10.47+0.03 the error is as small as $0\farcs1$ (Cesaroni private communication)

counterparts in the 2MASS PSC[3] and were used to derive the astrometry of our MIR images. The standard deviation of the difference between the 2MASS coordinates and the location of the three MIR sources is only $0\farcs12$. We compared the 2MASS and USNO2 positions of 24 stars within $2'$ from our target to estimate the local positional accuracy of the 2MASS catalogue. The standard deviation of the position differences is $0\farcs34$. Combining the errors from the 2MASS-MIR and the USNO2-2MASS comparison, we estimate an accuracy of $0\farcs4$ for our 11.9μm image.

Method B
In this method, the ISAAC image provides the transition from the USNO2 catalogue to our 11.9μm image. Within the $2.5'$ large field of the deep ISAAC Ks image, we identified 16 stars which have optical counterparts. Using the USNO2 coordinates we calibrated the astrometry of the ISAAC image with an accuracy of $0\farcs26$. To establish the astrometry of the MIR image we use four objects detected both at near- and mid-infrared wavelengths (sources I, IV, V, and VI in Fig. 2.1). The standard deviation of the differences between the near- and the mid-infrared coordinates is only $0\farcs13$. Thus, the astrometry of our MIR image is accurate within $0\farcs3$. The central $22'' \times 17''$ of our Ks ISAAC image together with the superimposition of the 11.9μm contour and the location of the UCH II regions are shown in Fig. 2.2.

2.4 Main results

2.4.1 Imaging

Seven mid-infrared sources can be identified in our more sensitive 11.9μm image taken during the second TIMMI2 observing run. An overview on the designation is given in Fig. 2.1. Five of the MIR sources are also detected at 12.9μm and in the [NeII] filter. Only the sources from I to IV are present in the smaller field of the Spectro-Cam observations (see Table 2.2). Sources I, IV, V and VI have NIR counterparts and are used to determine the astrometric reference frame of our MIR images (see Sect. 2.3). None of them shows radio emission in the 1.3 cm (CHWC98) and 6 cm (WC89) continuum maps. Source VII is at about $35''$ south-west from the HMC in the G10.47+0.03 region and coincides, within our astrometric accuracy, with the UCH II region G10.46+0.03A.
The most interesting mid-infrared sources are II and III because of their vicinity to a group of UCH II regions (G10.47+0.03A, B1, B2, and C) and to the HMC. They appear marginally extended in [NeII] and in the 12.9μm filters and more extended at 11.9μm. We detect faint emission at this wavelength between the two sources: this "bridge" might be due to the larger extension of the sources at 11.9μm. In Fig. 2.3 we show a cut along the direction connecting the peak positions in two different filters and an additional perpendicular cut for source II.
The UCH II region C is found to have a mid-infrared and a near-infrared counterpart in our images (see Fig. 2.2): The near-infrared, mid-infrared and radio peaks are coincident within our astrometric accuracy (see Sect. 2.3). The 2.16 μm emission is marginally extended and amounts to 0.22 mJy. Assuming a Gaussian profile both for the source (FWHM = $0\farcs67$) and for the beam (FWHM = $0\farcs56$), we calculate a deconvolved FWHM at 2.16 μm of $0\farcs4$ for source III. The MIR emission is more extended, the deconvolved source size amounts to $1\farcs8$ at 11.9 μm. For comparison, the 1.3 cm radio continuum emission is $0\farcs88$ (CHWC98) with

[3]The 2MASS PSC positions are reconstructed via the Tycho 2 Catalog

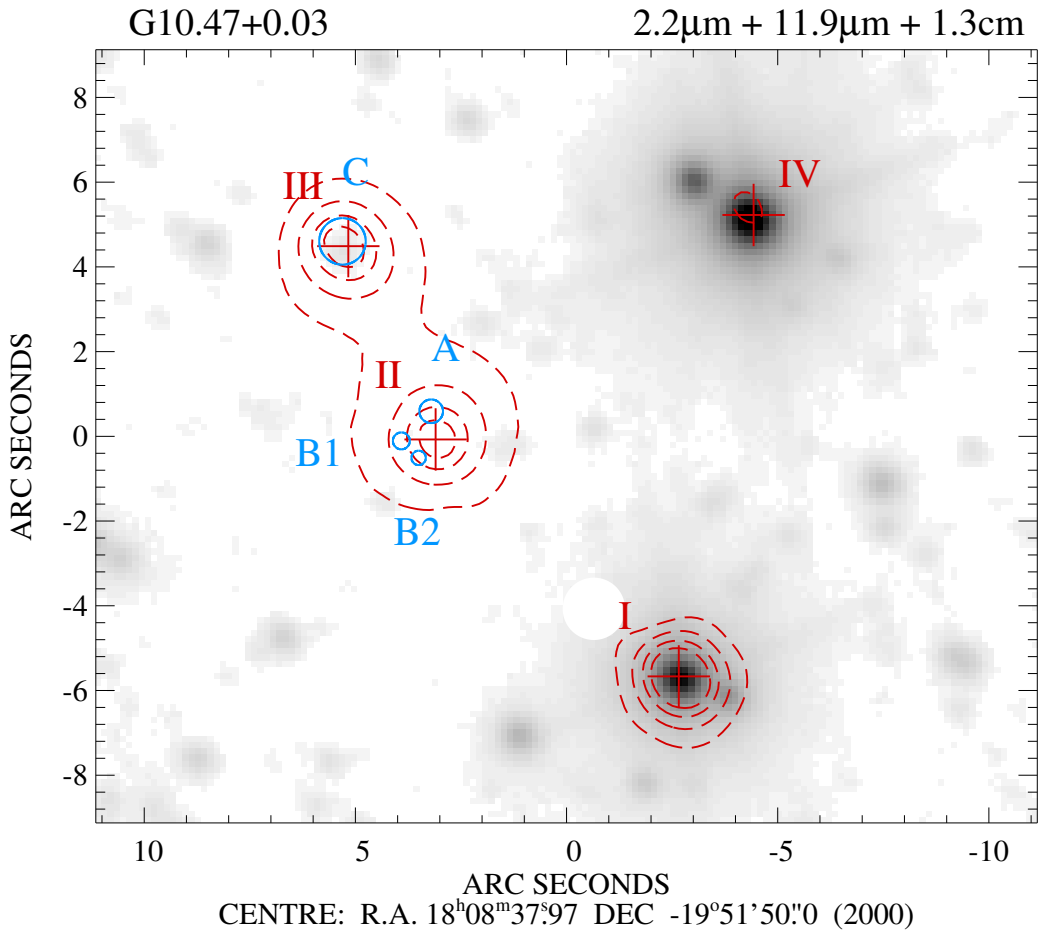

Figure 2.2: TIMMI2 image at 11.9 μm (dashed red contour) superimposed on the ISAAC image (grey scale) at 2.16 μm. Red contour levels go from 6.25 to 25 mJy/$\Box''$ with steps of 6.25 mJy/$\Box''$ (source labeling as in Fig. 2.1). The peak positions of the four MIR sources are marked by red crosses. The blue empty circles correspond to the four UCH II regions, namely A, B1, B2, and C, observed by CHWC98 in the 1.3 cm continuum. The diameter of the circles corresponds to the full width at half power of the radio emission. The millimeter emission from the HMC peaks at the location of the UCH II regions B1 and B2 (Olmi et al. 1996a; Gibb et al. 2002). With a white circular aperture we mask an additional MIR source which appears close to source I when subtracting the chop/nod images. The real location of the source, which we name source VII, is $\sim$27$''$ south-west of source I. Within the uncertainty of our astrometry, source VII coincides with the UCH II region G10.46+0.03A.

an extended spherical halo of 3″ detected in the lower resolution 6 cm radio map by Garay et al. (1993).
We do not detect NIR emission in the direction of the HMC and the three UCH II regions A, B1 and B2. Our near-infrared upper limit of 0.05 mJy/beam (3 σ sensitivity) translates into a Ks limiting magnitude of 17.8 mag. Radio measurements predict at least an O9.5 type star as ionizing source of the UCH II region A and B0 type stars in the case of the UCH II regions B1 and B2. The apparent Ks magnitude for an O9.5/B0 star located at the distance of G10.47+0.03 is 10.3/10.4 mag (intrinsic infrared colours from Tokunaga 2000 and absolute visual magnitude from Vacca et al. 1996). Considering the non-detection at NIR wavelengths and the apparent magnitudes calculated above, we find that the extinction towards the HMC and UCH II regions is at least 7.4 magnitudes at 2 μm.
The measured flux densities and peak positions of the seven MIR sources are provided in Table 2.2. The given total fluxes correspond to the fluxes within a synthetic aperture of 4″. The errors of each flux measurement are estimated to be 15% for the sources from I to IV, and 20% for sources V, VI and VII. We have no detection in the 8.8, 9.8, 17.9 and 20 μm filters. In these cases the upper limits for the flux densities can be deduced from the sensitivities given in Table 2.1.
We note that the IRAS source 18056-1952, which was considered to be the infrared counterpart of the complex massive star-forming region G10.47+0.03 (e.g. WC89, Hatchell et al. 2000), has a 12 μm flux of 7.93 Jy, more than 10 times larger than the total flux we measure from the seven MIR sources. This, together with the fact that none of our MIR sources is located inside the IRAS pointing accuracy ellipse excludes that the IRAS source is related to G10.47+0.03. For completeness, we mention that the Midcourse Space Experiment (MSX) detected a bright unresolved source at 21.3μm whose peak position (α_{2000} = $18^{\rm h}08^{\rm m}38.38^{\rm s}$ and δ_{2000} = -19°51′52.6″ from Egan et al. 1999) is at about 3.″7 south-east from our MIR source II. The MSX position accuracy is about 2″ both in right ascension and declination and the flux measured in the MSX beam amounts to 22±1 Jy. The large 18″ MSX beam includes all our MIR sources but source VII. However, considering the steep rise in the spectral energy distribution (SED) of HMCs (Osorio et al. 1999) we expect that the HMC in G10.47+0.03 contributes most of the flux at 21.3μm.

2.4.2 Mid-infrared spectroscopy

The calibrated N-band spectra of sources II and III are shown in Fig. 2.4. A reliable removal of the atmospheric lines is reached in the wavelength range 8–13 μm. The error plotted on each point represents the flux scatter due to photon noise, additional noise may come from the improper subtraction of telluric lines.
The spectrum of source II is clearly dominated by the silicate absorption feature. The [NeII] emission line at 12.81 μm is detected with a line-to-continuum ratio of about 1.5. In contrast, the spectrum of source III shows strong [NeII] line emission and weak silicate absorption. None of the other MIR fine-structure lines, like [ArIII] at 8.99 μm and [SIV] at 10.51 μm, can be identified in the spectra. Following Okamoto et al. (2001) and Okamoto et al. (2003), we estimate upper limits for the ionizing stars from the flux ratio of the non-detected [ArIII] and [SIV] and the [NeII] emission line. Upper limit fluxes for the [ArIII] and [SIV] lines are obtained by integrating the de-extincted spectra (see discussion for source III in Sect. 2.5.1 for the procedure) in a 0.06 μm interval centered on 8.99 μm and 10.51 μm, respectively. For source II we estimate an O7 type star, while for source III we obtain an O9 type star as

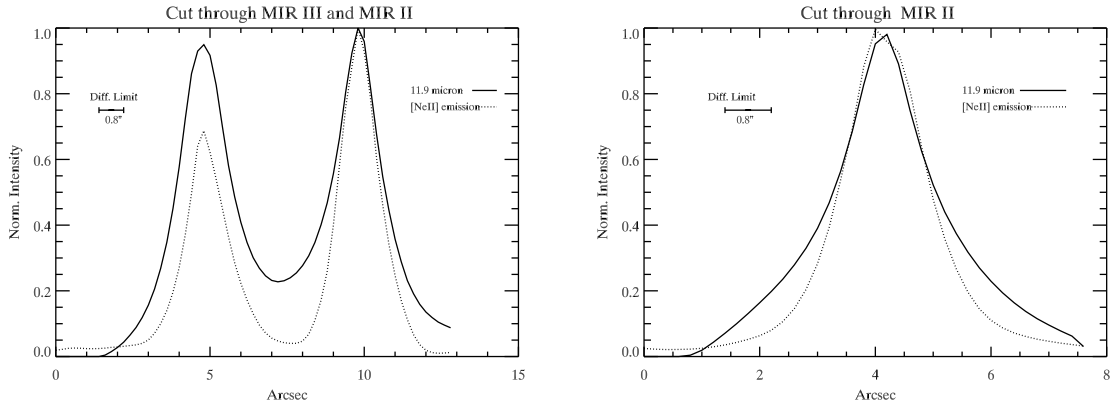

Figure 2.3: Cuts through the MIR sources II and III obtained on the wavelet-filtered images. The width of the cut is 3 pixels. The intensity is normalized to the peak of source II. Left: cut along the line connecting the peaks of the two MIR sources. A faint "bridge" of emission is visible between the peaks at 11.9 μm. Similar faint emission is also present in the non wavelet-filtered images. Right: cut in the perpendicular direction for source II showing different sizes at different wavelengths.

Table 2.2: Measured flux densities and peak positions of the MIR sources. Source labeling is as in Fig. 2.1, source VII belongs to the star-forming region G10.46+0.03 (see Sect. 2.4).

Source	Peak Position		$F_{11.7}$	$F_{11.9}$[a]	$F_{12.9}$[a]	$F_{[NeII]}$
ID	α(2000)	δ(2000)				
	[h m s]	[° ′ ″]	[mJy]	[mJy]	[mJy]	[mJy]
I	18 08 37.78	-19 51 55.7	101	170	154	220
II	18 08 38.19	-19 51 50.0	140	136	457	943
III	18 08 38.34	-19 51 45.6	131	137	236	703
IV	18 08 37.66	-19 51 44.8	23	30	<12	<33
V	18 08 37.59	-19 51 36.6	–	107	<12	<33
VI	18 08 38.61	-19 52 07.3	–	94	201	424
VII	18 08 36.47	-19 52 14.9	–	89	160	309

Note. The estimated flux uncertainty is 15% for sources from I to IV and 20% for sources V, VI and VII

– Sources V, VI and VII are outside the SpectroCam field

[a] Fluxes from the second TIMMI2 run, upper limits represent 3 σ sensitivities

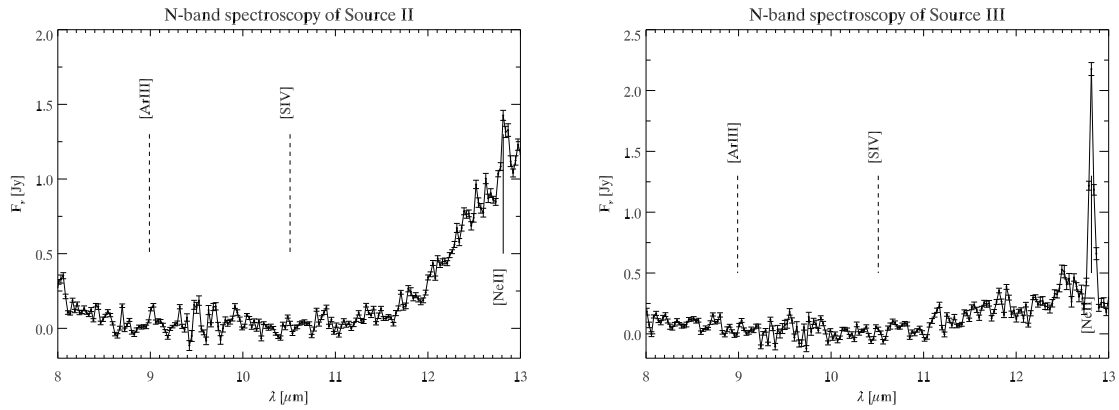

Figure 2.4: N-band spectroscopy of source II and III. The fine-structure emission lines from metal ions are marked with solid lines (detection) and dashed lines (non detection).

upper limits. We note that this method is model-dependent: The observed flux ratios are compared to CoStar calculations by Stasinska and Schaerer (1997). In the next section, we apply a different method which only depends on the observed [NeII] flux to estimate the Lyman continuum flux and thus to determine the spectral types of the ionizing sources.

2.5 Detailed discussion on individual sources

In the following, we discuss the MIR sources with special attention on sources II and III, which are close to the UCH II regions and the HMC in G10.47+0.03.

2.5.1 Source III and the close ultra-compact H II region

Source III is the mid-infrared counterpart of the UCH II region C (WC89). Radio measurements (Garay et al. 1993 and CHWC98) show that at least a B0 type star is responsible for its ionization. We also detect its NIR counterpart in the ISAAC Ks image (see Sect. 2.4). This slightly elongated counterpart has a total flux of 0.22 mJy at 2.16 μm, which corresponds to a Ks magnitude of 16.2. The apparent K magnitude for a B0 star at the distance of G10.47+0.03 is 10.4 mag (intrinsic infrared colours from Tokunaga 2000 and absolute visual magnitude from Vacca et al. 1996). Thus, we calculate an extinction $A_{2.2}$ of 5.8 mag at 2.2 μm. However, this value only represents a lower limit: part of the observed emission at this wavelength may come from scattered light in a non-spherical configuration and from warm dust surrounding the UCH II region. The presence of warm dust around the UCH II region is evident at longer wavelengths where the source appears more extended ($\sim 1\farcs8$ at 11.9 μm after deconvolution with the diffraction-limited beam) and has a flux more than 500 times larger than the extincted black body emission from the star.

To obtain a more accurate value for the extinction and to estimate the spectral type of the ionizing source independently from the radio measurements, we use our MIR spectrum. Assuming a simple model in which the warm dust (emitting in the MIR) is extinguished by a screen of cold dust in the foreground (e.g. Okamoto et al. 2001), the observed flux density

can be expressed as:

$$F_\nu = b\, B_\nu(T_\mathrm{d})\, \epsilon_\nu\, exp(-\tau_\nu) \tag{2.1}$$

with b being a scaling factor, T_d the temperature of the emitting dust, ϵ_ν the dust emissivity and τ_ν the optical depth of the cold dust layer. The optical depth τ_ν is proportional to the dust extinction coefficient and to the line-of-sight column density $N_{(\mathrm{H+H_2})}$. We consider two extreme cases: a) the warm dust is emitting like a blackbody ($\epsilon_\nu = 1$), b) the warm dust emission is optically thin ($\epsilon_\nu \propto \tau_\nu$). As for the dust composition, we use a mixture of carbonaceous and silicate grains (dust opacities from Weingartner and Draine 2001) with two different extinction laws for the local Milky Way ($\mathrm{R_V}$=3.1 and 5.5). The continuum of the observed spectrum (7.9–12.75 μm and 12.9–13.1 μm) is fitted by using the equation 2.1 with b, T_d, and $N_{(\mathrm{H+H_2})}$ as free parameters. The best fit is reached in the case b) and the ISM extinction law ($\mathrm{R_V}$=3.1). Best-fit parameters are provided in Table 2.3. The estimated line-of-sight extinction is 6 magnitude at 9.8 μm. This value translates into $A_{2.2} \sim 9$ magnitude, which is about 3 magnitudes larger than the extinction estimated from the observed Ks magnitude and the expected flux of a B0 star. This also means that only 5% of the measured Ks emission is photospheric flux from the ionizing star, the remaining 95% originates from dust re-emission.

To estimate the spectral type of the ionizing source we will use the de-extincted integrated flux in the [NeII] line ($I^0_{12.8}$) and a formula which links this quantity to the number of ionizing photons per second (Q_0). We determine the spectral type by comparing the calculated Q_0 with values from Table 5 of Vacca et al. (1996). The determination of the de-extincted flux in the [NeII] line is done as follows: First, we subtract the fitted continuum from the spectrum, then we extinct the [NeII] flux density by the measured τ_ν, finally we compute the integral in the [NeII] line between 12.75 and 12.9 μm. With the assumptions of a spherically symmetric, optically thin (see CHWC98), homogeneous and ionization-bounded H II region, we derived in Appendix A the equation that links the Lyman continuum flux to the emission line intensity from any ion. The ratio between the ion density and electron density can be written in our case as $n_\mathrm{ion}/n_\mathrm{e} \sim n(\mathrm{Ne^+})/n(\mathrm{H^+})$. Since we do not see other higher excitation lines as the [ArIII] and [SIV] in our MIR spectra, we can further assume $n(\mathrm{Ne^+})/n(\mathrm{H^+}) \sim n(\mathrm{Ne})/n(\mathrm{H})$ that is the neon over hydrogen abundance. Thus, equation A.8 can be re-written as:

$$Q_0 = 2.566 \times 10^{34}\, T_\mathrm{e}^{-0.8}\, D^2\, \frac{n(\mathrm{H})}{n(\mathrm{Ne})}\, \frac{I^0_{12.8}}{\epsilon_{12.8}} \tag{2.2}$$

where T_e is the electron temperature in K, D the source distance in kpc, $I^0_{12.8}$ the de-extincted intensity of the [NeII] line in $\mathrm{erg\,s^{-1}\,cm^{-2}}$ and $\epsilon_{12.8}$ the line emissivity in $\mathrm{erg\,cm^3\,s^{-1}}$. We assume T_e equal to 10000 K (CHWC98) and $n(\mathrm{Ne})/n(\mathrm{H})$ equal to 1.2×10^{-4}, which is the solar abundance as given by Grevesse and Sauval (1998). The calculation of the line emissivity $\epsilon_{12.8}$ is done following the formulae 3.25, 4.12 and 5.29 in Osterbrock (1974) and assuming atomic data from Saraph and Tully (1994): For the specific T_e and the electron density given by CHWC98, we obtain a value of $4.6\times10^{-23}\,\mathrm{erg\,cm^3\,s^{-1}}$. The derived spectral type (see Table 2.3) is in a good agreement with that estimated from radio measurements.

Our infrared images and spectrum show that the *B0 star ionizing the UCH II region C* is surrounded by dust which is optically thick at these wavelengths. This means that we cannot use the infrared fluxes to estimate the amount of dust surrounding the UCH II region. However, we can derive upper limits for the dust mass from the BIMA non-detection at 1.4 mm (Gibb et al. 2002). In the natural weighted BIMA map the 1 σ detection limit is 20mJy/beam

Table 2.3: Best fit parameters to the N-band spectra and estimated spectral types for the ionizing sources

Parameter	Unit	Factor	Source II	Source III
$T_{\rm d}$	[K]		275±20	319±46
$N_{(\rm H+H_2)}$	[$\rm cm^{-2}$]	($\times 10^{23}$)	2.7±0.1	1.4±0.2
$\tau_{9.8}$			12	6
$I_{12.8}$	[$\rm W/m^2$]	($\times 10^{-16}$)	5.0	18.9
$I^0_{12.8}$	[$\rm W/m^2$]	($\times 10^{-14}$)	2.3	1.3
$\log(\rm Q_0)$			48.35	47.99
SpTy			B0–O9.5	B0.5–B0

for a beam of $1.98'' \times 1.27''$ (Wyrowski private communication). We assume optically thin emission at 1.4 mm, two values for the dust temperature (30 and 50 K) and mass absorption coefficient from Ossenkopf and Henning (1994) for a gas density of $10^5\,\rm cm^{-3}$. A dust mass between 0.2–0.4 $\rm M_\odot$ is derived. This value translates into 20–40 $\rm M_\odot$ for a gas/dust ratio of 100 and into upper limit column densities of $1.9\text{–}3.5 \times 10^{23}$ $\rm cm^{-2}$ for the molecular hydrogen (see equations 2 and 3 in Henning et al. 2000). This column density is in good agreement with the value we estimate by fitting the MIR continuum of our N-band spectrum (Table 2.3).

2.5.2 Source II and its relation with the hot core

Object II is the most exciting among our MIR sources. Three UCH II regions and a HMC have been identified by CHWC98 in this region. CHWC98 suggest a picture in which the three massive stars, at the stage of UCH II regions, are embedded in the dense molecular core traced by ammonia emission. Since the UCH II regions B1 and B2 are more compact than A and show more absorption in NH_3, CHWC98 propose that A is lying closer to the surface of the HC, i.e in a less dense region. The fact that the three UCH II regions are tracing embedded stars is supported by the compactness of their radio emission: The two VLA 6 cm maps from WC89 and Garay et al. (1993) at different resolution provide the same total flux for the three UCH II regions. To show the complexity of this region we superimpose the radio, ammonia and MIR emission in Fig. 2.5.

Up to now, only few cases are known in which MIR emission is detected from the close vicinity of HMCs (De Buizer et al. 2003). Proving that the MIR arises from the HMC itself would support the idea of internally heated cores. However, the exact location of the MIR emission is difficult to determine independently from the radio sources and/or maser sites, whose relation to the MIR emission is yet not clear. In Sect. 2.3 we demonstrated that our MIR astrometry is accurate to $0\farcs3$ based on stars with counterparts at different wavelengths. This high accuracy allows to explore the relation between the UCH II phenomena, the HMC and the MIR emission. Here, the main question is whether the MIR emission is coming from dust surrounding one of the three UCH II regions or it is indicating the presence of a young massive star (before the UCH II phase) deeply embedded in the HMC. To answer this question we use both MIR images and spectroscopic data.

Before investigating the two scenarios, we briefly summarize the main observational results:

I) Based on our astrometry, *none of the UCH II regions coincides with the peak of the MIR*

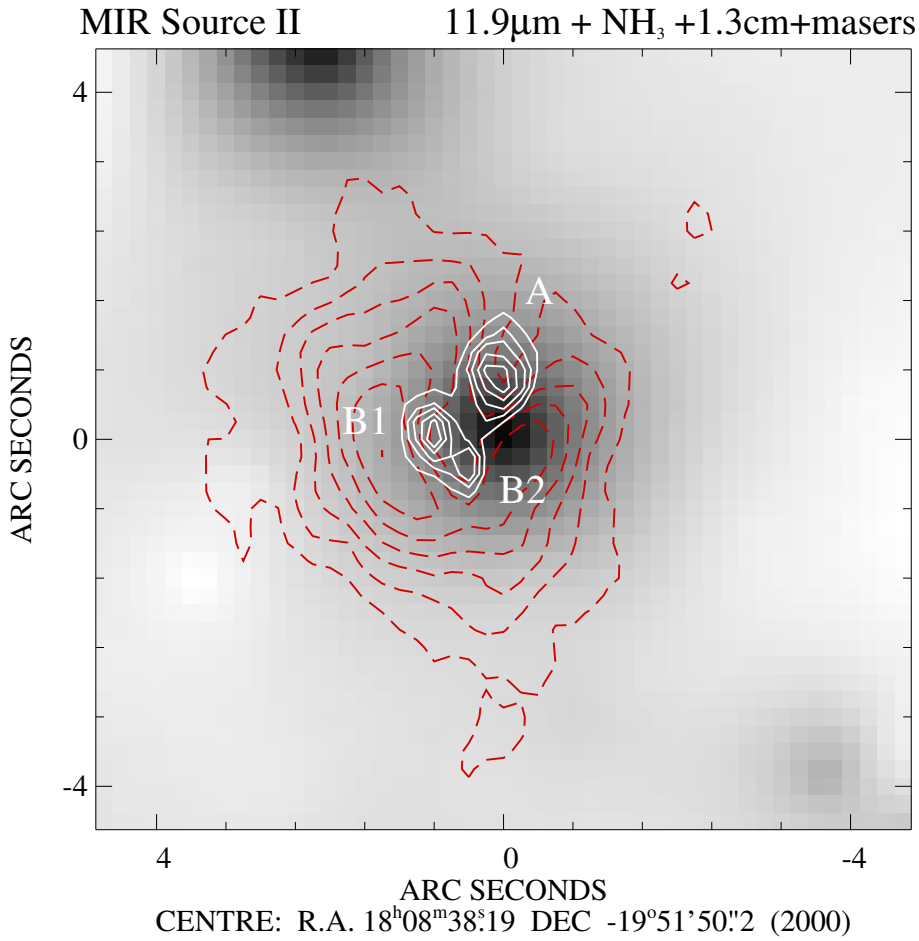

Figure 2.5: Image of the MIR source II at 11.9 μm with contours of the 1.3 cm radio continuum (solid white lines) and of $NH_3(4,4)$ line emission (red dashed lines) from CHWC98. White contour levels are spaced by 7 mJy/beam starting from 5 to 33 mJy/beam, red-dashed contours are spaced by 4 mJy/beam from 3 to 27 mJy/beam.

source II: this peak is located south of the UCH II region A, at about the same distance ($\sim$0.″6=3480 AU) from A and B2. The UCH II region B1 is further away from source II at about 0.″8. The MIR emission does not coincide with the center of the HMC, which is believed to be close to the most embedded UCH II regions B1 and B2.
II) The MIR emission is extended in NW-SE direction even in the [NeII] filter (deconvolved FWHM of 0.″9 after the continuum subtraction). The MIR extension is even larger at 11.9μm, about 1.″7 (see Fig. 2.3).
III) The MIR spectrum does not show the forbidden lines of [ArIII] and [SIV] thus implying an O7 upper limit for the spectral type of the ionizing source (see Sect. 2.4.2).
IV) CHWC98 report a lower limit for the H_2 column density of 2×10^{23} cm^{-2} towards the HMC which is comparable with the values we find from fitting the continuum of the MIR spectrum. Thus, object II is at a distance similar to the three UCH II regions and the HMC. Other estimates of the molecular hydrogen column density towards the HMC range between 3×10^{23} cm^{-2} (Hofner et al. 2000) and 6×10^{24} cm^{-2} (Olmi et al. 1996a). The exact location of source II in the HMC cannot be determined from these data.
V) The slope of the radio emission as given from the measurements at 6 cm (WC89) and 1.3 cm (CHWC98) is $S_\nu \propto \nu^{0.9}$ for the UCH II region A and $S_\nu \propto \nu^{1.4}$ for B. Both slopes are different from that expected in the case of ionization due to a stellar wind ($S_\nu \propto \nu^{0.6}$, Simon et al. 1983). Also the size of the UCH II region A increases towards shorter wavelengths, contradicting the wind hypothesis ($R_\nu \propto \nu^{-0.6}$, Hoare and Garrington 1995).
We now consider the first scenario, namely a massive star embedded in the HMC at a stage prior to the UCH II phase. In the early phases of massive star formation strong accretion could quench the radio free-free emission (Yorke 1986) and constrain the ionized hydrogen into a small dust-evacuated cavity of radius $R_c \sim (L_*/4\pi\sigma T_{\rm d}^4)^{1/2}$ (see e.g. Churchwell 2002). Using the same approach as for source III, we determine a lower limit spectral type of B0–O9.5. For these spectral types, the ionized region is well traced by [NeII] line emission. For a luminosity of 10^5 L$_\odot$ (Vacca et al. 1996) and dust sublimation temperature $T_{\rm d} \sim 1000$ K, we estimate an R_c of about 50 AU, which is 0.″008 at 5.8 kpc distance. Since we detect extended emission in the [NeII] line, we conclude that no massive star prior to the UCH II phase can be responsible for the observed [NeII] emission.
In the second scenario, we assume that *the warm dust around one of the UCH* II *regions is the source of the MIR flux detected as object II.* To explain why the peak of the MIR source II is shifted from the three UCH II regions, we consider the following situation: The embedded UCH II regions lie where the line-of-sight extinction is high, and are surrounded by warm dust emitting at MIR wavelengths. The peak of the MIR emission would coincide with the UCH II regions, but due to the extinction gradient the peak is apparently shifted towards the direction of lower extinction. Thus, the MIR-radio continuum offset is the result of extinction and geometry of the sources. We point out that estimating the spectral type of the ionizing star following the method described in the case of source III would be incorrect. Since we only see part of the MIR emission, the spatial ionization structure of the UCH II region has to be considered. An upper limit for the spectral type of O7 can be obtained from the ratio of the non-detected and detected forbidden emission lines (see Sect. 2.4.2). We now consider if such a star could maintain an ionized halo detectable in the MIR and showing [NeII] emission even at the distance of 0.″6 $\sim$ 0.02 pc. The CoStar models from Stasinska and Schaerer (1997) predict that the [NeII] emission can extend up to 0.055 pc for B0–O9 stars and up to 0.083 pc for O9–O8 stars embedded in spherically symmetric ionized regions with uniform electron density (see Fig. 13 of Okamoto et al. 2003, and text therein). These values do not exclude

the possibility that the [NeII] emission is due to the ionization from one of the embedded UCH II regions. We also mention that we find a marginal shift in the peak location of source II between the broad-band 11.9μm filter and the [NeII] narrow-band filter. The [NeII] peak of source II is 0.″1 north-east of the 11.9μm peak emission, i.e. closer to the UCH II region A. This shift, at the limit of our accuracy, supports our second scenario.

2.5.3 The other mid-infrared sources in the field

In the large field of view of the images from the second TIMMI2 run we detected seven MIR objects. The sources II and III belong to the massive star forming region G10.47+0.03 and have been described in the previous two Sections. Object VII is the MIR source located at the largest distance from the HMC in G10.47+0.03 and is found to coincide with the UCH II region G10.46+0.03A within our astrometric accuracy. To investigate the nature of the other four MIR sources, we retrieve their near-infrared magnitudes from the 2MASS PSC and we plot their colours in a NIR colour-colour diagram (for the use of the colour-colour diagram we refer to Lada and Adams 1992). The colours of main sequence, giant and supergiant stars are taken from Tokunaga (2000).
Source I lies on the right side of the main-sequence stripe, thus indicating NIR excess. This excess is thought to originate from hot circumstellar dust. The presence of dust around source I is confirmed by our MIR images: Source I appears slightly extended in the broad band filters (deconvolved FWHMs of $\sim 1''$ at 11.7 and 11.9 μm and 0.″5 at 12.9 μm) and has an SED slowly increasing towards longer wavelengths (see Table 2.2). The continuum-subtracted [NeII] images show no emission. Although the further discussion of this object is out of scope of the current paper, we note that the lack of the [NeII] and free-free radio emission proves that this star is not a massive (earlier than B0 spectral type) young stellar object.
Sources IV and V lie within the region of reddened main-sequence stars. To determine their spectral types and luminosity classes we adopt the following method: I) By shifting these sources back on the colour-colour diagram – along the reddening vector – we find the possible spectral type/luminosity class combinations. II) From the difference between the old and new location in the colour-colour diagram we estimate the extinction. The distance is given by the comparison of the apparent and the absolute magnitudes taking the derived extinction into account. III) As the last test, we compare the 11.9 μm flux of this hypothetical star (at the given distance and extinction) to our measured MIR flux. With this approach we find that sources IV and V are strongly reddened ($A_V > 20$ mag). Should they be dwarf stars, they would necessarily lie within a distance of 80 pc to fit the apparent brightness we observed. However, comparing the $A_V > 20$ mag to the mean extinction value of 1.9 V-mag/kpc of the Milky Way disk (Allen 1973), we can exclude that these sources are reddened main sequence stars. For source IV the most probable nature is that of a G0-G3 supergiant at a distance of about 5 kpc, although the measured MIR flux at 11.9 μm is slightly lower than that estimated from a black body approximation ($\sim$44 mJy) of the photosphere. Similarly, source V is consistent with a supergiant of spectral type B6 at a distance of 2.5 kpc and an extinction of 30 mag in V.

2.6 Summary of the main results on G10.47+0.03

We observed the massive star-forming region G10.47+0.03 at infrared wavelengths in order to study in detail the relationship between the HMC and the UCH II regions. An astrometric

accuracy at the subarcsecond level and additional spectroscopy of the two most interesting MIR sources allow us to draw the following main conclusions:

1. We detect extended mid-infrared emission (source II) towards the HMC and the three UCH II regions. However, the mid-infrared emission does not coincide with the HMC position nor with the position of any of the UCH II regions. The most plausible scenario is the one in which *the MIR emission of source II originates from dust heated by one of the UCH II regions embedded in the HMC*. The shift in the peak emission between the ionizing star and the MIR emission is interpreted as due to geometrical effect and changes in the extinction. This scenario is supported by the marginal shift of the peak positions found at 11.9 μm and in the [NeII] filter.

2. The UCH II region C, which is located outside the HMC, is found to have a mid-infrared and a near-infrared counterpart. From our MIR spectroscopy *we derive a B0 spectral type for the star ionizing the UCH II region C*. This spectral type agrees well with that found from radio free-free emission (CHWC98). The size of the radio free-free emission together with the relatively low column density towards the source suggest that the UCH II region C could have evolved rapidly because of a relatively low density environment.

3. The mid-infrared source VII is coincident with a UCH II region in the star forming region G10.46+0.03.

4. The mid-infrared source I shows infrared excess thus indicating the presence of surrounding warm dust. The absence of [NeII] and free-free radio emission proves that the star has a spectral type not earlier than B0.

5. Combining the 2MASS fluxes with our MIR observations we find that the mid-infrared sources IV and V are possibly supergiant stars in the foreground of the massive star-forming region G10.47+0.03.

2.7 Ultra-compact H II regions separated from hot cores

In the frame of our mid-infrared campaign to detect the early phases of massive star formation, we also targeted the hot molecular core W3(H_2O) and the neighboring UCH II region W3(OH). W3(OH) is located at a distance of 2.2 kpc (Humphreys 1978) and is very well-studied in the radio domain by continuum and molecular line investigations. The HMC W3(H_2O), also known as Turner-Welch object (TW, Turner and Welch 1984), lies $\sim 6''$ east of W3(OH). This enigmatic source shows an outflow traced by the proper motion of water masers (Alcolea et al. 1993) and is associated with radio continuum jets, presumably of synchrotron nature (Reid et al. 1995). Wyrowski et al. (1999b) detected another source in their interferometric images at 220 GHz, thus suggesting that the region harbours a cluster of protostars. The thermal infrared emission from W3(OH) has been already studied by Keto et al. (1992) using one of the first MIR array cameras (Arens et al. 1986). The same observations led Keto et al. to claim the detection of W3(H_2O) at 12.2 μm with a flux density of 45 ± 10 mJy.
In the following, we will present our MIR observations (Sect. 2.8), the immediate results (Sect. 2.9) and a detailed modeling of the dust surrounding the UCH II region and HMC (Sect. 2.10.3) in order to derive their individual luminosities.

2.8 Observations of the W3(OH) region

The observations were performed on 27 December 1998 using SpectroCam–10[4] (see Sect. 2.2 for more details on the camera). We applied the common chopping/nodding technique with a chopper throw of 20″ in north-south direction and filters with 8.8, 11.7 and 17.9 μm as central wavelenghts. The data reduction follows the same steps described in Sect. 2.2. To recover faint extended emission otherwise hidden in the noise, the images have been wavelet filtered with the algorithm of Pantin and Starck (1996). The high dynamic range of the individual frames allowed the application of a shift-and-add procedure which includes resampling, yielding a final pixel scale of 0.″125. To enlarge our field of view, we observed two positions at 11.7 μm, the first centered on W3(OH) and the second offset the by 10″ east. Lastly, frames were mosaicked.

The star α Tau was measured at about the same airmass (1.2) as the target and was used for the flux calibration. Its photometric zero points and photometry are from Cohen et al. (1992) and Cohen et al. (1995). The observations were performed during photometric conditions, with an internal photometric error of less than 2% as estimated from the flux variation of the standard star. The 3σ sensitivities (mJy/□″) for the detection of point sources in the final images are 4 at 8.8 μm, 6 at 11.7 μm, and 93 at 17.9 μm.

We detect two mid-infrared sources in our final images. Their morphology allows to identify them with the ultra-compact H II region W3(OH) and the cometary UCH II region north-east of it. Our astrometry is based on the radio position of the UCH II region W3(OH) which is assumed to coincide with the peak of the thermal infrared emission. Because the HMC and the UCH II region are spatially separated by about 6″, the accuracy of such astrometric reference frame is sufficient to unambiguously interpret our data.

2.9 Immediate results

The prime results of our observations are contained in Fig.2.6 which shows the 11.7 μm continuum image together with the 8.4 GHz contours from Wilner et al. (1999). The two infrared sources in Fig.2.6 correspond to W3(OH) and the cometary UCH II region located north-east of it. A comparison with α Tau (Fig. 2.6 insert) shows that W3(OH) is spatially well resolved in our diffraction-limited 11.7 μm image (beam size 0.″6). The lowest contour line of the infrared emission represents the 3 σ detection limit. *The flux density from W3(H_2O) is below our sensitivity limit.* This result is clearly in contradiction with the finding of Keto et al. (1992) who claimed the infrared detection of W3(H_2O). We briefly mention that their interpretation requires caution since the emission they presume to originate from W3(H_2O) peaks only 4″ instead of 6″ east of W3(OH) (see their Fig.1). Furthermore, their total flux of 45±10 mJy contradicts with the fact that this emission well exceeds their lowest contour level of 100 mJy/□″. Thus, we conclude that they did not see W3(H_2O) as well, and were confused by the north-eastern UCH II region.

There is a good overall correspondence between the thermal infrared and the 8.4 GHz radio continuum emission. However, there are certain features which are different in both maps. The north-eastern trail from W3(OH) is more confined in the radio continuum and only marginally indicated by the infrared contours. The peak of the radio emission from the

[4]Observations at the Palomar Observatory were made as part of a continuing collaborative agreement between the California Institute of Technology and Cornell University.

north-eastern UCH II region is closer towards W3(OH) than its infrared maximum. This is presumably caused by the extinction of a dust lane stretching from W3(H_2O) to the north-west. Indeed, the $C^{17}O$(1-0) map of Wyrowski et al. (1997) shows such a feature.
A more detailed discussion of the HMC and UCH II region W3(OH) is presented in the next sections. For completeness, we report the following flux densities of 0.3, 0.6 and 6.1 Jy at 8.8, 11.7 and 17.9 μm respectively for the northeastern UCH II component (within a 3 $''$ aperture).

2.10 Detailed discussion

In the following we will discuss more in detail the results and implications of our observations on the UCH II region W3(OH) and the HMC W3(H_2O).

2.10.1 The ultra-compact H II region W3(OH)

We derived the FWHM of the MIR emission from Gaussian fits, taking the size of the diffraction-limited beam into account. The sizes and flux densities of W3(OH) are listed in Table 2.4. The fluxes were obtained using a synthetic aperture of $4''$ diameter. The extent of the thermal emission is larger than that of the 8.4 GHz radio continuum which has a FWHM of $1\farcs52$, clearly indicating that the warm dust is more extended than the ionized gas. The angular size of the MIR emission depends on the wavelenght approximately as $\mathrm{FWHM}(\lambda) \sim \lambda^{0.6\pm0.2}$. This can be explained if the temperature declines with increasing distance from the heating star(s). The comparison of our flux densities of W3(OH) with other estimates allows conclusions on the influence of different beam sizes. For this purpose, we retrieved the IRAS-LRS and the ISO-LWS spectra from the data archives. In addition, we identified W3(OH) in the MSX point source catalog (Egan et al. 1999) and we provide the fluxes in Table 2.4. The LRS spectrum was integrated according to the applied passbands. It is obvious that the 8.8 μm fluxes given in Table 2.4 considerably exceed our value. This can be explained by ubiquitous emission attributed to Polycyclic Aromatic Hydrocarbons (PAHs) surrounding the UCH II region which strongly contributes to the flux in the large apertures of IRAS and MSX. Pronounced 7.7 and 8.6 μm PAH bands can be misleading in ground-based derivations of the optical depth of the 9.7 μm silicate feature (e.g., Roelfsema et al. 1996).

2.10.2 The hot molecular core W3(H_2O)

Our attempt to detect W3(H_2O) in the infrared regime was stimulated by the presence of the highly collimated outflow from the TW object. Generally, outflow lobes allow the leakage of infrared emission with scattering being the dominant mechanism (e.g., Fischer et al. 1996). An example is the high-mass Class 0 object NGC6334 I(N) for which Sandell (2000) rendered the detection of infrared emission impossible because of the extremely high extinction derived from mm/submm continuum maps. However, this source is associated with NIR emission (Tapia et al. 1996; Megeath and Tieftrunk 1999) obviously originating from the blue-shifted lobe of its outflow. The flux densities from W3(H_2O) in the absence of any absorbing matter can be estimated from the temperature map given by Wyrowski et al. (1997). The expected peak surface brightness amounts to 2170 Jy/$\square''$ at 11.7 μm. Together with our 3σ sensitivity, this yields a lower limit to the extinction at this wavelength of 12 mag. Our failure to detect this source is consistent with the high molecular hydrogen column densities of $1 \ldots 3.5 \times 10^{24}$ cm^{-2}

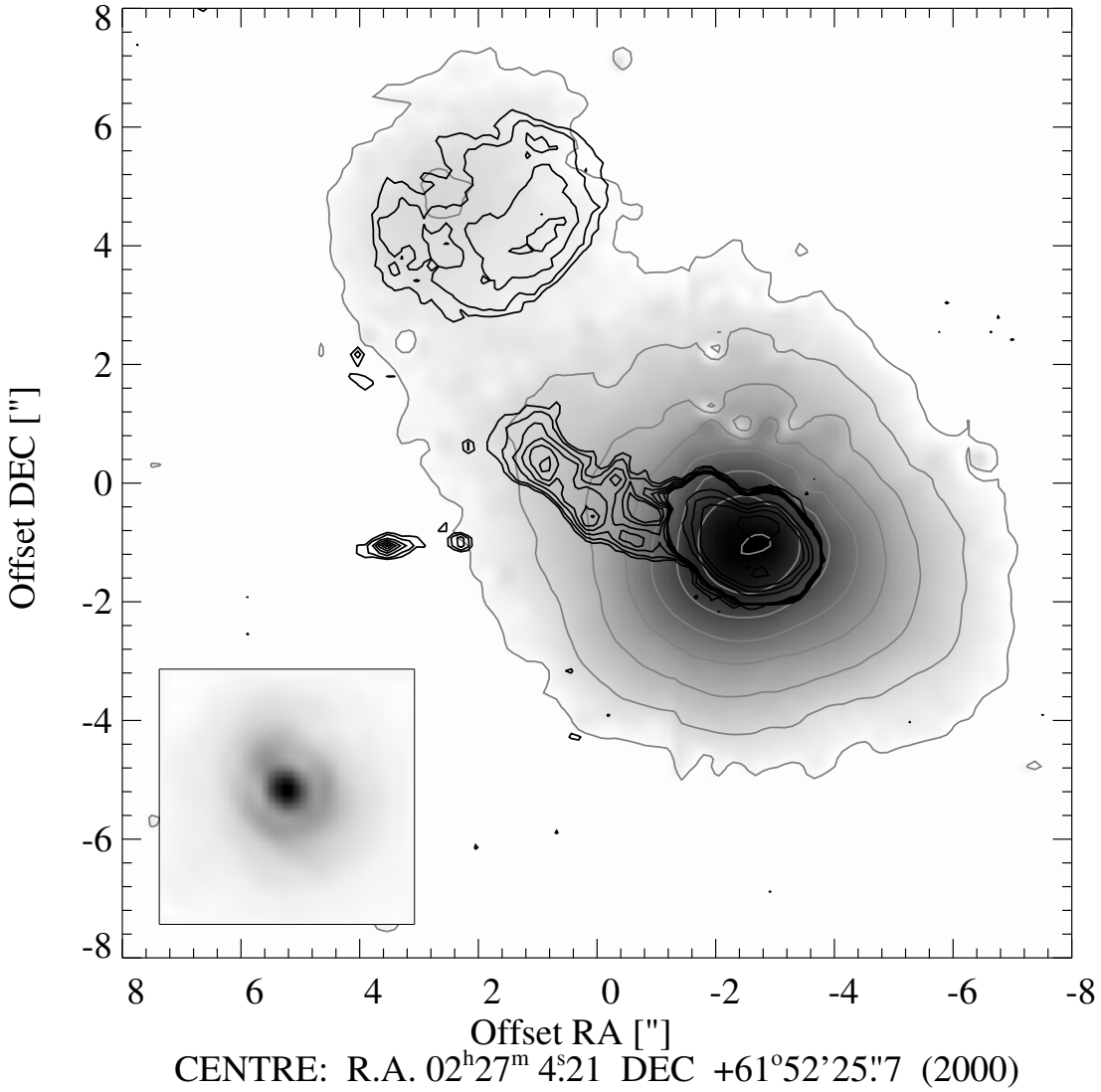

Figure 2.6: 11.7 μm image of W3(OH) with contours of the 8.4 GHz radio continuum emission (black lines) from Wilner et al. (1999). The grey contours delineate the 11.7 μm emission and are spaced by a factor of 2.5 starting at 3 σ (10 mJy/$\square''$). W3(H_2O) is the elongated radio source at ($+3''.9, -0''.6$). The lower-left insert shows the 11.7 μm image of the reference star α Tau using a logarithmic brightness scale.

Table 2.4: SpectroCam–10, IRAS-LRS, and MSX-SPIRIT III flux densities of W3(OH)

Wavelength [μm]	Peak flux [Jy]/$\Box''$	Total flux [Jy]	FWHM [$''$]
8.8	2.6	6.5	1.96
11.7	7.7	22.4	2.08
17.9	19.5	93.0	2.88
IRAS-LRS [μm]	Total flux [Jy]	MSX [μm]	Total flux [Jy]
8.8	24.9	8.28	11.1
11.7	24.1	12.13	36.7
17.9	89.1	14.65	77.1
		21.41	332.6

inferred from molecular line and continuum investigations (Turner and Welch 1984; Wyrowski et al. 1997). This suggests that the molecular outflow of W3(H_2O) is very young, i.e. has not fully penetrate the HMC yet, and, in addition, might be in the plane of the sky. In fact, Fig. 1 from Wyrowski et al. (1999b) shows that the jet is confined to the region of the HMC. The moderate expansion velocity of the H_2O masers of $20\,\mathrm{km\,s^{-1}}$ (Alcolea et al. 1993) suggests a dynamical timescale of only 500 yr which is consistent with the recent upper limit on proper motions of the radio jet of $150\,\mathrm{km\,s^{-1}}$ (Wilner et al. 1999). These velocities are low compared to those of thermal radio jets (Anglada 1996) and indicate that the outflow is presumably slowed-down by the high-density environment.

2.10.3 Modeling the dust emission

One of the questions concerning W3(OH) and W3(H_2O) is related to their individual luminosities which directly translates to the nature of the internal heating sources. Although it is reasonable to assume that the internal heating is due to stars of intermediate or high mass, no direct confirmation of their presence exists. The luminosity might also, at least partly, result from accretion. The high column densities towards W3(H_2O) make it difficult to figure out whether this accretion is due to infall from a circumstellar disk or stellar mergers like in the scenario proposed by Bonnell et al. (1998).
The derivation of the individual luminosities has to be based on the decomposition of the spectral energy distribution. While our measurements provide constraints for the ground-based thermal infrared windows, the lack of spatial resolution in the far-infrared (FIR) did not permit us to separate both components. An upper limit of $\sim$1800 Jy on the 50 μm flux of W3(H_2O) has been established by Campbell et al. (1989) from KAO scans. In the mm/submm range, aperture synthesis measurements show that the 1.3 mm emission from W3(H_2O) is due to dust radiation while free-free emission dominates the flux of W3(OH) at this wavelength (Wyrowski et al. 1999b). The ISO-LWS spectrum shows that the SED between 42 and 140 μm can well be fitted by a modified black-body (35 K and $\kappa(\nu) \sim \nu^2$). The association of W3(H_2O) with cold dust suggests that the FIR excess for $\lambda > 140\,\mu$m is presumably due to the HMC.

Table 2.5: Model parameters

Source	L_* ($10^4 L_\odot$)	R_{in} (AU)	R_{out} (AU)	M_d ($M_\odot$)
W3(OH)	8[1]	2270[2,3]	57000[4]	5.0
W3(H_2O)	2.4[5,6]	190	24000[5]	3.0[7]

References: [1] Wink et al. (1994), [2] Chini et al. (1986), [3] Campbell et al. (1989), [4] Zeng et al. (1984), [5] Osorio et al. (1999), [6] Thompson (1984), [7] Wyrowski et al. (1997).

We model the W3(OH) and W3(H_2O) sources to determine how much the HMC contributes to the FIR excess seen in the ISO-LWS spectrum. In addition we intend to calculate which sensitivities are required to detect the HMC in the MIR regime. The input SED is based on fluxes coming from this work, from the MSX point source catalogue at 21.41 μm (see Table 2.4), from the IRAS-LSR and ISO-LWS spectra and from Wyrowski et al. (1997) as well as Wilner et al. (1995) for the mm wavelenghts. To solve the radiative transfer problem we used the 1D-code of Manske and Henning (1998) and assumed spherically symmetric shells for W3(OH) and W3(H_2O) like in previous works. The dust composition includes graphite, silicate and iron (optical constants from Dorschner et al. 1995 and Draine and Lee 1984) and a Mathis, Rumpl & Nordsieck-type size distribution (Mathis et al. 1977) is assumed. The model parameters and related references are given in Table 2.5: here L_* is the luminosity of the embedded star, R_{in} and R_{out} the inner and the outer radius of the shell, M_d the dust mass. We note that the inner radius of the dust shell of W3(OH) coincides with the outer radius of the UCH II region. For the HMC the inner radius is set by the dust sublimation temperature ($\sim$ 1000 K). To model the spectral energy distribution of W3(H_2O) we follow Osorio et al. (1999) in adding an accretion luminosity of 4.2×10^4 $L_\odot$ to the stellar luminosity and a free-fall density shell. For W3(OH) the density profile that better fits our observations is Gaussian and yields an almost constant density distribution up to $\sim$ 20000 AU. The resulting opacities at the mm wavelenghts varies as $\nu^{1.3}$.
Figure 2.7 shows the individual SEDs as well as their superimposition. Our model produces the following FWHMs at the observed wavelenghts: 1.″6 at 8.8μm, 2.″0 at 11.7μm and 3.″1 at 17.9μm. These values are quite in agreement with those given in Table 2.4 which supports the view that the parameters of the radiative transfer model are representative for the actual conditions. From the spectral energy distribution of W3(H_2O) we conclude that deep observations in the Q band might be able to detect the MIR emission from the HMC.

2.11 Summary of the main results on W3(OH) and W3(H_2O)

We targeted the UCH II region W3(OH) and its hot core W3(H_2O) aiming to detect and characterize these early phases of massive star formation in the MIR regime. The 6″ separation between the two targets offers the possibility to clearly separate the UCH II and HMC emission already with 5-m class ground-based telescopes. The main conclusions of this work are as follows:

1. Our diffraction-limited imaging resolve the thermal emission from W3(OH) and clearly

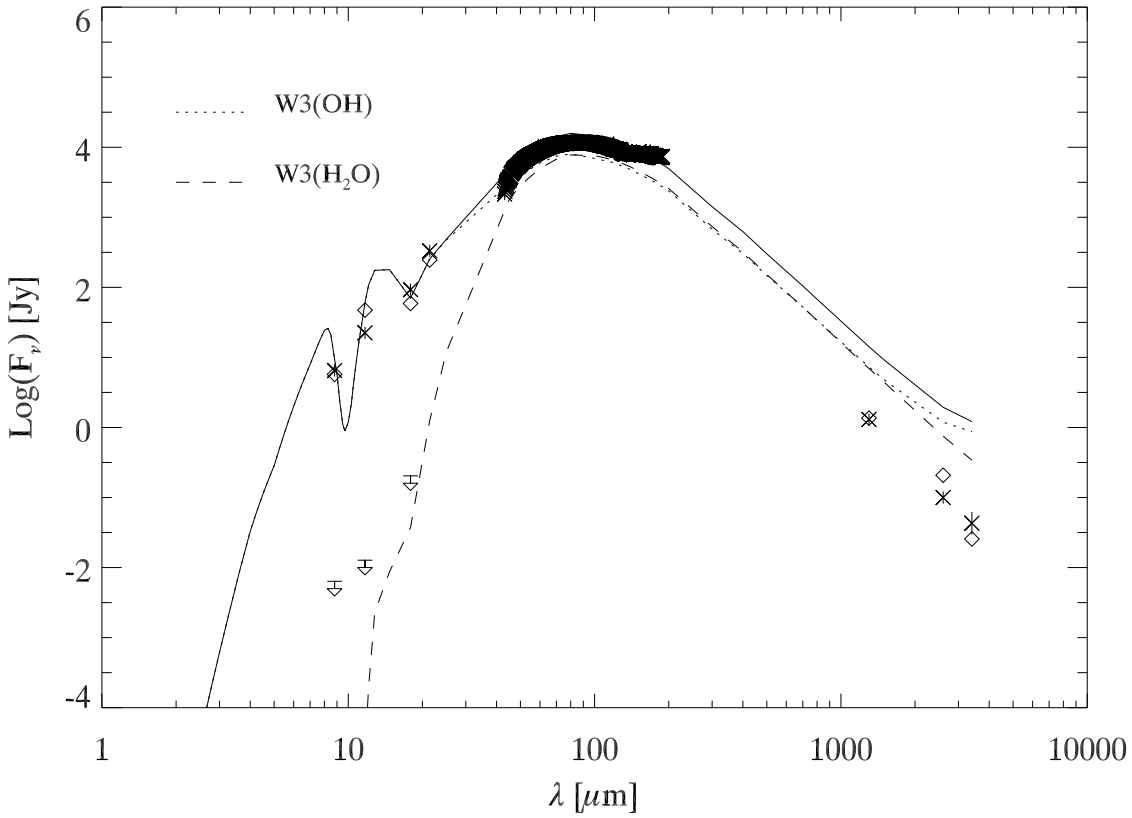

Figure 2.7: SED of the individual sources (W3(OH) – dotted line, W3(H_2O) – dashed line) and of their sum (solid line). Asterisks with errorbars indicate the measured flux densities. Diamonds represent the model fluxes for the observational beam sizes. Arrows mark the detection limits for W3(H_2O).

indicates a wavelength dependence of its apparent size.

2. The comparison of our 8.8 μm flux to those measured with IRAS and MSX leads to the conclusions that PAHs surround W3(OH).

3. *The thermal infrared counterpart to the hot core W3(H_2O) is not detected at any wavelength of our observations.* This revises the finding of Keto et al. (1992) which most probably resulted from confusing W3(H_2O) with the UCH II region northeast of W3(OH). We derive a lower limit for the extinction at 11.7 μm towards W3(H_2O) of 12 mag.

4. In accordance with our thermal infrared imaging and (sub)mm studies, the ISO-LWS spectrum of W3(OH) can be decomposed in two components with W3(OH) being the hotter, more evolved, object while W3(H_2O) dominating at far-infrared wavelengths.

The observations and main results on the massive star-forming region G10.47+0.03 are summarized in a paper submitted to the Astronomy & Astrophysics Journal. Results on the mid-infrared campaign towards the W3(OH) region appeared in Stecklum et al. (2002).

Chapter 3

Massive Stars and the Potential of Interferometry

The question whether massive stars form as essentially a scaled-up version of low-mass stars via disk accretion (McKee and Tan 2002; Yorke and Sonnhalter 2002) or from merging of intermediate-mass stars (Bonnell et al. 1998) is still strongly disputed. Observationally prove one of the two scenarios requires good sensitivity and above all high angular resolution. Because mid-infrared (MIR) wavelengths are about a hundred times less affected by extinction than optical wavelengths, the MIR regime gives the possibility to penetrate the thick dusty cocoons where massive stars are born. However, conventional MIR imaging rarely reaches the sub-arcsecond resolution and is unable to resolve the immediate environment of many massive young stellar objects.
The new mid-infrared interferometer MIDI achieves unprecedented spatial resolutions of 10 milliarcsecond (mas) at 10 μm in combination with resolving power ($\lambda/\Delta\lambda$) up to 270 and fairly good sensitivity of tens of Jy. As part of the MIDI Guaranteed Time programme "The Formation of High-Mass Stars", we selected 35 massive young stellar objects aiming to investigate their multiplicity and the distribution of the surrounding dust.
In this Chapter, we present the first MIDI results on the young massive star M8E IR. The basics of interferometry and the main characteristics of the MIDI instrument are introduced in the first two sections (Sects. 3.1 and 3.2). We present our target and the motivation to observe at such high angular resolution in Sect. 3.3. The observations and the data reduction are described in Sect. 3.4. Finally, we discuss our results (Sect. 3.5) and we briefly summarize the future work on mid-infrared interferometric observations of massive young stellar objects (Sect. 3.6).

3.1 Brief introduction to interferometry

Interferometry is the technique of synthesizing large apertures by combining light beams from two or more small telescopes. In this way, the achievable angular resolution is not anymore limited by the diameter of a single telescope but only by the maximum distance between the telescopes.
The basis of interferometry lies in the description of the correlations between electric fields in the Fourier space (see e.g. Monnier 2003 for more details). The main ideas can be summarized as follows:

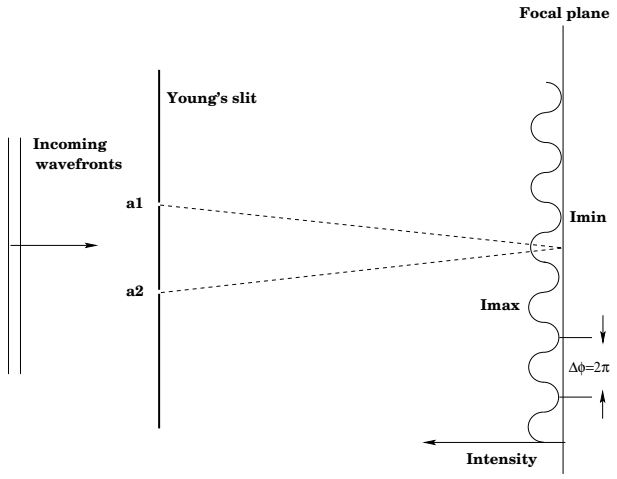

Figure 3.1: Scheme of the Young's slit experiment. Light from the left passes a screen with two small apertures, a1 and a2. On the focal plane the detector registers the characteristic fringe pattern, maxima alternate to minima with a shift of $\Delta\phi$.

I) Each astronomical source can be described as the superimposition of co-sinusoids (Fourier components of the source brightness) each of which corresponds to a particular spatial frequency or angular scale in the sky. II) The spatial coherence function describes the correlation of the electric fields from a distant astronomical source and is the quantity measured by interferometers. III) The van Cittert-Zernike theorem states that the normalized Fourier transform of the sky brightness distribution is equal to the normalized value of the spatial coherence function. Thus, *interferometers measure the different components of the Fourier transform of the source brightness.* When the Fourier space is well sampled, the Fourier transform of the coherence function is an adequate representation of the source brigthness. As example, the simplest interferometer made of two telescopes separated by a distance B, usually called baseline, and observing at a wavelength λ measures the value of the Fourier transform of the source brightness distribution at a spatial frequency $u = \frac{B}{\lambda}$.
A simple way to illustrate how interferometry works in practise is to consider the Young's slit experiment (see Fig. 3.1). The incoming wavefronts are intercepted by a screen with two small apertures and after are focused to a distant screen. We call the electric fields at the small apertures E_1 and E_2. Then, the intensity at the focal plane will be the modulus square of the total electric field (E_1+E_2). The time averaged intensity can be written as:

$$< (E_1 + E_2) \times (E_1 + E_2)^* >=< (E_1)^2 > + < (E_2)^2 > + < 2E_1\, E_2\, cos(\phi) > \qquad (3.1)$$

where ϕ is the phase difference between E_1 and E_2. Equation 3.1 shows that the intensity consists of two parts: a constant term given by the sum of the intensities from each small aperture and an oscillating tem which is related to the spatial coherence function. This last term gives rise to the characteristic fringe patters, maxima of intensity alternated by minima. The modulation of the fringe pattern is expressed as:

$$V = \frac{[I_{\rm max} - I_{\rm min}]}{[I_{\rm max} + I_{\rm min}]} \qquad (3.2)$$

where $I_{\rm max}$ abd $I_{\rm min}$ are the maximum and minimum intensities. The phase of the fringe pattern is the location of the white-light fringe relative to some reference point. These two

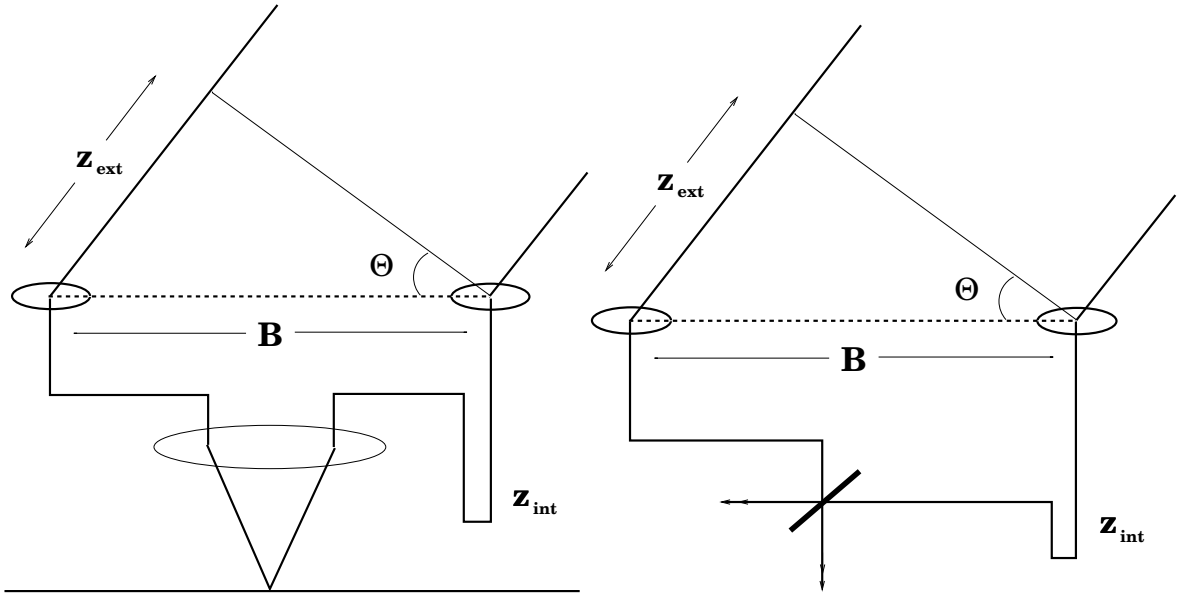

Figure 3.2: Schemes of the two beam combinations. Shown are the external and internal path differences ($z_{\rm ext}$, $z_{\rm int}$) and the baseline B. Left: Image-plane combination. Both beams are focused to the detector. Right: Pupil-plane combination. The beam splitter splits the beam and the two parallel beams are combined to individual pixels.

quantities (V and phase of the fringe pattern) encode the amplitude and phase of the spatial coherence function, also known as visibility function.
Now that we have seen how interferometry works, we briefly introduce the two main beam combination schemes for homodyne (direct) interferometry: the image- and the pupil-plane combination. In the first scheme, the beam is focused to make an image of the sky, the images are superimposed so that interference fringes form across the combined image. The interferometers who use this method of combining beams are also known as Fizeau interferometers. In the pupil-plane combination, one of the beam passes through a beam splitter and only after the parallel beams are superimposed on single detector pixels. This kind of interferometer is also known as Michelson interferometer. The two ways of beam combination are schematically shown in Fig. 3.2 (see e.g. Traub 2000 for a more detailed description).

3.2 MIDI: The mid-infrared interferometer for the VLTI

In this section, we briefly describe the mid-infrared instrument MIDI designed for the ESO Very Large Telescope Interferometer (VLTI). MIDI makes direct interferometry by combining the light from two telescopes, the Unit (UTs) or the Auxiliary (ATs) VLT telescopes, at a time. The beam combination occurs like in the classical Michelson interferometer (see Fig. 3.2 right panel). The longest available baseline of 200 m (with the ATs) allows to reach a resolution[1] as high as 10 mas at 10 μm. In addition, the large aperture of the UTs coupled with the MIDI design permit to achieve a point source sensitivity of 1 Jy in self fringe tracking mode and of 10 mJy with external fringe tracking. Currently MIDI operates in the N band between 8 and

[1] The resolution is defined as the first zero of the visibility in the uniform disk assumption

13 μm, in the future the wavelength coverage will be extended to the Q band (17–26 μm). The spectral resolution can be chosen by inserting different filters or a prism (resolution $\lambda/\Delta\lambda \sim$30) or a grism (up to $\lambda/\Delta\lambda \sim$270) in the parallel beam after beam combination.
The optical layout of MIDI is schematically shown in Fig. 3.3. Since the thermal radiation from the environment is critical at 10 μm, most of the optics have to be kept at cryogenic temperatures: all the optical components of the cold bench are cooled down to 40 K, the detector is kept at a temperature of 5 K. Mechanical and reflective optics parts are made of the same material to preserve the alignment of the optical paths during the cooldown. From the left of Fig. 3.3, the beams from two UTs/ATs enter the MIDI cryostat (cold box) through the entrance window (Dewar window). A cold pupil stop suppresses the thermal emission from outside the beams and a first focus is formed just after to introduce different masks or spatial filters. Next, the beams combine on the surface of the beam splitter with 50% transmission-reflection coefficients. The beams (four if the photometric beam splitter is in the beam, two otherwise) pass a filter wheel and dispersive elements and are focused on the detector. The detector has 320×240 pixels (320 pixels in the direction of the dispersion) and is read-out row by row with the possibility of windowing by selecting out only some of the rows. In the following sections, we will use the nomenclature I1 and I2 for two of such windows on the detector.
The fringe modulation is done by scanning the fringe packet with the piezo-mounted mirrors within MIDI. Two scanning modes are available: I) The Fourier mode, in which more fringes are scanned and the squared fringe contrast is obtained by integrating the scan power spectral density II) The ABCD mode, in which the central fringe is measured at regular intervals $\lambda/4$ and the squared fringe contrast is the sum of the squared amplitudes of the two quadratures. This last mode can be used only in combination with the external fringe tracker FINITO which stabilizes the fringes. At the moment only the Fourier mode is available.
More details on the MIDI instrument can be found in Leinert et al. (2003a,b), and at the following web page: http://www.mpia.de/MIDI/index.html.

3.3 The first massive star observed with MIDI

M8E IR (GL 2059) is a bright and compact MIR source probably part of the Lagoon Nebula, M8 (Wright et al. 1977). This locates the object at a distance of 1.8±0.2 kpc (e.g. van Altena and Jones 1972, Humphreys 1978, Plume et al. 1992), in the Sagittarius-Carina arm of our galaxy. The broad-band energy distribution and infrared recombination line spectrum of M8E IR are similar to the Becklin-Neugebauer object in Orion. Simon et al. (1984) estimate that M8E IR harbors a young star which is approximately of B0 spectral type, if on the zero-age main sequence.
Interesting insights on the nature of M8E IR have been reached during the lunar occultations of 1983 (Simon et al. 1985). These observations at 3.8 and 10 μm revealed two distinct components: the small one is clearly asymmetric (about 6 mas FWHM) and dominates the 3.8 μm flux while the large component is about 100 mas and has a more spherical shape. The two components contribute almost in the same amount to the 10 μm flux. Results from three different position angles led to the conclusion that the 6 mas asymmetric emission originates from a circumstellar disk seen nearly edge-on. More uncertain is the nature of the large component, which might be emission from the outer optically thin part of the disk or from the warm inner regions of the molecular cloud surrounding M8E IR. To account for the

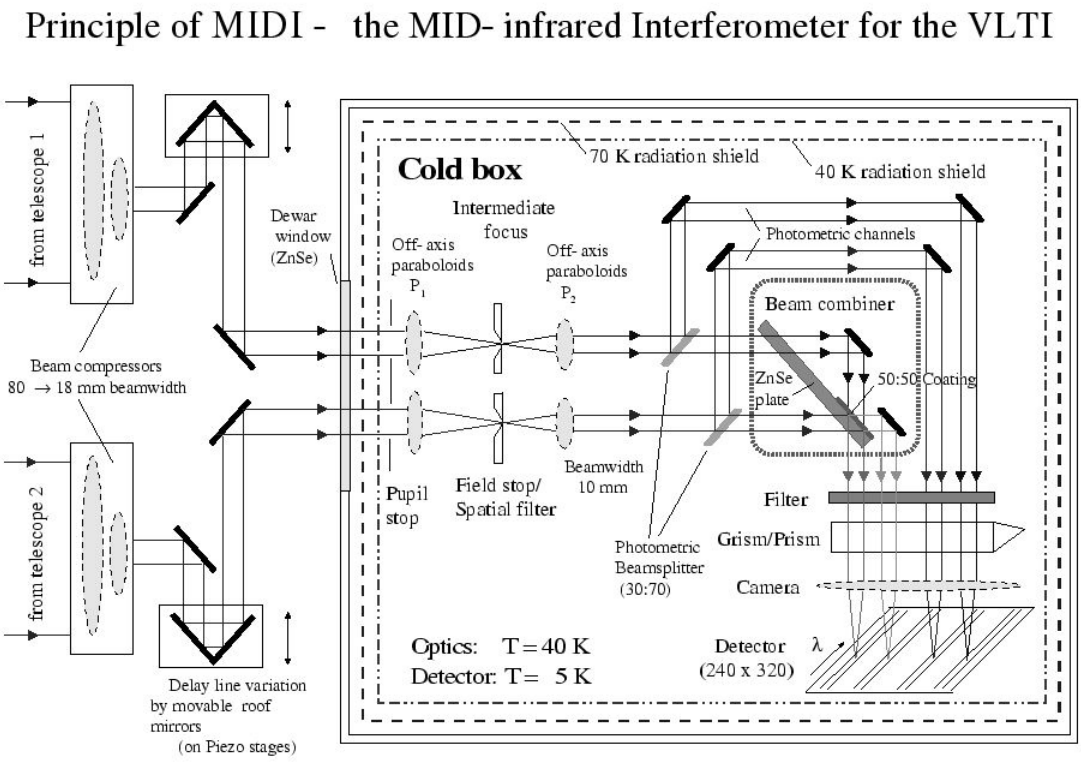

Figure 3.3: Optical concept of MIDI.

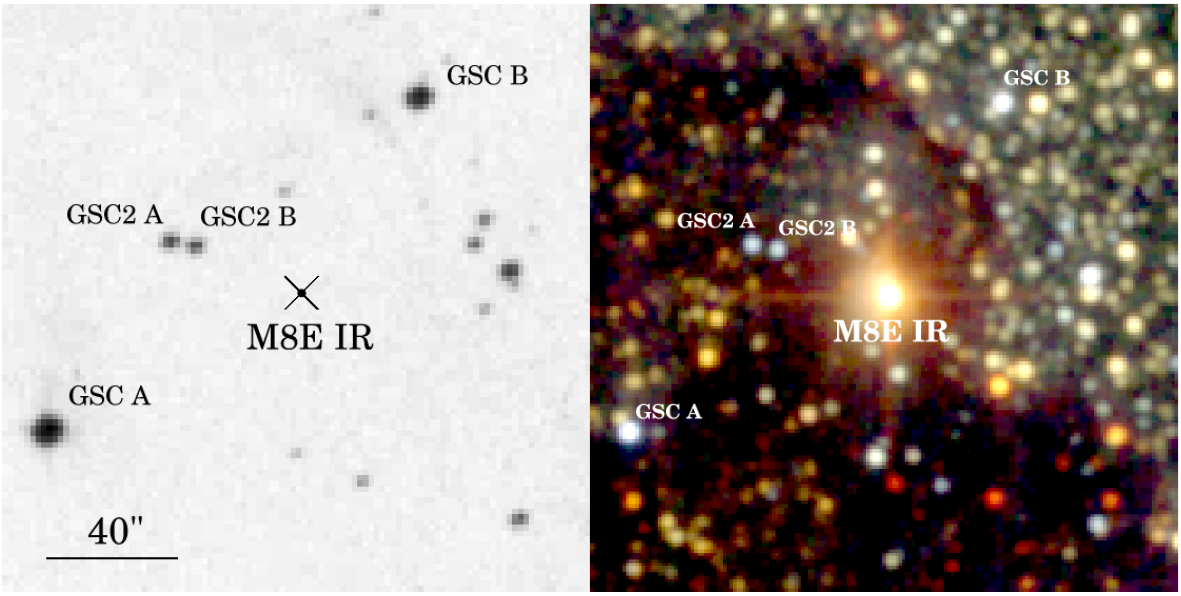

Figure 3.4: The $3' \times 3'$ field centered on our target M8E IR. Left: Optical image from the Digitized Sky Survey. Right: True color composite obtained from the J(blue), H(green) and K(red) 2 MASS Quick Look Atlas Images. Stars brighter than 16 mag in the visual are indicated: their location and magnitudes are extracted from the Guide Star Catalogue, Versions 1 and 2. The immediate surrounding of M8E IR populate with bright sources in the near-infrared regime.

observed infrared flux, Simon et al. (1985) estimate a disk major axis of about 72 mas.
Later K-band pupil mask interferometry by Löwe et al. (1997) resolved M8E IR in the north-south direction with an extended component to the south. These new results are consistent with the findings of Simon et al. (1985). However, Löwe et al. (1997) suggest a different scenario taking also into account the CO radio line measurements of Mitchell et al. (1992). Since the CO line traces an outflow whose position angle coincides with the elongation found in the infrared regime, Löwe et al. (1997) propose that the structures claimed to be a disk by Simon et al. (1985) could instead be scattered light in the innermost regions of the outflow lobes.
New high resolution infrared observations are necessary to better understand the connection between the outflow and the predicted disk. Scales of 10–100 mas are only accessible in the MIR regime with the new ESO interferometer MIDI. Our main goal here is to determine the extension and structure of the MIR emission.

3.4 Observations and data reduction

The observations were carried out on the 13th of June 2003 during the first nights of MIDI Guaranteed Time Observations. The two involved VLTI Unit Telescopes (UTs) were the UT1 and UT3 which provide a baseline of 102 m. The typical MIDI observing sequence includes: I) Coarse target acquisition by the telescope. II) Mid-infrared images with MIDI. III) Maximization of the images overlap. IV) Interferometric measurements. V) Photometry. The target acquisition starts by moving the telescope to the target coordinates at present

time then tracking and Coudé–guiding. The standard procedure uses the STRAP units (in the Coudé tunnel) on source to accurately position the target in the MIDI field of view. This can be only done if the target has a magnitude lower than 16 in the optical. During the observation, the STRAP units also correct for the first order of atmospheric turbulence (tip-tilt correction). However, the STRAP units could not be used for M8E IR because it is much fainter than 16 mag in the visual. In Fig. 3.4 we show the $3' \times 3'$ field centered on M8E IR in the V band (Digital Sky survey) and a true color near-infrared image (2 MASS Quick Look Atlas). The closest stars brighter than 16 mag in V are located at about $40''$ from M8E IR and are only $\sim$14 mag in V (stars from the Guide Star Catalogue 2, Version 2.2.01). Other two stars brighter than 12 mag in V are more than $1'$ from M8E IR (stars from the Guide Star Catalogue at ESO, http://archive.eso.org/gsc/gsc). The target acquisition of M8E IR was quite difficult and was based on the target coordinates and on the location of bright stars in the large field used for the telescope guiding. No tip-tilt correction was applied during the observation.

After the target acquisition, MIR images have been taken in the short wave N band filter (8.7 μm central wavelength and 1.4 μm width) with a chopping through of $10''$. These images from both photometric channels (A from UT1 and B from UT3) are used to shift the target to the central pixel of the MIDI camera and thus maximize the beam combination. To acquire interferometric measurements the beam combiner and the low resolution prism ($\lambda/\Delta\lambda$ about 30) are introduced into the optical train. After having found the location of the zero optical path difference (OPD) by moving the VLTI delay lines, visibility measurements are started in the self-fringe tracking mode. We acquired 12000 frames (400 scans[2]) with an integration time per frame of 4 ms by default in order to avoid background saturation. The baseline B projected on the sky had an extension of 76 m and a position angle (P.A.) of 43.5°. A sketch of the baseline projection with respect to the molecular outflow by Mitchell et al. (1992) is given in Fig. 3.5 superimposed on the 8.7 μm acquisition image (sky subtracted) of M8E IR. The figure shows that we were observing almost in the direction perpendicular to the outflow, i.e. parallel to the major axis of the predicted disk.

During the fringe searching and tracking the chopping is not used. Before closing the observing sequence additional photometric data are acquired by blocking the light first from one of the telescope and then from the other telescope and not removing the beam splitter. In this way, the incoming light from each channel is registered on I1 as well as on I2 and the effect of the beam splitter on the light propagation can be taken into account during the data reduction. Here, the chopping procedure is used again to subtract sky and background.

The star HD 168454 was observed just before and after our target to provide the instrumental visibility curve and properly calibrate the visibility from M8E IR. HD 168454 is a good calibrator because it is bright (62 Jy at 12 μm, IRAS flux) and unresolved (5.78 mas in diameter) in the MIR regime. For HD 168454 observations were tip-tilt corrected. The effect of the tip-tilt correction on the visibility measurements will be treated in Sect. 3.4.1.

The data reduction of the interferometric data is performed using a custom IDL software written by R. Köhler and O. Chesneau. In the following, we describe its main steps:

1. *Files selection.* Three files have to be selected to reduce each visibility point measurement: the file recording the fringes and the two spectra taken after the fringe tracking.

2. *Creating the mask to extract the fringes.* At this point only the spectra are used. First,

[2]a scan corresponds to the movement of the piezo through the OPD

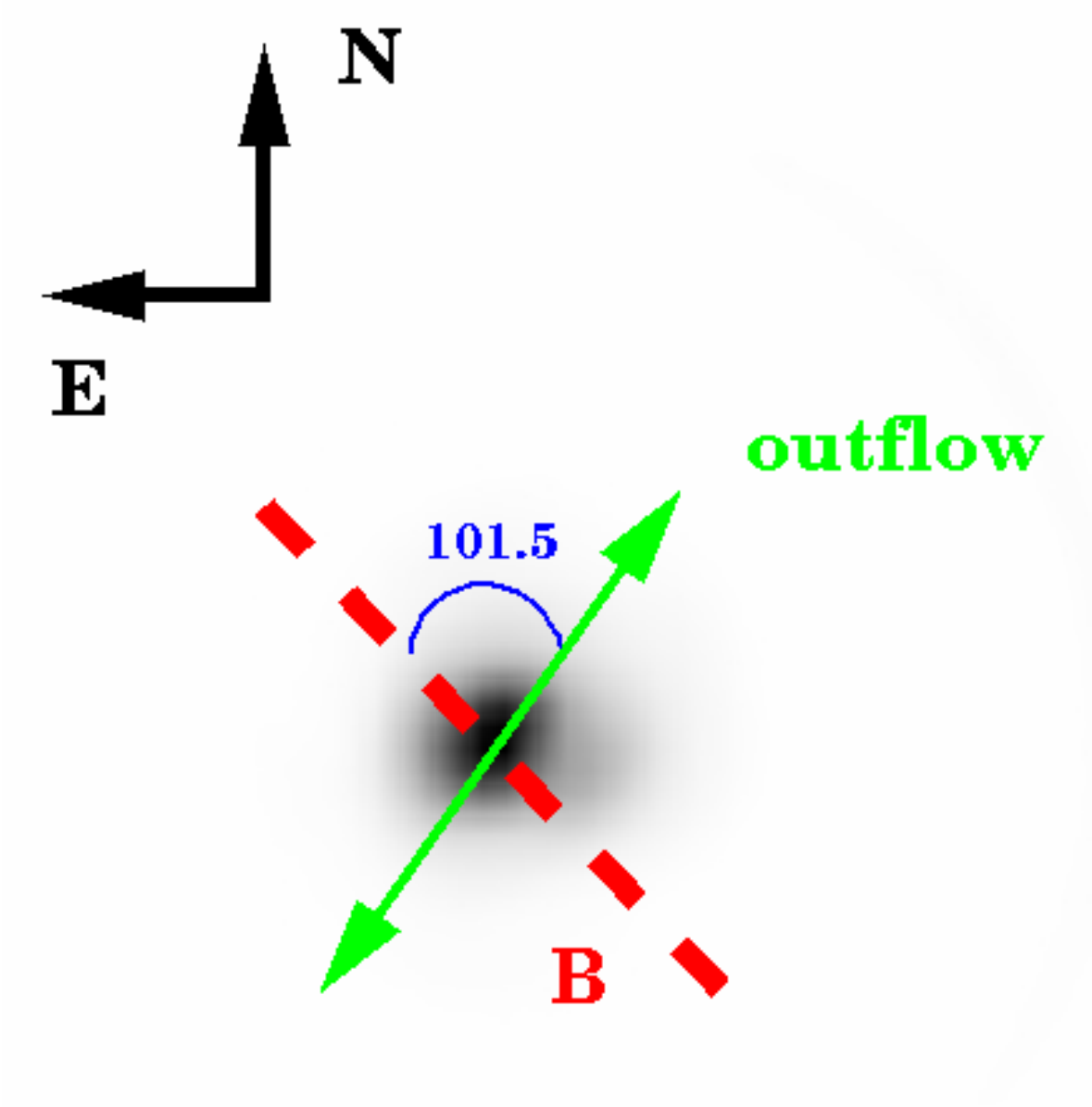

Figure 3.5: Acquisition image of M8E IR at 8.7 μm obtained with a simple co-addition of all the sky subtracted on-source frames. The extension of the source in east-west direction is an artifact due to atmospheric turbolence as discussed in Sects. 3.4 and 3.5.1. The purpose of this image is merely to show the orientation of the projected baseline B (red dashed line) in respect to the CO outflow by Mitchell et al. (1992) in green. The angle between the projected baseline and the outflow direction is 101.5°.

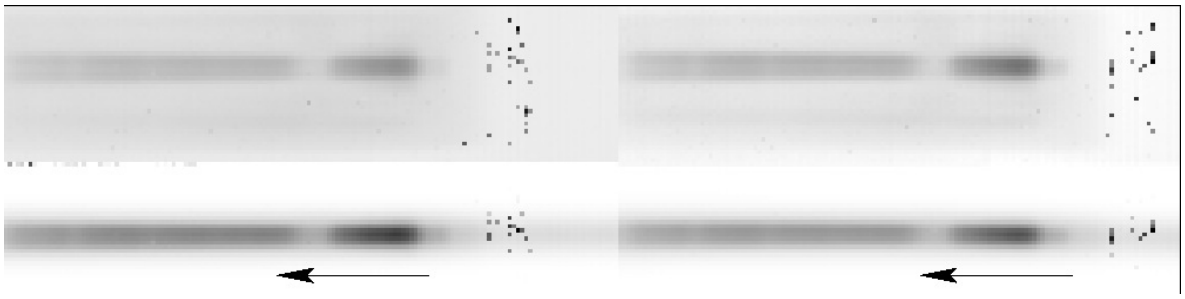

Figure 3.6: Use of the masks to extract the visibilities. The upper panels show the mean of the interferometric data on the two windows I1 and I2. The lower panels are the data from the upper panels multiplied by the masks created from the spectrometric data. The wavelength increases from right to left as indicated by the black arrow. Some bad pixels are present around 5 μm.

the program averages the frames on the target and the frames on the sky, then the average sky frame is subtracted from the average target frame. The next step is to fit a Gaussian profile to each column pixel (y-axis). The location of the Gaussian peak position in function of the wavelength (x-axis) is fitted by a quadratic polynomial. The width of the Gaussian is fitted by a linear function. In this way a mask is created for both windows I1 and I2 and for both photometric datasets A and B. The final masks for I1 and I2 contain in each column the average position and width of the spectra from the photometric channels A and B.

3. *Extracting the correlated flux.* Each frame of the fringe data is multiplied by the corresponding mask calculated in the previous step (see also Fig. 3.6) and integrated in the direction perpendicular to the spectral dispersion (y-axis). Then the fringe data recorded on I1 are subtracted from those recorded on I2. This operation allows to extract a quantity proportional to the correlated flux.

4. *FFT and Power spectrum.* The spectra from each scan (1 scan is 30 frames in our case) are Fourier transformed from OPD to frequency space and the corresponding power spectrum is computed for each frequency. To improve the signal to noise the spectra are binned by four wavelength pixels.

5. *Scan selection.* To select the scans with fringes, the histogram of all amplitudes found after integration over all wavelengths is checked. The threshold of integration can be also chosen interactively.

6. *Visibility computation.* The integration mentioned in the previous step provides the correlated flux. The visibility is obtained by dividing the correlated flux with the photometric flux (normalized visibility).

We also carefully analyze the 8.7 μm acquisition image obtained just before the interferometric measurements to check whether the circumstellar material around M8E IR is resolved by the unit telescopes. A self–developed IDL routine processes the single-dish data as follows:

1. The individual frames are extracted and subdivided into on target (T), on sky (S) and undefined (U). The U frames are obtained while the telescope is moving from S to T and vice versa and are therefore excluded from further processing.

2. The S frames are averaged to obtain a mean sky frame. The mean sky frame is subtracted from the individual T frames.

3. The sky–subtracted T frames are further selected based on the target FWHM. First, we compute the minimum FWHM (minFW) and the standard deviation (σ) of the FWHM distribution and then we select only those frames with target FWHM smaller than (minFW+2$\times\sigma$). With this selection criteria from 40% up to 70% of the T frames can be rejected.

4. Finally, the selected sky–subtracted T frames are cross-correlated and averaged.

This procedure is applied to the M8E IR data set as well as to the frames from the calibrator observed before and after M8E IR. We note that the individual frames have an exposure time of only 4 ms, 50 times shorter than the typical time of atmospheric stability at Paranal in the MIR regime. The frames co-addition only after cross-correlation removes blurring in the final image that are caused by the object's motion in the field of view due to atmospheric turbolence. The resulting 8.7 μm acquisition images of M8E IR and its calibrator are presented and discussed in Sect. 3.5.1.

3.4.1 Effect of tip-tilt correction on visibility measurements

The STRAP units correct for the first order of atmospheric turbolence and stabilize the location and FWHM of the observed sources. This is important for visibility measurements because a displacement in the location and/or a larger FWHM of the source can result in a poor overlapping of the beams from the two telescopes. Thus, in general we would expect that uncalibrated visibilities from a source observed without tip-tilt correction are smaller than those of the same source observed with active STRAP units. In our case, this consideration might imply that the calibrated visibilities of M8E IR will be underestimated.
To check in a more quantitative way the effect of tip-tilt correction, we analyze the dispersed frames obtained after the visibility measurements. In particular we measure the shifts in position with wavelength and changes in the FWHM both for M8E IR and the calibrator HD 168454 observed before (Cal1) and after (Cal2) our target. The results are summarized in Fig. 3.7. The beam overlapping from Cal2 is very good (dashed lines in the lower panels of Fig. 3.7). However, the FWHM of the source from the beam B is noisy at short wavelengths. The opposite happens for Cal1: The mean peak position of the two beams is separated by about 2 pixels (not good beam overlapping) but the FWHM of the source from the two beams is consistent and decreases, as expected, towards short wavelengths. This already suggests that *the use of the STRAP units not always can guarantee good beam overlapping and stable FWHMs*. Similar analysis has been independently performed on different calibrators observed during the year with similar results. We note here that the FWHM of the Point Spread Function is about 4 pixels in the range 8–13 μm with a sigma of 2 pixels. Thus, even for a separation in peak positions of 2 pixels the two beams partially overlap and visibility data can be extracted (see also the discussion of the Cal1 visibility curve in the next section). For our target (solid lines in Fig. 3.7), we find that the beam overlapping is worse than for Cal2 but better than for Cal1. The FWHM of M8E IR is always larger than the FWHM of the calibrators, thus suggesting that our source might be already resolved by the unit telescopes. This possibility will be further discussed in Sect. 3.5.

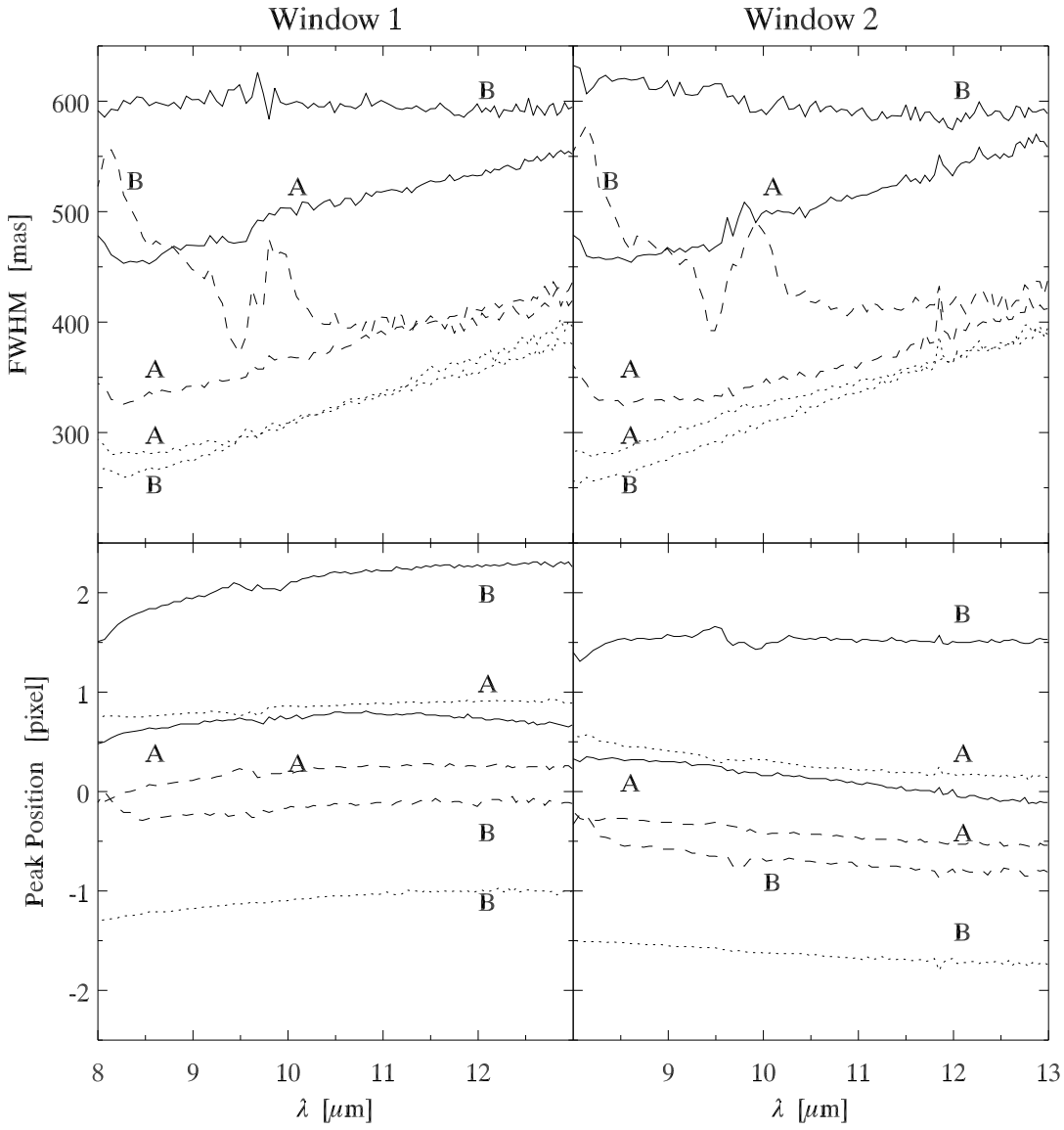

Figure 3.7: Analysis of the beam overlapping and FWHM for our target and the calibrator HD 168454. The two left panels are relative to the Window 1 (I1) of the camera, the right ones to the Window 2 (I2). Solid lines provide results for M8E IR, dotted lines for HD 168454 observed before M8E IR (Cal1) and dashed lines for HD 168454 observed after M8E IR (Cal2). The FWHM is measured in milliarcsecond, the peak position is derived from a 1D Gaussian fit at the sampled wavelengths. In each window we compare the incoming light from the two unit telescopes (Beam A for the UT1 and Beam B for the UT3).

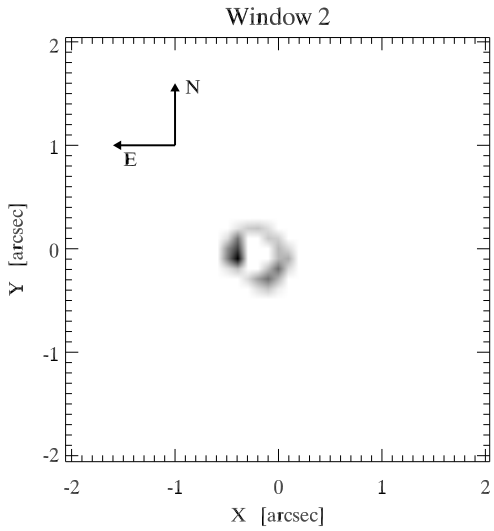

Figure 3.8: PSF-subtracted image of M8E IR. Only counts larger than 10 times the mean background are plotted. M8E IR is clearly resolved by the unit telescopes.

3.5 Results and discussion

In the following sections we discuss our single-dish and interferometric data and draw conclusions on the extension of the dust surrounding M8E IR.

3.5.1 Single-dish data

We reduce the acquisition images of M8E IR and its calibrator following the procedure described in Sect. 3.4. The selection criteria we adopt exclude from further processing those frames that have been acquired while the telescope was still moving. Because of atmospheric instability and imperfect chopping, the position of the target is slightly different from frame to frame. A simple co-addition of all the acquired frames results in blurring and fictitious elongation in the final image, see Fig. 3.5 of M8E IR. Our approach of cross-correlating the selected frames before co-addition removes any of these artifacts.
To determine whether M8E IR is resolved by the single UTs, we compare its acquisition images with those from the calibrator HD 168454, whose diameter in the MIR is estimated to be only 5.78 mas. However, due to a worsening in the atmospheric conditions the first one third of the frames are of better quality than the others. The "better quality" frames include all the Cal1 8.7μm frames and the first 5000 frames of M8E IR. The PSF of Cal2 appears slightly elongated in east-west direction and the first Airy ring is not clearly visible in all the frames. In addition, we note that the images from Window 2 (UT1) are in general of better quality (less vignetting, lower background, rounder PSFs) than those from Window 1 (UT3). This difference is mainly due to the extra-path in the VLTI interferometric tunnel that light, collected from the UT3, crosses before reaching the detector.
Taking into account the discussed differences in image quality, we compare the first 5000 frames of M8E IR only with the acquisition images of Cal1, the other 10000 frames of M8E

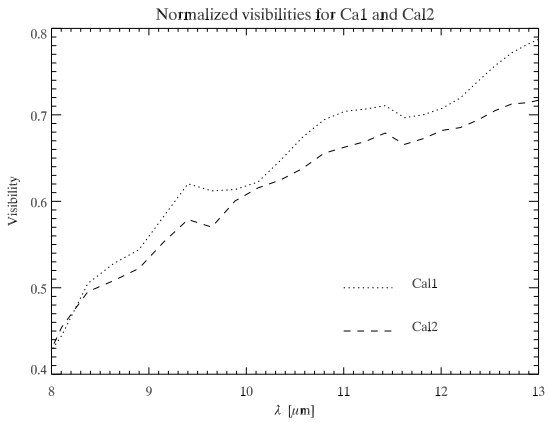

Figure 3.9: Instrumental visibility curve. Normalized visibility measurements of the calibrator HD 168454 observed before (dotted line) and after (dashed line) M8E IR.

IR only with the images from Cal2 and we keep separate results from Window 1 and Window 2. A firm result from the different comparisons is that *M8E IR is resolved by the unit telescopes.* This confirms the existence of a warm envelope with sizes of 100–200 mas, these sizes translate into 180–360 AU at the distance of 1.8 kpc. We also find that the envelope is slightly more elongated in the east-west direction. To illustrate these results we show in Fig. 3.8 the PSF subtracted image of M8E IR obtained from the most reliable data set, i.e. light collected from the UT1, the calibrator Cal1 and only the first 5000 frames of M8E IR. Before subraction, the Cal1 and M8E IR images have been scaled using the ratio of the fluxes collected within a radius of 3 times the FWHM of Cal1.

3.5.2 Interferometric data

We adopt the data reduction described in Sect. 3.4 to independently extract normalized visibility curves for M8E IR and its calibrator in the wavelenght range between 8 and 13 μm. Before presenting our results, we further check the quality of our data, we correct for intrumental effects in the visibility curve and prove the robustness of the calibrated visibility curve.

The data quality is checked with the following two step procedure: i) We compare the instrumental visibility of all the calibrators observed during the same night ii) We check the stability of our calibrator and target by measuring the scatter in the fourier fringe amplitude. From analysis i), we derive that the standard deviations between the instrumental visibility curves of the calibrators (8 calibrators, 4 of which different) of the same night is only 7%, that classify the night as "good" for MIDI observations. In addition, we find that the standard deviation of the fourier fringe amplitude of M8E IR is comparable with that of its calibrator. We can therefore conclude that the *quality of the visibility data is good.*

In Fig. 3.9 we plot the instrumental visibilities from Cal1 and Cal2. The two curves show the same behaviour as a function of wavelength: The increasing visibility values towards long wavelenghts are expected for an unresolved source. The exact value of each visibility point is slightly larger for Cal1 than for Cal2.

We correct for instrumental effects by dividing the normalized visibility curve of M8E IR with that of its calibrator. The result is shown in Fig. 3.10 left panel: The two visibility

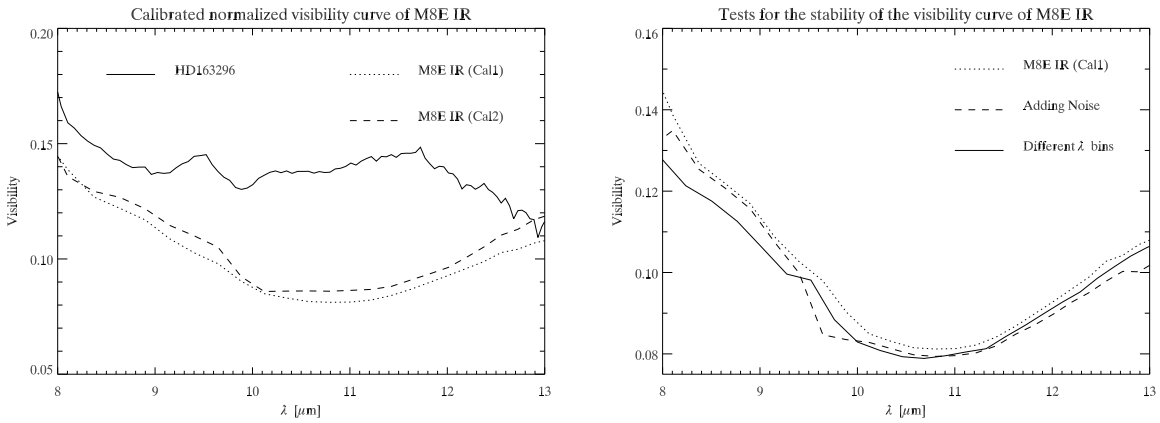

Figure 3.10: Visibility measurement of M8E IR. Left panel: Visibility curves from M8E IR calibrated with the star HD168454 observed before (dotted line) and after (dashed line) our target. To illustrate the difference between the shape of the visibility curve from M8E IR and that from a typical Herbig Ae star, we superimpose the calibrated visibility curve (scaled by a factor of 1.5) of HD163296 (solid line). Right panel: Tests to check the robustness of the visibility curve of M8E IR. The curves are calibrated using Cal1. Dotted line is the same as in the left panel. Dashed line is the visibility curve obtained by adding a noise calculated from scans at an OPD distance larger than 300 μm (30×10 μm). The solid line provides the visibility curve for a different binning in wavelenghts: Step in spacing between columns equal to 4 and number of columns added in one bin equal to 8 (the standard is 4).

curves of M8E IR are calibrated with HD 168454 observed just before (dotted line) and after (dashed line) our target. We discussed in Sect. 3.4.1 the quality of the data in term of beam overlapping and variation of the FWHM. We also noted that the use of the STRAP units does not necessarily guarantee a good beam overlapping (the case of Cal1) or a stable FWHM (the case of Cal2). The stability of the two calibrators, also compared with other calibrators in the same night, give us confidence on the shape and absolute values of the plotted visibility curve for M8E IR. We estimate an error of 10% on each visibility point that is the maximum deviation between the two curves calibrated with Cal1 and Cal2. This value is close to the accuracy of MIDI visibility measurements estimated on different sources (Leinert et al. 2004).

The robustness of the calibrated visibility curve of M8E IR is further controlled by applying the following tests: i) We set a threshold for good and bad scans. ii) We vary the binning in wavelenghts. Test i) means that we add a noise to the visibility measurements. We define a minimum distance in OPD from the median OPD (threshold) and we calculate the noise as the mean of all scans that have an OPD larger than the threshold. Setting a threshold larger than 400 μm (40×10 μm), does not produce significant differences with the curve computed without noise (difference smaller than 7% for all the sampled wavelenghts but the 9.6 μm where the difference amounts to 14%). For a threshold at 300 μm differences become larger but the main characteristics in the shape of the visibility curve are not affected (see Fig. 3.10 right panel). With test ii) we vary the binning in wavelenghts and their grouping. The standard procedure groups 4 wavelenghts (about the PSF) to provide a visibility point. We add together up to 8 columns spaced by 4 wavelenghts: At shorth wavelenghts the calibrated visibility curve is lower but its shape is not strongly affected (see Fig. 3.10 right panel).

All these tests prove that the shape of the calibrated visibility curve and the low visibility values measured for M8E IR are a robust result. Thus, we can firmly conclude that *M8E IR is well resolved in the mid-infrared regime by MIDI.* Considering the baseline orientation in respect to the molecular outflow by Mitchell et al. (1992),it is very likely that we are resolving the reprocessed infrared emission from the circumstellar material, possibly a disk.
The visibility curve slightly decreases towards long wavelengths, reaches the minimum of 0.08 between 10 and 11.5 μm and then increases again. This behaviour is different from that shown by Herbig Ae stars (Leinert et al. 2004) : Where the visibility curve of M8E IR has a well that of Herbig Ae stars has a bump. To illustrate this difference we overplot in Fig. 3.10 left panel the calibrated visibility curve from the Herbig Ae star HD163296. The difference in the shape of the visibility curve has to be sought in the origin of the MIR emission. In the case of intermediate mass stars, most of the MIR emission is emitted in the optically thin upper layer of their flared disks and their MIR spectra are usually characterized by prominent silicate emission features around 10 and 20 μm. The same silicate features are often observed in absorption towards massive stars and very little is known about the distribution of their circumstellar dust. Optical depth effects, geometry and extension of the circumstellar material might be all influencing the shape of the visibility curve. Understanding what plays a major role requires at least an additional observation with a perpendicular baseline orientation to constrain the dust geometry and detailed radiative transfer modeling of the circumstellar material.
Our aim here is to analyze the extension of the MIR emission and compare it with results from previous high-resolution observations. For the sake of simplicity, we approximate the source brightness with a Gaussian distribution. The expression for a normalized Gaussian with mean 0 is

$$f(x) = \frac{1}{\sigma\sqrt{2\pi}}\, e^{-x^2/2\,\sigma^2} \tag{3.3}$$

where σ^2 is the variance of the distribution. When we introduce the $FWHM$ in equation 3.3 and we make its Fourier Transform, we obtain

$$V(u) = exp(-3.56\ u^2\ FWHM^2) \tag{3.4}$$

where u is the spatial frequency defined as λ/B, B being the modulus of the baseline projected on the sky (76 m in our case). From equation 3.4 and the measured visibilities, we calculate the extension of the correlated MIR emission in the observed wavelength range (see Fig. 3.11). The two curves, obtained from the visibility calibrated with Cal 1 (dotted line) and Cal2 (dashed line), deviate less than 3%. The FWHM increases always with the wavelength, more steeply between 10 and 12 μm.
This *increase of the effective size of the MIR emitting region* is probably the result of a temperature gradient along the circumstellar material. We note a small decline of the FWHM after 12.5 μm possibly indicating that the correlated MIR flux is confined to the inner 28 mas, 50 AU at the distance of M8E IR. These linear dimensions are at least 10 times larger than those probed around Herbig Ae stars by MIDI (Leinert et al. 2004). The larger extension of the MIR emission could be due to a less steep density gradient and a larger dust evacuated region compared with the density distributions and inner radii of disks around intermediate mass stars. This explanation is also in agreement with first 1D radiative transfer simulations of the circumstellar material around massive stars in the UCH II phase (see also Sect. 2.10.3 for an example).

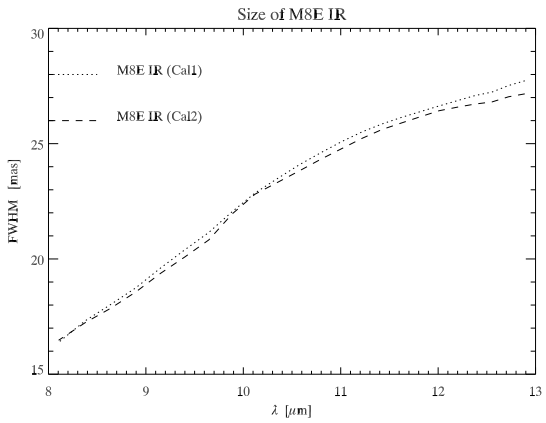

Figure 3.11: Extension of M8E IR at different wavelengths. The dotted and dashed curves originate from the calibrator observed before and after our target.

With the projected baseline of 76 m we probe dimensions between 15 and 30 mas in a direction almost perpendicular to the molecular outflow by Mitchell et al. (1992). These sizes well agree with the width to 1% intensity at 10 μm of the small component by Simon et al. (1985). We note that the lunar occultation of July 1983 occurred in a direction almost parallel to that of our projected baseline. However, while our low visibility values suggest that the correlated flux is not more than 15% of the total flux, Simon et al. (1985) suggest that the small component contributes to about half of the N-band flux.

3.6 Summary and perspective

In this Chapter, we demonstrated that MIR interferometry is a novel and powerful tool to probe the close vicinity of massive stars. The resolution reached with MIDI is better than 30 times that of 8-m class telescopes at the same wavelenght. Thus, MIDI allows to explore the sizes at which circumstellar disks and companions around young massive stars are expected. However, MIDI only provides visibility curves that need careful modelling to be correctly interpreted. In particular, we point out that at least two visibility measurements with almost perpendicular baselines are needed to constrain the geometry of circumstellar dust.
The first observations of the massive star M8E IR led to the following main results:

1. The 8.7 μm acquisition images show that the MIR emission of M8E IR is resolved by the unit telescopes. The emission in the E–W direction looks slightly more elongated. No mid-infrared companions are detected in the 2″ field of view of MIDI.

2. We obtained good quality visibility data for M8E IR in the range 8–13 μm and we estimate an error of about 10% on each visibility measurement.

3. The low visibility values prove that *M8E IR is well resolved by MIDI and the observed correlated flux is about 10% of the total flux.*

4. Using a simple Gaussian brigthness distribution, we derive FWHM for M8E IR between 15 and 30 mas that correspond to linear sizes of about 30–50 AU at the distance of

1.8 kpc. These dimensions compare well with those reported by Simon et al. (1985) for the small component.

5. We find a *remarkable difference between the shape of the visibility curve of M8E IR and that typical of Herbig Ae stars.* Dust opacity effects as well as different geometry of the circumstellar dust can play an important role.

Additional observations of M8E IR are scheduled for June this year with a baseline orientation close to the direction of the molecular outflow. These new observations coupled with detailed radiative transfer simulations will decide whether the circumstellar dust is confined in a disk and constrain its orientation.
Other 34 massive massive young stellar objects are included in the Guaranteed Time programme with the purpose of studying their circumstellar environment and their multiplicity. The upcoming external fringe tracker FINITO will enable to extend MIDI observations to sources as faint as 10 mJy in the MIR regime and possibly probe the young and embedded phases of massive star formation discussed in the previous Chapter. Bright MIR targets will benefit from the use of the auxiliary telescopes that provide longer baselines in comparison to the unit telescopes and complementary baseline orientations.

Chapter 4

The Influence of Massive Stars on Their Surroundings

Massive stars form on relatively short timescales ($\sim 10^5$ yr) and their birth is marked by the onset of a powerful ionizing flux that renders them detectable in the radio regime as ultra-compact H II regions. In about 10^5 yr, the hot and dense gas in the ultra-compact phase expands into a larger, more diffuse and thus less obscured H II region (see also the Introduction).
In the previous Chapters, we discussed the early embedded phases of massive star formation. Here, we focus on the more evolved H II regions aiming to study the influence of massive stars on their immediate surroundings. Because evolved H II regions are characterized by much lower extinction than the early phases, they can be observed in the near-infrared regime at the high resolution provided by adaptive optics (AO) techniques recently applied on 8-m class telescopes. In this Chapter, we present observations of the Orion Nebula, the prototype for the H II phase, obtained with the adaptive optics system at the Very Large Telescope and we explore the infrared view of the direct vicinity of the ionizing star Θ^1 C Ori.

4.1 The Orion Nebula and the massive star Θ^1 C Ori

The Orion Nebula (M 42) at a distance of about 450 pc is the nearest H II region and site of ongoing massive star formation. One of its main sources of ionization is the O6p star Θ^1 C Ori in the Trapezium cluster. The extraordinary luminosity of Θ^1 C Ori has for long time prevented observations of its immediate surroundings in the optical and near-infrared (NIR) regimes.
Already two decades ago optical line emission and radio continuum observations discovered the existence of compact photoionized knots near the center of M42 (Laques and Vidal 1979; Churchwell et al. 1987; Garay et al. 1987). However, only the high-resolution and sensitivite observations from the Hubble Space Telescope (HST) revealed their nature as pre-main sequence stars surrounded by flattened circumstellar dust and gas (O'Dell et al. 1993; O'Dell and Wen 1994; O'Dell and Wong 1996). More than hundred of these objects, named proplyds, have been found in M 42 and few in other massive star forming regions (Stecklum et al. 1998; Yusef-Zadeh et al. 2000; Brandner et al. 2000; Smith et al. 2003). Those proplyds located in front of the ionized nebula, far enough to escape the ionization radiation from the massive star, reveal their circmustellar disks in silhouettes. Those lying close to the massive star

appear like ionized envelopes with bright cusps facing the massive star and tails created by escaping photo-evaporated wind. A review on the properties of proplyds in the optical regime is included in O'Dell (2001).
Observations at NIR wavelengths are also numerous towards M 42 (McCaughrean and Stauffer 1994; Simon et al. 1999; Hillenbrand and Carpenter 2000; Carpenter et al. 2001; Muench et al. 2002). However, many of them lack the spatial resolution necessary to resolve the structure of the proplyds. This problem has been recently overcome by the implementation of AO techniques on 8-m class telescopes that provide resolutions as high-as 50-70 mas that translate into 20-30 AU at the distance of Orion.
In the following we present new high-resolution NIR images of the immediate vicinity of Θ^1 C Ori obtained with the NAOS/CONICA (NACO) adaptive optics system. Archival HST images are also analyzed to provide complementary information on the NIR objects detected with NACO. Particular emphasis is given to the object Orion 163-323 which lies at only $2''$ projected distance from Θ^1 C Ori. In spite of its apparent close vicinity to the powerful O6 star, Orion 163-323 does not show any ionized tail in the narrow-band HST images. Another interesting property is its strong and compact mid-infrared (MIR) emission (Hayward et al. 1994; Robberto et al. 2002). The MIR observations led to the idea of a star and disk system being photoevaporated by the UV radiation from Θ^1 C Ori. The system, also known as SC3, has the peculiarity of being oriented face-on with respect to both Θ^1 C Ori and the Earth (Robberto et al. 2002).

4.2 Observations and data reduction

4.2.1 NACO broad-band and narrow-band imaging

The observations have been performed in December 2002 with the adaptive optics system NACO mounted on the YEPUN VLT telescope, as part of the MPIA Guaranteed Time Programme "Formation and Early Stages of High-mass Stars". Broad-band images in the J(1.265 μm), H(1.66 μm), and Ks(2.18 μm) filters together with narrow-band images in the Brγ(2.166 μm), H_2(2.122,μm), [FeII](1.26 and 1.64 μm) and continuum filters have been acquired using the highest resolution camera (pixel scale of 13.25 mas). For each filter a mosaic of 5 frames have been taken with Θ^1 C Ori at the central position. In addition, two sky frames were obtained in a separate starless field for the broad-band images and for the 10 s on source exposures in the Brγ and H_2 filters. For the same observations, the total integration time on source per filter amounts to 5 minutes. This integration time allows detecting sources as faint as 13.5 mag in Ks (main sequence star of spectral type M0). For the [FeII] filters and for the Brγ we obtained shorter exposures for a total on-source time per filter of 30 s.
The data reduction has been carried out with self-developed IDL routines following a procedure similar to that adopted to reduce the ISAAC images of G10.47+0.03 (see Sect. 2.2.4): All frames were subject to standard bad-pixel removal, flat fielding, and centering at the subpixel level before being combined in the resulting image. For photometric calibration of the broad-band images we used objects in common with the catalogue of Muench et al. (2002) because of similarities in the central wavelength and bandwidth of the filters. Standard deviations between our magnitudes and those provided by Muench et al. (2002) are 0.12, 0.16 and 0.17 mag in J, H and Ks respectively. We assume our photometry to be accurate within these uncertainties. In the absence of any calibrator to determine the exact conversion factor at the Brγ line, we scaled the conversion factor Jy/Counts from the Ks image by taking into account

the different bandwidths and throughput of the filters. A similar procedure was adopted for the other narrow-band measurements.
The AO corrections have been performed using the massive star Θ^1 C Ori as reference source for the visual wavefront sensor. Assuming a simple Kolmogorov atmosphere model and typical conditions at Paranal, an isoplanatic angle[1] of $9''$ can be reached in Ks, decreasing to $7''$ in H and $5''$ in J-band (see e.g. Stolte 2003). In our images we notice a decrease of the AO performance already for sources at distances larger than about $5''$ from the reference star Θ^1 C Ori. Therefore, we will limit our analysis to the inner $12''\times12''$ field centered on Θ^1 C Ori.

4.2.2 Archival HST images

The region surrounding Θ^1 C Ori has been extensively observed with the WFPC2 on board of HST. We retrieved the high-level science products from the Multimission Archive at Space Telescope (MAST). These products include observations from 1995 to 2001 in broad- ,medium- and narrow-band filters. The narrow-band filter images have been published in O'Dell and Wong (1996) and Bally et al. (1998) and probe the prohibited emission lines [OIII], [OI], [NII] and [SII] and the Hα line emission. For the same data set, exposures in the medium-band filter centered at 547 nm have been also acquired to remove the continuum sources from the narrow-band images. The U and B broad-band images have been obtained in March 2001 as part of the HST Proposal 8894 and are presented for the first time in this thesis. There are no observations with the WFPC2 in the broad-band filters V, R and I. For most of the filters there are exposures with the Wide Field camera and with the Planetary Camera (PC) that provides an angular resolution more than 2 times better ($0\farcs05$ pixel^{-1}). Since this resolution is comparable with that of our NACO images, we prefer to use the PC images when comparing the optical and NIR appearance of the sources.

4.3 Immediate results

4.3.1 The NACO view of the vicinity of Θ^1 C Ori

The composite image in J(blue), H(green), and Ks(red) of the central $12''$ by $12''$ is shown in Fig. 4.1. The names of the detected NIR sources follow the nomenclature scheme suggested by O'Dell and Wen (1994): The first three digits indicate the source right ascension and the second three digits indicate its declination with a box subtending $1\farcs5$ in right ascension and $1''$ in declination.
The only two stars in the field are Orion 167-325 and Θ^1 C Ori (O'Dell and Wong 1996) and are saturated in all the broad-band images and long exposure narrow-band images. Orion 167-325, also known as Θ^1 F Ori, is classified as a B8 main sequence star (Hillenbrand 1997). Θ^1 C Ori is the massive O6p star responsible for most of the ionization of the M42 nebula. An interesting result of NIR speckle observations was the discovery of a close visual companion to Θ^1 C Ori (Weigelt et al. 1999). The projected separation of the binary was between 30 and 45 mas during the 6 years timeline observations (Schertl et al. 2003). These separations correspond to ∼2–3 pixels in our high-resolution NACO images and cannot be confidently probed even in the non-saturated narrow-band exposures.

[1]The isoplanatic angle defines the maximum radial distance from the reference source within which the residual wavefront errors are smaller than 1 radian and the diffraction limit is reached.

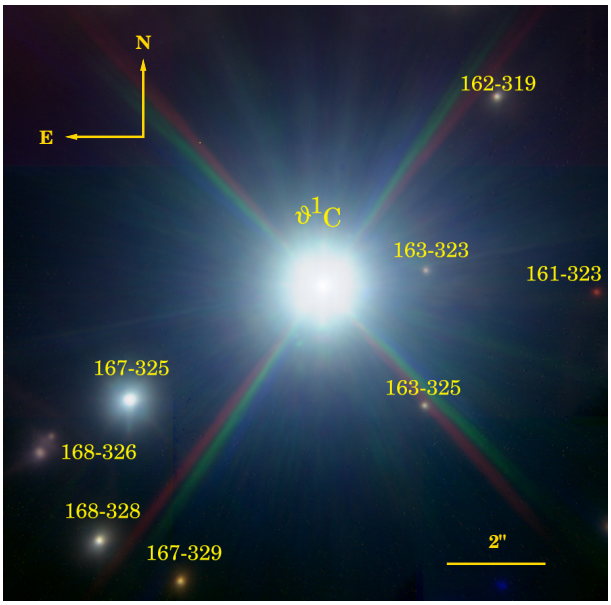

Figure 4.1: Colour composite NACO image of the $12'' \times 12''$ field centered on Θ^1 C Ori. The colour coding is blue for J, green for H and red for Ks. The nomenclature for the Orion sources follows the scheme by O'Dell and Wong (1996).

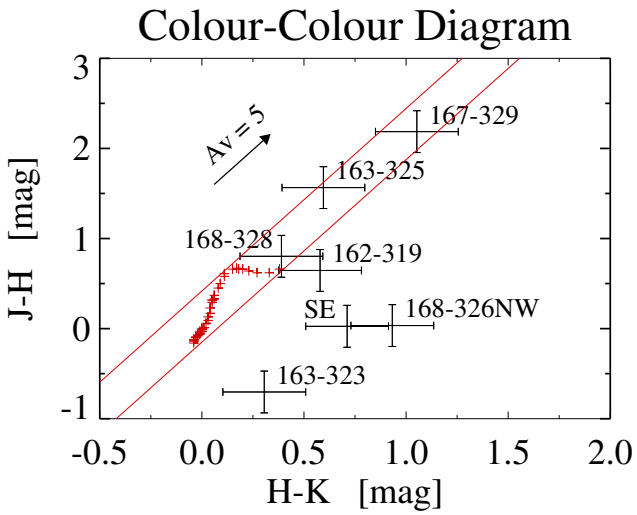

Figure 4.2: Colour-Colour Diagram of the Orion sources shown in Fig. 4.1. Red crosses represent the intrinsic colours for dwarfs (Tokunaga 2000). The two red lines bound the region of reddened main-sequence stars and are parallel to the reddening vector appropriate for the Orion nebula (R_V=5.5, Fitzpatrick 1999). The black arrow indicates a reddening of 5 mag at optical wavelengths. For the binary proplyd Orion 168-326 we use the nomenclature of Graham et al. (2002).

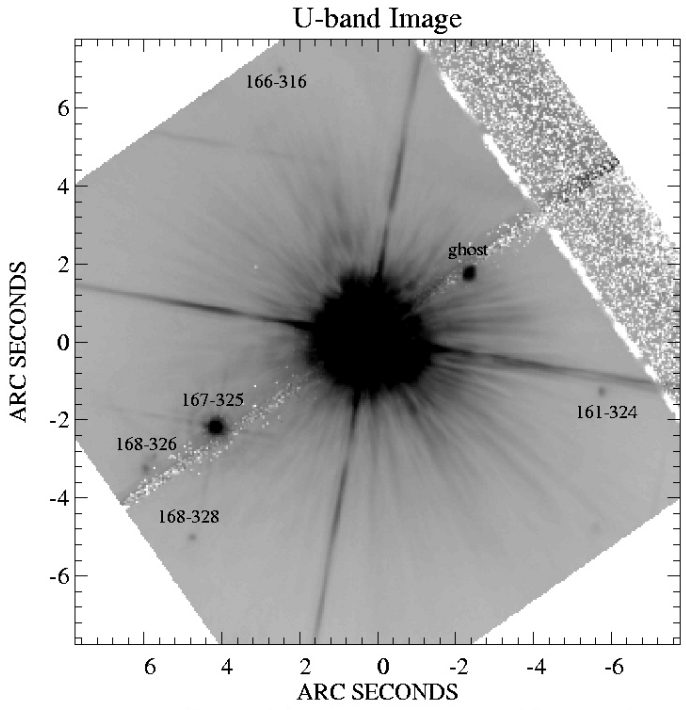

Figure 4.3: U-band image obtained with the PC portion of the WFPC2 and retrieved from the MAST. The field is centered on Θ^1 C Ori and covers the NACO field shown in Fig. 4.1 The ghost located at about 3″ N–W of Θ^1 C Ori is caused by internal reflections in the field flattener (see text for more details). The N-W edge of the chip is strongly affected by readout noise.

Orion 168-326 and Orion 168-328 are included in the catalogue of non-stellar objects by O'Dell and Wong (1996), while the remaining five sources are not classified. These seven sources are detected in the broad-band filters and in the long Brγ exposures with the exception of Orion 161-323, which is not detected in the J band. For the sources with detections in the J, H and Ks filters, we plot their colours in Fig. 4.2 (see also Sect. 2.5.3 for the interpretation of the Colour-Colour diagram). The objects Orion 168-328, 163-325 and 167-329 fall within the stripe of reddened main sequence stars, while the other four sources show NIR excess. Note that the binary proplyd system 168-326 has bluer J-H colour than typical dwarfs do. Orion 163-323 is the bluest objects among those in Fig. 4.2.

4.3.2 The U- and B-band archival HST images

The U- and B-band images are the only broad-band images obtained with the WFPC2 on board of HST. Θ^1 C Ori is badly saturated in the 30 s and 400 s exposures and its diffraction spikes lie at the position angles of some interesting sources like the binary proplyd Orion 168-326 and Orion 163-323. In Fig. 4.3, we present the short exposure (1 s) image obtained in the U filter with the Planetary Camera. The B image is very similar and is not shown here. The field is centered on Θ^1 C Ori and is slightly larger than the NACO field shown in Fig. 4.1: The proplyds Orion 166-316 and 161-324 are also detected in the NACO images but are at

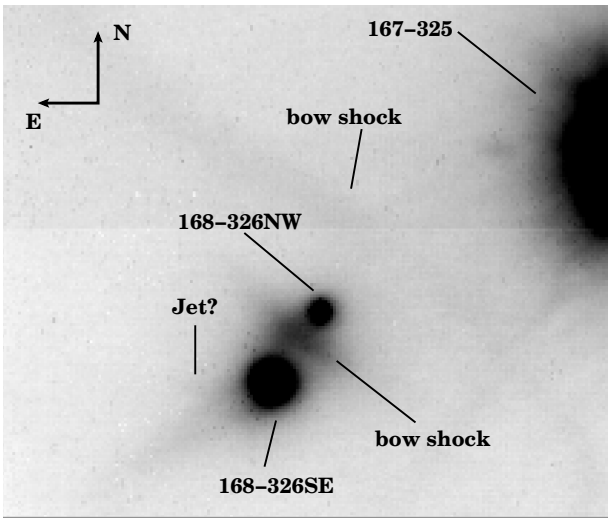

Figure 4.4: NACO Ks image of the binary proplyd 168-326. The negative gray scale shows clearly the two components 168-326NW and SE and the bow shock interaction between their photoevaporated flows. Also detectable are the bow shock due to the interaction between the proplyd flow and the wind from Θ^1 C Ori and the microjet, whose evidence is presented in García-Arredondo et al. (2001).

locations where the AO corrections cannot properly account for the atmospheric turbulence. Apart from the two stars Θ^1 C Ori and Θ^1 F Ori, only two other sources (in common with the NACO sources) are detected at these short wavelengths: These are the proplyds Orion 168-326 and 168-328. None of the five unclassified objects is detected in the U- and B-band images. A bright disk-like object appears to the N–W of Θ^1 C Ori at a projected distance of about $3''$. The shape and the location of the object strongly suggest that it is a ghost due to internal reflections in the field flattener (see Sect. 4.4.3 and 5.10 of the new WFPC2 Handbook v8.0). This is further supported by the fact that there is no evidence for such object in any of the other archival HST images nor in our NACO exposures.

4.4 Discussion of individual sources

In this section, we discuss in details the nature of the most interesting sources located within $6''$ from the massive star Θ^1 C Ori.

4.4.1 Four unclassified Orion sources: Proplyds or Stars?

The sources Orion 161-323, 162-319, 163-325 and 167-329 have been already detected by McCaughrean and Stauffer (1994) in the K' filter and by Muench et al. (2002) in the J, H and K filters. The red Orion 161-323 does not appear in our NACO J-band exposures, a lower limit value of 18 mag is estimated by Muench et al. (2002) from their deep NTT J-band image. A common characteristic to these sources is that they do not show any optical or infrared line emission: They are not detected in any of the narrow-band HST filters and do not appear in our long exposure continuum-subtracted Brγ image. This proves that they are surrounded by very little ionized gas.

We discuss here two possibilities that can explain the low ionization. The first one is that these sources are proplyds located at true distances from Θ^1 C Ori much larger than their projected distances, far enough to escape the ionizing radiation from the massive star. If this would be the case, we would expect infrared excess due to emission from the dust surrounding the pre-main sequence stars in the proplyds. This scenario might be appropriate for Orion 161-323 but not for the other three sources. In fact, the colours of Orion 162-319, 163-325, 167-329 are very close to reddened main sequence stars and show no or very little infrared excess (see Fig. 4.2). The alternative and more plausible explanation is that these sources have already lost their gas and dust envelopes and reached the zero-age main sequence.

4.4.2 The binary proplyd Orion 168-326

We resolve the two components of the binary proplyd Orion 168-326 in all our broad-band and long exposure narrow-band images. Going from shorter (J-band) to longer (Ks-band) wavelengths their sizes decrease but the SE component remains about 30 mas larger than the NW component at all wavelengths, see Fig. 4.4. In the subtracted Brγ images both components appear slightly more extended than in the broad-band Ks filter, as expected for externally ionized sources. The separation of their peak emission does not change with wavelengths, we measure a distance of $0\farcs4$ in all our NACO images. The interaction zone between the ionizing wind from Θ^1 C Ori and the flow from the proplyd disks is clearly visible in our Ks exposure with a shape similar to the Hα and [OIII] emission (Bally et al. 1998). In addition, we detect the interaction between the two proplyds as a bright and extended arc, concave in respect to the small NW component, in the H, Ks and in the continuum subtracted Brγ images (see Fig. 4.4). The U and B bands also resolve the two knots at the same location of the NACO images and the interaction zone above mentioned. Marginally detectable in the 2 μm exposures is the microjet from the SE component also present in the [OIII] line emission (García-Arredondo et al. 2001).
The proplyd-proplyd shock and proplyd-wind shock have been first discovered in the Hα and [OIII] HST images and later mapped in the 5 GHz radio continuum (Graham et al. 2002). A model that explains these features is that of two side-by-side proplyds whose photoevaporating winds collide and create a bow shock detected in emission lines and radio as a bright arc in between them (Graham et al. 2002).

4.4.3 Orion 163-323 and its bright mid-infrared counterpart

Orion 163-323 is the closest object to Θ^1 C Ori at only $2''$ projected distance. Among its peculiarities are the compactness of its Hα and [OIII] line emission and the very bright and compact MIR appearance (Hayward et al. 1994; Robberto et al. 2002). The 10 μm image of Orion 163-323 with the location of the sources identified in our NACO images is shown in Fig. 4.5. In the following, we will show that our new NIR high-resolution images provide additional relevant information to understand the nature of this source. We will analyze the spectral energy distribution of Orion 163-323 and for the first time its size as function of the wavelength.
We start by compiling the list of flux measurements at different wavelengths. Orion 163-323 is detected in all the long-exposure NACO images but not in the U- and B-band HST observations. The sensitivity in the U and B exposures at the location of Orion 163-323 is limited by the high and varying background close to Θ^1 C Ori. We estimate the limiting

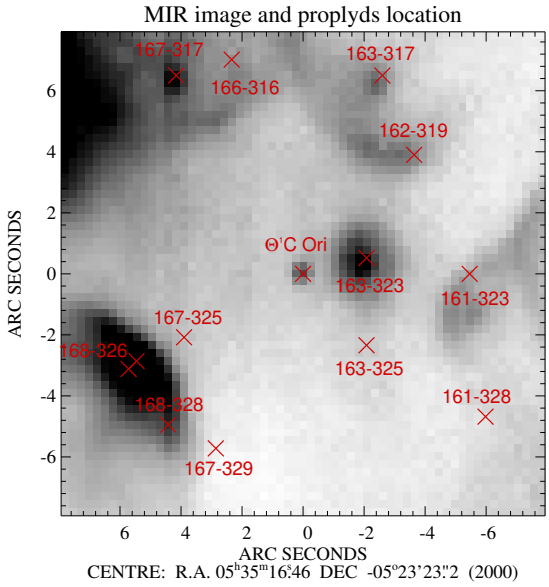

Figure 4.5: Greyscale 10 μm image of Θ^1 C Ori and its surroundings. The image has been acquired with the MAX camera on UKIRT and has a plate scale of $0\farcs26$ pixel^{-1} (Robberto et al. 2002). With red crosses we show the location of the NIR sources identified in our NACO images. Orion 163-323 appears bright and compact at 10 μm.

magnitudes in the following manner: First, we fit a gaussian to the proplyd Orion 168-328 that appear point-like in the U and B filters (see Fig. 4.3) and we compute its magnitude as described in Sect. 8.8 of the WFPC2 Handbook v8.0; Then we place the fitted gaussian at the location of Orion 163-323 and we scale its magnitude until the source disappears in the background. In this way, we estimated lower limit magnitudes of 14.7 mag and 16.9 mag in U and B filters respectively. In Table 4.1 we report on new J, H and Brγ flux measurements, the upper limits for the U and B bands and we summarize fluxes known from the literature. From our Brγ image, we estimate a line emission of 7.5×10^{-12} erg s^{-1} cm^{-2}, which is 12% of the total Ks flux. Fluxes in the Hα and [OIII] filters are taken from Bally et al. (1998): the source is not detected in the other HST narrow-band filters. We show the complete spectral energy distribution (SED) of Orion 163-323 in the left panel of Fig. 4.6. Its more prominent features are the large MIR flux density (more than 400 times that measured at 2 μm) and the steep flux increase towards the J-band, even steeper than that for the binary proplyd Orion 168-326 (note also the blue colours of Orion 163-323 in the diagram of Fig. 4.2).

To determine whether the NIR fluxes originate from the star photosphere, we fit the NIR measurements with a single black body and assume an extinction of A_V=1 mag and redding vector Rv=5.5 from Fitzpatrick (1999). The star temperatures and sizes are taken from Tokunaga (2000) for main-sequence stars and from Baraffe et al. (1998) for pre-main sequence stars. The extinction of only 1 mag in V should be a good estimate for the line-of-sight extinction for the following reasons: I) A_V=1 mag is measured towards the close Θ^1 C Ori; II) Since the radiation from Θ^1 C Ori reaches Orion 163-323 and ionizes the surrounding gas, the extinction between the two sources must be small; III) The MIR emission of Orion 163-323 is optically thin (Hayward et al. 1994), which also supports II). The result of black body

Table 4.1: Observed magnitudes and fluxes for Orion 163-323

Band	Brightness [mag]	Error [mag]	Ref.
U	> 14.7		1
B	> 16.9		1
J	12.09	0.12	1
H	12.79	0.16	1
Ks	12.48	0.12	1
K'	12.2	0.5	2
Band	Flux [erg s^{-1} cm^{-2}]	Error [%]	Ref.
Hα	2.4×10^{-13}	5–25	3
OIII	1.9×10^{-13}	5–25	3
Brγ	7.5×10^{-12}	30	1
Band μm	Flux density [Jy]	Error [Jy]	Ref.
8.8	3.93	0.79	4
10.0	4.0	0.8	5
11.7	4.13	0.82	4

- References (1) This thesis ; (2) McCaughrean and Stauffer (1994) ; (3) Bally et al. (1998) ; (4) Hayward et al. (1994) ; (5) Robberto et al. (2002)

fitting procedure is that the J-band flux is always larger than what expected from the star photosphere, that might be the result of dust scattering.

To further investigate this possibility we analyze the size of the emission from Orion 163-323 at different wavelengths. Deconvolved sizes are computed assuming gaussian profiles both for the source and for the PSF (right panel of Fig. 4.6). In the case of the NACO measurements we used the source Orion 163-325 as PSF reference. Since the NIR colours of Orion 163-325 are typical of reddened main-sequence stars (see Fig. 4.2) and it is not detected in any of the narrow-band filters, it is likely not a proplyd (see Sect. 4.4.1). The PSF of the Hα and [OIII] HST images is computed with the latest version of the Tiny Tim PSF simulator for the specific source location on the detector (Version 6.1a, http://www.stsci.edu/software/tinytim/tinytim.html). Errors on the deconvolved sizes are the propagated formal errors of the gaussian fit. Orion 163-323 is marginally resolved in the Ks filter but its size is larger in the Brγ filter and at shorter wavelengths. Its extension in the Brγ filter is similar to the size measured in the Hα filter.

From the inspection of the sizes of Orion 163-323 at different wavelengths and from the measured flux densities, we conclude that we probably *detected the star only in the Ks filter.* If this would be the case, a de-reddened K2 MS star or a 1 Myr old 0.18 $M_\odot$ pre-main sequence star could account for the measured H and Ks fluxes. However, we have to keep in mind that later spectral type stars might as well be possible if unresolved emission from dust in

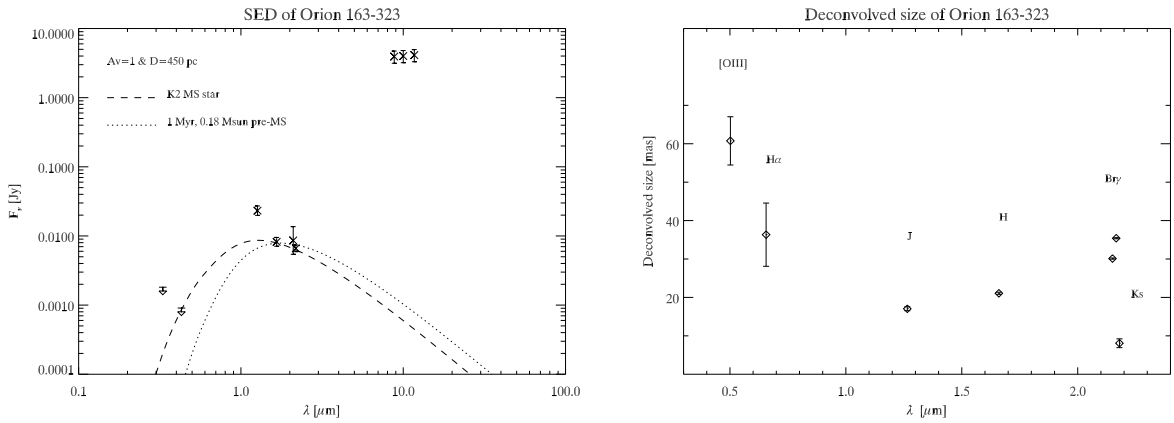

Figure 4.6: Properties of Orion 163-323. Left panel: Superimposed to the SED of Orion 163-323 are the black body emissions for two stars extincted by A_V=1 mag. Right panel: Deconvolved sizes of Orion 163-323 at different wavelengths. The corresponding filters are given above each symbol: J, H and Ks sizes are from the NACO data, sizes at shorter wavelengths are from the HST planetary camera images.

a circumstellar disk would contribute at 2 μm. The increase in flux and especially in size towards the H filter proves that *scattering from dust* start to contribute at this wavelenght and *becomes dominant in the J-band*: The measured J-band flux is at least 2.5 times larger than the flux density from the star photosphere. The dust might be located just behind the interaction zone between the wind from the disk and the wind from Θ^1 C Ori or alternatively scattered light from the circumstellar disk (see Fig. 4.7 for a schematic representation).
The rapid flux increase in the MIR regime is due to warm dust. The detection of the 9.7 μm silicate emission implies that the extinction is smaller than 1 at this wavelenght (Hayward et al. 1994). We can thus compute the total dust mass emitting in the MIR by assuming optically thin emission (see Sect. 2.5.1 for the formulae). The temperature of a black body grain at a projected distance of 2″ from Θ^1 C Ori would be around 200 K. We use temperatures between 100 and 300 K for the dust emission and dust opacities for the standard Mathis, Rumpl & Nordsieck-distribution for the diffuse interstellar medium (Ossenkopf and Henning 1994). The resulting dust masses can be as low as 4×10^{-9} $M_\odot$ or as large as 8×10^{-5} $M_\odot$, depending mainly on the assumed dust temperature. For comparison, we note that Lada et al. (1996) observed more than 10 proplyds in the mm regime and measured total disk masses between 0.007 and 0.016 $M_\odot$. Only our largest estimate of the dust mass towards Orion 163-323 falls in this range when the typical dust mass over gas mass ratio of 100 is assumed. As discussed in the case of the scattering, the dust might be located just behind the spherical ionization front (I-Front) or we might detect warm dust from the disk. Mid-infrared interferometric observations are needed to resolve and determine the dust in the disk.

4.5 Conclusions

We imaged the close vicinity of the massive star Θ^1 C Ori using the NACO adaptive optics system on the VLT. We detected at least three NIR sources within 10″ from Θ^1 C Ori that are likely to be low-mass main sequence stars based on their NIR colours and on the absence

of line emission. The binary proplyd Orion 168-326 is resolved into two bright knots both in our NIR and in the U- and B-band HST images. The fainter arc-like emission between the two components is prominent in the Brγ continuum-subtracted exposures and is due to the interaction between the photoevaporated winds from the proplyds. We also marginally detected the microjet from the SE component at 2 μm.
The NIR colours and the compact line emission from Orion 163-323 strongly support the idea that the source is a proplyd with the peculiarity of being seen almost face-on. Our high-resolution NIR images resolve Orion 163-323 in the J, H and narrow-band Brγ filters. The inspection of the sizes and flux densities at different wavelengths suggests that we probably detected the star in the proplyd in our Ks exposures. The J-band flux is much larger than what is expected from the stellar photosphere, which we explain by being dominated by dust scattering. The large MIR emission must be thermal emission from warm dust. Our data cannot decide if most of the dust emitting in the J- and N-bands is located in the disk or just behind the spherical ionization front. More reliable measurements of the extinction and high-resolution interferometric MIR observations could resolve and determine the amount of dust in the disk.
With a resolution as good as the Hubble Space Telescope in the optical, our new near-infrared images clearly show the impact of massive stars on their surroundings. Their winds and strong ultraviolet radiation strip away and ionize the outer material around nearby young low-mass stars. The efficiency of these destruction processes have strong implications on the evolution of the circumstellar disks (proplyds) and on the possibility whether such disks can form planets.

The NACO near-infrared images targeting Θ^1 C Ori and preliminary results were presented at the IAU Symposium no. 221 (Pascucci et al. 2003a).

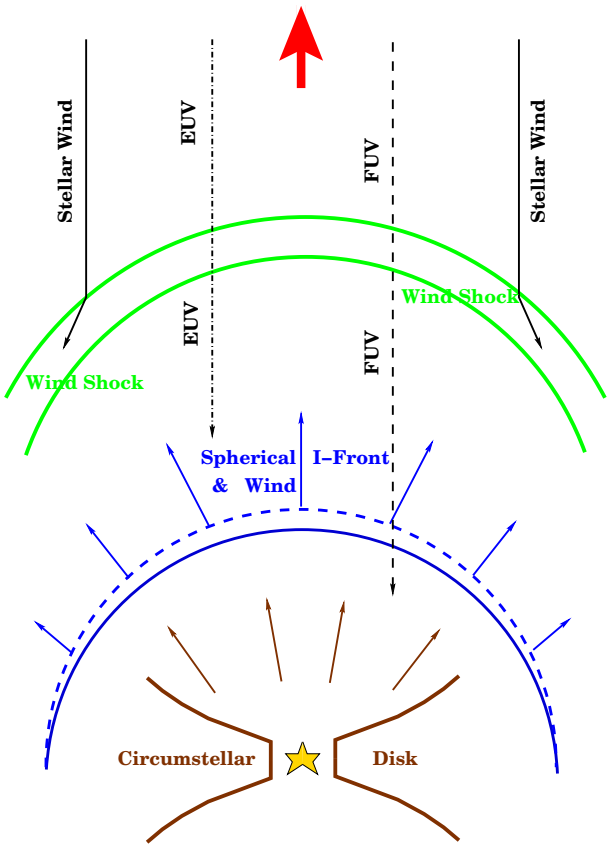

Figure 4.7: Schematic drawing of Orion 163-323. The big red arrow at the top of the figure shows the direction of Θ^1 C Ori and of the Earth. The young star is surrounded by a circumstellar disk which receives the FUV radiation (photons with energy $< 13.4\,\mathrm{eV}$) from Θ^1 C Ori and starts a slow wind of neutral atomic gas. The wind is accelerated when it passes through the local ionization front (I-Front) located where photons of energy larger than 13.4 eV are completely absorbed. A stationary bow shock is formed where the wind from the disk reaches ram pressure balance with the Θ^1 C Ori stellar wind.

Chapter 5

Towards Modeling Disks Around Massive Stars

If massive stars form as low-mass stars, circumstellar disks are a natural consequence of their formation process (Yorke and Sonnhalter 2002). However, their lifetime is limited to only a few 10^5 yr by photoevaporation due to the intense ultraviolet flux from the central star (e.g. Hollenbach et al. 2000). These short timescales partly explain why no direct evidence [1] of such disks has been found up to now. Observational limitations are the high resolution and sensitivity needed to penetrate the crowded dusty regions of massive star formation (see Chapter 2 and 3). These issues are now being tackled by new techniques such as interferometry and adaptive optics and by space facilities. The new instruments are expected to bring convincing evidence for the existence of disks around young massive stars and to constrain their properties. The complexity of these regions however will require substantial modeling effort and *reliable tools* to correctly interpret the observations.

Currently a number of continuum multidimensional radiative transfer (RT) codes exist and are widely used to predict and to interpret observations from various astrophysical objects (see e.g. Dunn et al. 2002; Wolf et al. 2003; Dullemond and Dominik 2004a; Gonçalves et al. 2004). However, such complex numerical codes can be independently tested only in the simplest cases where the RT equation can be solved analytically. These cases are certainly far from representing the complexity of dust-enshrouded objects and do not guarantee the robustness of the RT solutions in general.

In this Chapter, we present the first comparison of five different RT codes in a two-dimensional (2D) configuration aiming to provide *benchmark solutions for the verification of RT codes*. We consider the well-known case of a low-mass star surrounded by a circumstellar disk and we test the maximum disk mass that current RT codes are able to handle. This investigation represents an important step in understanding the actual limitations of RT codes and the improvements necessary to model disks around high-mass stars. In Sect. 5.6, we discuss an application of RT codes to interpret and to predict interferometric measurements.

[1] Indirect evidence is provided by the high detection rate of powerful molecular outflows toward young high-mass stars (for a review see Zhang 2002)

5.1 Establishing the benchmark for disk configurations

In contrast to hydrodynamical simulations, benchmark tests for radiative transfer computations are rare. The only practical approach to test the reliability of RT calculations is to compare solutions of well-defined problems by several independent codes. This has been done for the one-dimensional (1D) case by Ivezic et al. (1997). A benchmark project for 1D plane-parallel RT and vertical structure calculations for irradiated passive disks is available on the web [2]. As for 1D radiative transfer in molecular lines, a comparison of results from different codes has been performed by van Zadelhoff et al. (2002) [3]. Going from spherical symmetry to two- and three-dimensional spatial configurations, we add two or three more variables to the RT problem. Numerically, this implies 10^4 or 10^6 more numbers to store when a decent resolution of 100 points in each variable is used. In addition, the geometry makes the solution of the integro-differential RT equation more complex. This explains why *benchmark tests for 2D and 3D configurations are lacking.* It also implies that reaching an agreement to the level of 1D radiative transfer computations using state-of-the-art computer equipment is unrealistic. A previous attempt to test 2D radiative transfer calculations has been made by Men'shchikov and Henning (1997). They compare results from their approximate method with those of a fully-2D program (Efstathiou and Rowan-Robinson 1990) applying the same geometry.
Here, we test the behaviour of five different RT codes in a well defined 2D configuration, point out advantages and disadvantages of the various techniques applied to solve the RT problem and provide benchmark solutions for the verification of continuum RT codes. As modelling sources with high optical depth and strong scattering is the challenge of multi-dimensional RT codes, we explicitly include *a test case at the limit of the current computational capabilities.* In next two sections we briefly introduce the RT problem and we define our test case. From Sect. 5.3.1 to 5.3.3, we describe the different methods to solve the RT equation, the codes used in this benchmark and their reliability in 1D configurations. We present the details of these 2D simulations in Sect. 5.3.4 and solutions for the dust temperature and emerging SEDs from Sect. 5.4.1 to Sect. 5.4.4. In the last section we discuss our results.

5.2 Benchmark problems

5.2.1 The radiative transfer problem

Solving the RT problem means to determine the intensity $I_\lambda(\vec{x},\vec{n})$ of the radiation field at each point $\vec{x}$ and direction $\vec{n}$ of the model geometry and at each wavelength λ. This is achieved by solving the stationary transfer equation

$$\begin{aligned}\vec{n}\nabla_{\vec{x}} I_\lambda(\vec{x},\vec{n}) \;=\; & -\left[\kappa^{\rm abs}(\lambda,\vec{x}) \;+\kappa^{\rm sca}(\lambda,\vec{x})\right]\; I_\lambda(\vec{x},\vec{n}) \\ & +\kappa^{\rm abs}(\lambda,\vec{x})\; B_\lambda[T(\vec{x})] \\ & +\frac{\kappa^{\rm sca}(\lambda,\vec{x})}{4\pi}\int\limits_\Omega d\Omega' p(\lambda,\vec{n},\vec{n}') I_\lambda(\vec{x},\vec{n}') \\ & +E_\lambda(\vec{x},\vec{n}) \end{aligned} \tag{5.1}$$

[2] http://www.mpa-garching.mpg.de/PUBLICATIONS/DATA/radtrans/benchmarks/
[3] see also: http://www.strw.leidenuniv.nl/~radtrans/

where $\kappa^{\rm abs}(\lambda,\vec{x})$ and $\kappa^{\rm sca}(\lambda,\vec{x})$ are the absorption and scattering coefficients of the particles, respectively. The quantity $p(\lambda,\vec{n},\vec{n}')$ denotes the probability that radiation is scattered from the direction $\vec{n}'$ into $\vec{n}$, Ω is the solid angle, B_λ is the Planck function, and T is the temperature. The index λ denotes that the quantity is defined per wavelength interval. $E_\lambda(\vec{x},\vec{n})$ represents all internal radiation sources such as viscous heating or cosmic rays. For the sake of simplicity, we only consider one dust component of specific size and chemical composition. In addition, we do not discuss the polarization state of the radiation field and consider the intensity only.
If spherical symmetry in the particle distribution and the sources of radiation is assumed, the integro–differential equation (5.1) becomes a function of 3 variables, already difficult to solve even for a given dust temperature $T(\vec{x})$. In the case of spatial 2D configurations (axial-symmetric disks, tori), we have to deal with 5 variables. Moreover, the coupling between the radiation field and the dust temperature requires the simultaneous consideration of the balance equation for the local energy density at point $\vec{x}$

$$\int_0^\infty d\lambda\ Q_\lambda^{\rm abs} B_\lambda[T_{\rm rad}(\vec{x})] = \int_0^\infty d\lambda\ Q_\lambda^{\rm abs} \frac{1}{4\pi} \int_\Omega d\Omega'\ I_\lambda(\vec{x},\vec{n}') \tag{5.2}$$

to calculate intensity and temperature self–consistently. Here, $Q^{\rm abs}(\lambda)$ is the absorption efficiency factor, while $T_{\rm rad}$ is the temperature arising from radiative heating. Additional heating sources can contribute to the temperature with

$$T(\vec{x}) = T_{\rm rad}(\vec{x}) + T_{\rm heat}(\vec{x}). \tag{5.3}$$

5.2.2 Model definition

We consider the general astrophysical case of a star embedded in a circumstellar disk with an inner cavity free of dust. We assume that the star is point-like, located at the center of the configuration and radiating as a black body at the same temperature as the Sun. The disk is made of spherical astronomical silicate grains, having a radius of 0.12 μm and a density of 3.6 $\mathrm{g\,cm^{-3}}$ (optical data are taken from Draine and Lee 1984 [4], see also Fig. 5.1). The disk radially extends to a maximum distance of 1000 AU from the central star. Since the correct determination of the sublimation radius is quite a difficult problem, we fix the inner radius to 1 AU. This guarantees a maximum dust temperature less than 1000 K, even in the case of high optical depth. The density structure is that of a massless (in relation to the central star) Keplerian disk having no cutoff at a certain opening angle. This implies that *the radiative transfer has to be simulated both in the optically thick disk and in the optically thin envelope*. The disk geometry and density structure are similar to those described by Chiang and Goldreich (1997, 1999) and successfully applied to study passive disks around T Tauri stars (Natta et al. 2000). The density distribution provides a steep-density gradient in the inner part of the disk which could give rise to numerical problems when solving the RT equation. This turns out to be an advantage for RT comparison since it allows to test the codes' behaviour under extreme conditions. The density distribution we adopt has the following form

$$\rho(r,z) \quad = \quad \rho_0 \times f_1(r) \times f_2(z/h(r)) \tag{5.4}$$

[4] downloadable from: http://www.mpia.de/PSF/PSFpages/RT/benchmark.html

Table 5.1: Model parameters

Symbol	meaning	value
M_*	Stellar mass	1 $M_\odot$
R_*	Stellar radius	1 $R_\odot$
T_*	Stellar effective temperature	5800 K
$R_{\rm out}$	Outer disk radius	1000 AU
$R_{\rm in}$	Inner disk radius	1 AU
$z_{\rm d}$	Disk height	125 AU
a	Grain radius	0.12 μm
$\rho_{\rm g}$	Grain density	3.6 g cm^{-3}
$\tau_{\rm v}$	Optical depth at 550 nm	0.1, 1, 10, 100

$$\begin{aligned} f_1(r) &= (r/r_{\rm d})^{-1.0} \\ f_2(r) &= exp(-\pi/4 \times (z/h(r))^2) \\ h(r) &= z_{\rm d} \times (r/r_{\rm d})^{1.125} \end{aligned}$$

with r being the distance from the central star in the disk midplane ($\sqrt{x^2+y^2}$) and z the distance from the midplane. Here $r_{\rm d}$ is half of the disk outer radius ($R_{\rm out}/2$) and $z_{\rm d}$ one fourth of $r_{\rm d}$ ($R_{\rm out}/8$). Note that the disk is slightly flared, i.e., the disk opening angle $h(r)/r$ is exponentially increasing with the distance from the star. The term f_1 provides the radial dependence of the density distribution. In protoplanetary disks, the volume density is usually proportional to $r^{-\alpha}$ with α in the range (1.8÷2.8) (e.g. Wood et al. 2002 and Cotera et al. 2001). For this benchmark we use $\alpha = 1$ in order to save CPU time. Both f_1 and f_2 remain unchanged while ρ_0 is chosen so to define different optical depths. We perform calculations for four values of visual (λ = 550 nm) optical depth, namely $\tau_{\rm v}$ = 0.1, 1, 10, 100. The optical depth, as seen from the centre, is calculated along the disk midplane. Since most of the dust is confined in the midplane, the optical depths we refer to are the highest in each model. The test case $\tau_{\rm v}$ = 100 is at the limit of our current computational capabilities. The resulting total dust mass for the model with $\tau_{\rm v}$ = 1(100) is 1.1×10^{-6} $M_\odot$(1.1×10^{-4} $M_\odot$). The density structure perpendicular to the disk midplane is shown for the same model in Fig. 5.2. The RT is calculated for 61 wavelengths being distributed nearly equidistantly on a logarithmic scale from 0.12–2000 μm. These 61 wavelengths define the frequency resolution of our computations. In Sect. 5.4.4 we also compare two Monte Carlo (MC) codes on a grid with two times more wavelengths and we discuss the effect of the frequency resolution on the 2D benchmark. Since anisotropic scattering is not included in all codes, we consider the scattering as isotropic. Symbols and values of the model parameters are summarized in Table 5.1 for more clarity.

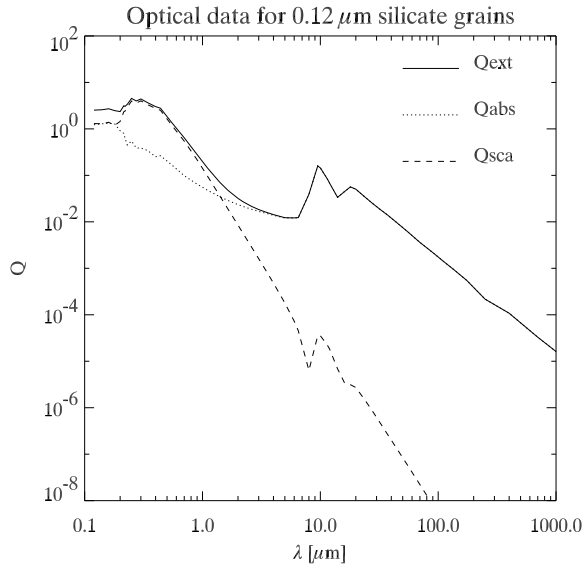

Figure 5.1: Optical data for spherical astronomical silicate grains having a radius of 0.12 μm (Draine and Lee 1984). Note that scattering dominates between 0.2 and 1 μm for this type of grains.

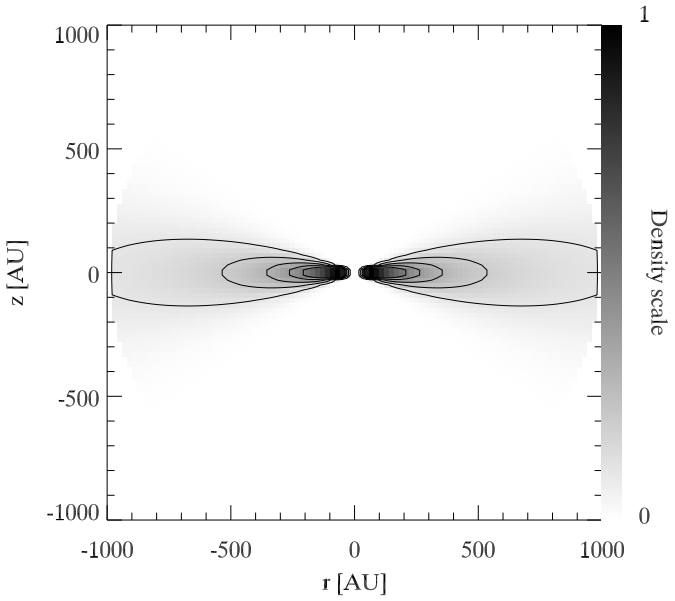

Figure 5.2: Density structure perpendicular to the disk midplane and centered on the star for the model with $\tau_{\rm v} = 1$. Values are normalized to the maximum density. The contours provide 0.10, 0.19, 0.28, 0.38, 0.48% of the maximum.

5.3 Radiative transfer simulations

5.3.1 Methods to solve the radiative transfer equation

Similar to hydrodynamical simulations, we can distinguish particle (Monte Carlo) and grid-based methods to solve the RT equation numerically (Henning 2001).
In MC simulations the radiation field is partitioned in equal-energy, monochromatic "photon packets" that are emitted stochastically both by the source and by the surrounding envelope. The optical depth determines the location at which the packets interact while their albedo defines the probability of either scattering or absorption. In the original scheme (*scheme 1*) the source and the envelope photon packets are emitted separately. At first the grains re-emit according to the absorbed source radiation. Then dust reemission takes also into account the envelope emission radiation field. Reemission by the dust is repeated as long as the difference between the input and the output energy is larger than a chosen threshold. However, the dust reemission, i.e. the repetition of the Monte Carlo experiment, is time consuming. An alternative possibility (*scheme 2*) is to store all radiation exchanges within the envelope. In this case the Monte Carlo experiment can be carried out once for all[5], but a large amount of computer memory is needed. A drawback of these two schemes is that the input luminosity is not automatically conserved during the simulation. This becomes a serious problem for configurations with very high optical depths which therefore usually need a larger number of iterations. A solution has been found by Bjorkman and Wood (2001) in the so-called immediate reemission (*scheme 3*). In this case only source photon packets are emitted and followed in their interaction locations. When a packet is absorbed, its energy is added to the envelope and a new packet is emitted immediately at a frequency which takes into account the modified envelope temperature. This method does not require any iteration and implicitly conserves the total energy. Another improvement of the standard MC procedure has been proposed by Lucy (1999) to treat extremely optically thin configurations. This approach considers the absorption not only at the end points of the photon path but also in between.
Grid-based codes solve the RT equation on a discrete spatial grid. The grid can be either determined during the simulation or generated before starting the computation. The 2 RT grid-based codes we compare, namely RADICAL and STEINRAY, use the second approach (see following code description in Sect. 5.3.2). Among the schemes applied to solve the RT problem two are the most used: the so-called "Lambda Iteration" (see e.g. Collison and Fix 1991; Efstathiou and Rowan-Robinson 1991) and the "Variable Eddington Tensor" (Mihalas and Weibel Mihalas 1984; Malbet and Bertout 1991; Stone et al. 1992; Kikuchi et al. 2002; Dullemond et al. 2002; Dullemond and Dominik 2004b). The "Lambda Iteration" mode suffers from the same convergence problems as the standard MC which is based on *scheme 1*. Thus, the improved "Accelerated Lambda Iteration" (e.g. Rybicki and Hummer 1991) method is more widely applied. The "Variable Eddington Tensor" mode is more robust than the "Lambda Iteration" and usually converges faster. Moreover, it has been proven that it works properly even at extremely high optical depths. Integration of the formal RT equation can be done in a straightforward way by applying the "Long Characteristics" algorithm. This method is accurate but turns out to be costly in CPU time. A more efficient way is based on the "Short Characteristics" algorithm (Mihalas et al. 1978; Kunasz and Auer 1988).
Each of the solution algorithms has its advantages and drawbacks. In MC methods, a photon is propagated through the calculation domain and its scattering, absorption, and re-emission

[5] This is only valid for opacities explicitely independent on the temperature

Table 5.2: Main features of the codes.

Feature	MC3D	MCTRANSF	RADICAL	RADMC	STEINRAY
3D	+				+
anisotropic scattering	+	+		+	+
arbitrary grid geometry	+	+			
grain size distribution	+	+	+	+	+
multiple dust species	+		+	+	+
images	+	+	+	+	+
polarization maps	+				
global error control			+		+
multiple/extended heating sources	+		+		+
dust evaporation		+	+		
acceleration for high τ	+	+	+		+
parallel version		+	+		

are tracked in detail. This allows to treat very complicated spatial distributions, arbitrary scattering functions and polarization. Drawback is the presence of a random noise in the results. This noise can be reduced by increasing the number of used photon packages and by including deterministic elements in the MC experiment (Niccolini et al. 2003). Grid-based solvers are less flexible than MC codes but have the advantage not to involve random noise.

5.3.2 Description of the codes

In the following sections we briefly describe the RT codes participating in the 2D benchmark. A summary of their main features is provided in Table 5.2.

MC3D

MC3D is a 3D continuum RT code. It is based on the MC method and solves the RT problem self-consistently. MC3D is designed for the simulation of dust temperatures in arbitrary dust/electron configurations and the resulting observables: spectral energy distributions, wavelength-dependent images and polarization maps.
For the estimation of temperatures either the standard *scheme 1* (see Wolf et al. 1999; Wolf and Henning 2000) or the immediate reemission concept (*scheme 3*) can be applied. For this benchmark project, the *scheme 3* is used to treat properly the more optically thick models. Optically very thin configurations, such as the atmosphere/envelope described in Sect. 5.2.2, are easily computed by the method proposed by Lucy (1999). Furthermore, the efficiency of MC3D is increased by (a) the fast photon transfer and (b) wavelength range selection concept (see Wolf and Henning 2000), and (c) the enforced scattering mechanism as described by Cashwell and Everett (1959).

Previous applications of MC3D cover feasibility studies of extrasolar planet detections (Wolf et al. 2002a), the RT in the clumpy circumstellar environment of young stellar objects (Wolf et al. 1998), polarization studies of T Tauri stars (Wolf et al. 2001), AGN polarization models (Wolf and Henning 1999), a solution for the multiple scattering of polarized radiation by non-spherical grains (Wolf et al. 2002b), and the inverse RT based on the MC method (Wolf 2001). Executables of MC3D (V2) can be downloaded for several model geometries and platforms from: http://www.mpia-hd.mpg.de/FRINGE/SOFTWARE/mc3d/.

MCTRANSF

MCTRANSF solves multi-dimensional continuum RT problems in dusty media by means of a MC method. It has been originally developed by Lopez et al. (1995). So far, the code has been used for the empirical modelling of several circumstellar envelopes of post AGB-stars of different types (e.g. Lopez and Perrin 2000), including multi-scattering effects.
Currently, only spherical symmetric (1D) and axisymmetric (2D) problems can be considered, but an extension to 3D is possible and straightforward. Several improvements of the standard MC procedure have been recently included (Niccolini et al. 2003) in order to avoid the usual increase of the noise level which typically occurs in extremely optically thin or optically thick situations. The concept suggested by Lucy (1999) is implemented to treat very optically thin cases. Optically thick configurations are tackled by the inclusion of several deterministic elements for the treatment of the absorption during the photon propagation phase, forcing the absorption to take place all along the rays. The temperature structure of the medium in radiative equilibrium is found by applying *scheme 2*. The convergence is found to be rapid, even in optically thick situations, but needs a large amount of computer memory, because the primary MC information must be stored source-dependently.
As a result of the combination of all these measures, MCTRANSF is capable to simultaneously model optically thin and optically thick parts of the model volume with about the same accuracy. Thus, both clumpy media and discontinuous opacity structures can be handled. MCTRANSF is able to arrive at numerical solutions for RT problems even in case of very large optical depths (e.g. for disk configurations). Parallelised versions of the code have been developed for a Cray T3E 1200 and for systems supporting the OpenMP application program interface. All these versions use shared memory systems.

RADICAL

The core of the code `RADICAL` is a lambda operator subroutine based on the method of "Short Characteristics", implemented on a polar grid by Dullemond and Turolla (2000). Using this subroutine as the main driver, `RADICAL` offers two modes of operation: a simple Lambda Iteration mode and a Variable Eddington Tensor mode. In this paper we use the latter because of its faster convergence and capability of treating high optical depths. The Variable Eddington Tensor method is implemented in RADICAL as follows (Dullemond and Dominik 2004b). First, the primary stellar radiation field is propagated from the star outwards into the disk. Dust scattering is included in a MC fashion. The energy absorbed by the disk in each grid-cell is then re-emitted as infrared (IR) radiation, which is treated as a separate radiation field. The 2-D transfer solution for this secondary radiation field is found by solving the frequency-integrated moment equations. The closure for these equations is based on the variable Eddington tensors and mean opacities computed with the Short Characteristics method

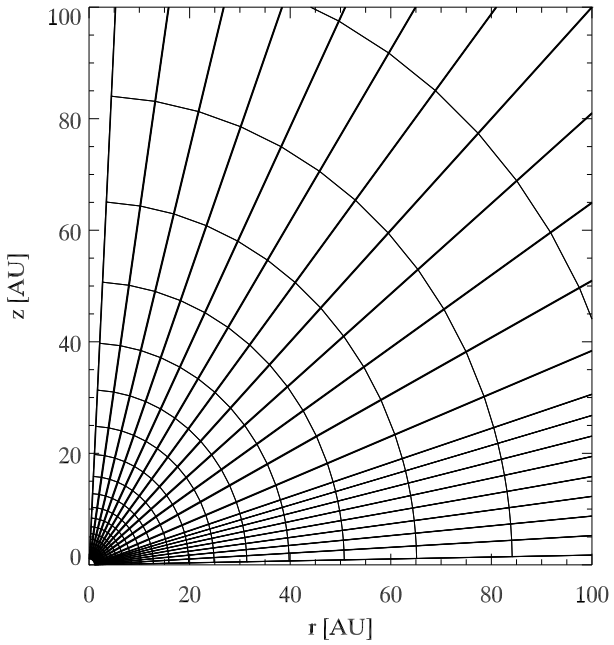

Figure 5.3: Grid adopted by MCTRANSF to store the temperature resulting from the RT simulations. Similar spherical grids are also used by the other codes.

of Dullemond & Turolla. At the end of the calculation a global check on flux conservation is made. For all the models discussed in this paper the error remained within 2%.

RADMC

RADMC is an MC code based on *scheme 3*. However, the original method of Bjorkman & Wood produces very noisy temperature profiles in regions of low optical depth, and requires a large number of photons ($N \sim 10^7$) for a smooth SED. These disadvantages have been solved in RADMC by treating absorption partly as a continuous process (Lucy 1999), and using the resulting smooth temperature profiles with a ray-tracing code to produce images and SEDs. These images and SEDs have a low noise level even for relatively few photon packages ($N \sim 10^5$). In addition, the frequency grid used for RADMC is not bound by the constraints set in the original method. This improved Bjorkman & Wood method works well at all optical depths, but may become slow in cases where the optical depth is very large ($\tau_{\rm v}$ about 1000). For the test cases in this paper the optical depths are low enough that this problem does not play a role. For more information on the code, see:
http://www.mpa-garching.mpg.de/PUBLICATIONS/DATA/radtrans/radmc/.

STEINRAY

STEINRAY is a grid-based code which solves the full 3D continuum RT problem. A combination of ray-tracing and finite differencing of 2nd order on adaptive multi-frequency photon transport grids is applied. Steinacker et al. (2002b) have shown that the use of 3rd order

Table 5.3: Resolution and number of photons for the different test cases.

Code Name	# r	Δ r [AU]	# θ	Δ θ [°]	# Phot [$\times 10^6$]	Test case $\tau_{550\mathrm{nm}}$
MC3D	55	0.03–141	121	1.5	244	0.1,1,10
MC3D	10^3	0.07–4.1	121	1.5	244	100
MCTRANSF	48	0.17–125	40	4.5	1000	0.1
MCTRANSF	48	0.17–125	40	4.5	800	1
MCTRANSF	46	0.18–130	46	2.8-5.3	1000	10
MCTRANSF	46	0.18–130	46	2.8-5.3	500	100
RADICAL	60	0.03–116	62	1.6-8.3		0.1–100
RADMC	60	0.03–116	62	1.6-8.3	10	0.1–100
STEINRAY	61	0.12–109	61	1.3		0.1–100

finite differencing is too time-consuming for 3D RT, while 1st order schemes introduce an unacceptable degree of numerical diffusion to the solution.
The spatial grids are generated using an algorithm described in Steinacker et al. (2002a). They are adaptive and optimized to minimize the 1st order discretization error hence guaranteeing global error control for solutions of radiative transfer problems on the grid. Since the use of one single grid for all frequencies leads to large discretization errors, STEINRAY calculates individual grids for each frequency to use the global error control of the grid generation method. Minimization of the grid point number is possible in regions where the optical depth becomes large allowing for treatment of applications with optical depth of any value. Contrary to former treatments, the full frequency-dependent problem is solved without any flux approximation and for arbitrary scattering properties of the dust. For the direction discretization, equally spaced nodes on the unit sphere are used along with corresponding weights for the integration derived by evaluating special Gegenbauer polynomials in Steinacker et al. (1996). The temperature distribution is calculated by an Accelerated Lambda Iteration between the radiative transfer equation and the local balance equation. The program is designed to provide spatially resolved images and spectra of complex 3D dust distributions and allows for multiple internal and external sources (Steinacker et al. 2003).
Recently, a 2D version of the program has been developed and was used for this benchmark. The grids are similar to the spherical grids shown in Fig. 5.3. The 2D version uses ray-tracing to solve for the intensity in all directions.

5.3.3 Reliability of the codes in 1D geometry

All the RT codes participating in the benchmark have been already tested in 1D spherically symmetric configurations. Results from MC3D have been compared with those calculated with the RT code of Chini et al. (1986) and with the code of Men'shchikov and Henning (1997). In both cases differences below 1% even in the case of high optical depth have been found (Wolf et al. 1999). MCTRANSF has been tested (Niccolini et al. 2003) against the 1D code written by Thibaut le Bertre and based on the work of Leung (1976). For the case of optical depth equal to 10 at 1 μm (with $\kappa \propto \frac{1}{\lambda}$, and isotropic scattering) the agreement between

MCTRANSF and le Bertre's code is better than 1%. In the case of RADICAL, tests have been performed by comparing the results with those from TRANSPHERE[6], a 1-D variable eddington factor code tested against the similar "code 1" of Ivezic et al. (1997). Steinacker et al. (2003) used the 1D benchmark provided by Ivezic et al. (1997) to test the 3D version of STEINRAY. Agreement below 1% has been found both for the emerging temperature and SEDs.

5.3.4 Details on the 2D radiative transfer computations

The three MC codes involved in the 2D benchmark, namely MC3D MCTRANSF and RADMC, choose a spherical grid to store the temperature resulting from the RT simulations. Radially the steps are logarithmic in order to properly resolve the innermost dense region of the disk. The number of radial points is kept below 100 for all the codes but MC3D, for which we tried a two weeks long computation for the most optically thick case (see Table 5.3). Differences in the SED between this computation and the one with 55 radial points and lower number of photons are discussed in Sect. 5.4.4. MC3D adopts an equally spaced grid in vertical direction (1.5° resolution, see Table 5.3), while MCTRANSF and RADMC choose a resolution decreasing with the distance from the disk midplane (see Fig. 5.3). Similar grid geometries are also used by the two grid-based codes RADICAL and STEINRAY. RADICAL makes use of the same grid as RADMC while STEINRAY has comparable resolution in vertical direction but larger cells in the inner disk (0.12 AU, see Table 5.3).
We note that *the resolution given in Table 5.3, together with the number of photons for the MC codes, are at the limit of the computing capabilities for most of the codes.* MC3D needs about 1 Gby memory. The temperature resulting from these test cases is obtained in 1–2 days. Computing the SED requires about a week for all the models, but for the most optically thick one for which we try a longer computation. MCTRANSF needs a large amount of computer memory to store all radiation exchanges. The necessary memory goes as the square of the number of cells: 46×46 cells is actually the technical limit ($\sim$ 4Gby) on our 4-processors (ev67 at 1 GHz) HP-compaq ES45 server. The runtime for the most optically thick case is about 2 weeks. Results from RADICAL and RADMC are obtained in less than a day for all the test cases. However, the actual spatial resolution of RADICAL cannot be doubled due to not sufficient computer memory. To produce the final spectrum RADMC uses the ray-tracing module from RADICAL, and for that reason is also limited to the maximum spatial resolution that can be achieved by RADICAL. This is a mere technical problem. In the 2D version of STEINRAY, the code uses about 1 Gby memory. To obtain convergence in the temperature iteration of 1% for the case $\tau_{\rm v} = 100$, the code runtime is about a week.

5.4 Results of the simulations

5.4.1 Approximate solution for optically thin configurations

In the case of configurations being optically thin for all relevant wavelengths, heating of the dust particles is dominated by the stellar radiation. When re-emission of the dust particles can be neglected and scattering is only included as extinction term, the dust temperature can be easily determined from equation (5.2) without any coupling to equation (5.1). We use this approximate semi-analytical solution to test independently our RT computations for the

[6] http://www.mpa-garching.mpg.de/PUBLICATIONS/DATA/radtrans/

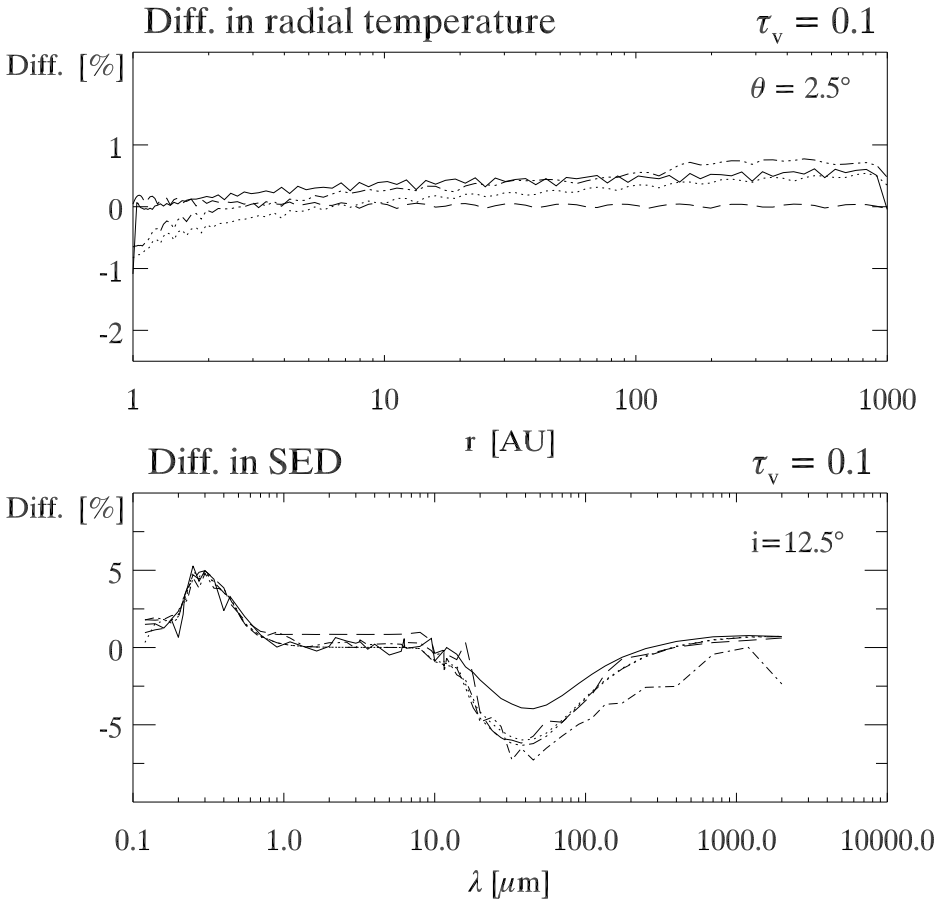

Figure 5.4: Differences of the most optically thin model from the semi-analytical solution (see Sect. 5.4.1). Upper panel: differences in radial temperature for an angle θ near to the disk midplane. Lower panel: differences in the SED for an almost face-on disk (disk inclination equal to 12.5°). For both panels, solid lines give the difference of MC3D, dot-dashed lines of MCTRANSF, dashed-dot-dot-dot of RADICAL, dotted lines of RADMC, and dashed lines of STEINRAY from the semi-analytical solution.

most optically thin case and to check the correctness of the density setup in the other more optically thick models (see Sect. 5.4.2 and 5.4.3).
The assumptions we discussed above simplify equation (5.2) in the following way

$$\int_{\lambda_{\min}}^{\lambda_{\max}} d\lambda\ B_\lambda[T_{\rm d}(R,\theta)]Q_\lambda^{\rm abs} = \left(\frac{R_*}{2R}\right)^2 \int_{\lambda_{\min}}^{\lambda_{\max}} d\lambda\ B_\lambda^e(T_*,R,\theta)Q_\lambda^{\rm abs} \tag{5.5}$$

with $T_{\rm d}(R,\theta)$ being the disk temperature at the location (R,θ)[7] and $Q^{\rm abs}(\lambda)$ the absorption efficiency factor. We perform the integration at the same wavelengths as those adopted by the RT codes (see Sect. 5.2.2). The term $B_\lambda^e(T_*,R,\theta)$ represents the black body emission from the star corrected for the extinction

$$B_\lambda^e(T_*,R,\theta) = B_\lambda(T_*)\, e^{-\pi a^2 (Q_\lambda^{\rm abs}+Q_\lambda^{\rm sca}) \int_0^{\rm R} dR' \rho(R',\theta)} \tag{5.6}$$

where a is the dust radius, $Q^{\rm sca}(\lambda)$ is the scattering efficiency factor and $\rho(R',\theta)$ is the density distribution given in equation (5.4) but here expressed in spherical coordinates. The argument of the exponent represents the optical depth $\tau_\lambda(R,\theta)$ at the distance R, θ from the central star. Once the optical depth is determined, the extincted black body emission can be substituted in equation 5.5 and the dust temperature can be easily computed. To obtain the flux density F_λ at a distance equal to the stellar radius we need to integrate the power emitted by each grain over the entire volume. If we express the power emitted by one grain as

$$P_\lambda^{\rm g}(R,\theta) = 4\pi a^2\, Q_\lambda^{\rm abs} B_\lambda[T_{\rm d}(R,\theta)] \tag{5.7}$$

the flux density can be obtained by solving the following integrals

$$F_\lambda = \frac{2\pi}{4\pi R_*^2} \int_{\rm R_{in}}^{\rm R_{out}} \int_{\theta=0}^{\pi} d\theta' dR' P_\lambda^{\rm g}(R',\theta')\, \rho(R',\theta')\, R'^2 cos(\theta') \tag{5.8}$$

here the factor 2π comes from the integration in ϕ which is the azimuthal angle in the $x-y$ plane.
A first rough estimate of the correctness of this approach can be done by evaluating how much the disk temperature $T_{\rm d}$ would increase because of secondary emission re-absorption events. The grain emissivity is proportional to $T_{\rm d}^4$ and, in case of optically thin emission, to the optical depth. Our most optically thin model has a maximum IR optical depth of 0.01 at 10 μm in the disk midplane, where most of the dust is confined. If an emitted IR photon were re-absorbed by the disk, its temperature would increase by the quantity $(1+\tau_{\rm IR})^{0.25}$. Thus, the temperature obtained by the semi-analytical approach can be considered correct within 0.26% in a first approximation. The corresponding emergent flux has an uncertainty which is about four times larger (about 1%). However looking at the SED differences (see Fig. 5.4), it is clear that deviations due to scattering (treated correctly in the numerical codes) are important too. A more realistic estimate of the error on the semi-analytical approach should indeed consider the effect of scattering apart from damping the stellar flux.

5.4.2 Resulting temperatures

All the codes correctly reproduce the shape of the temperature distribution, both its radial and vertical dependence.

[7] R and θ are the distance from the star and the angle from the disk midplane in spherical coordinates

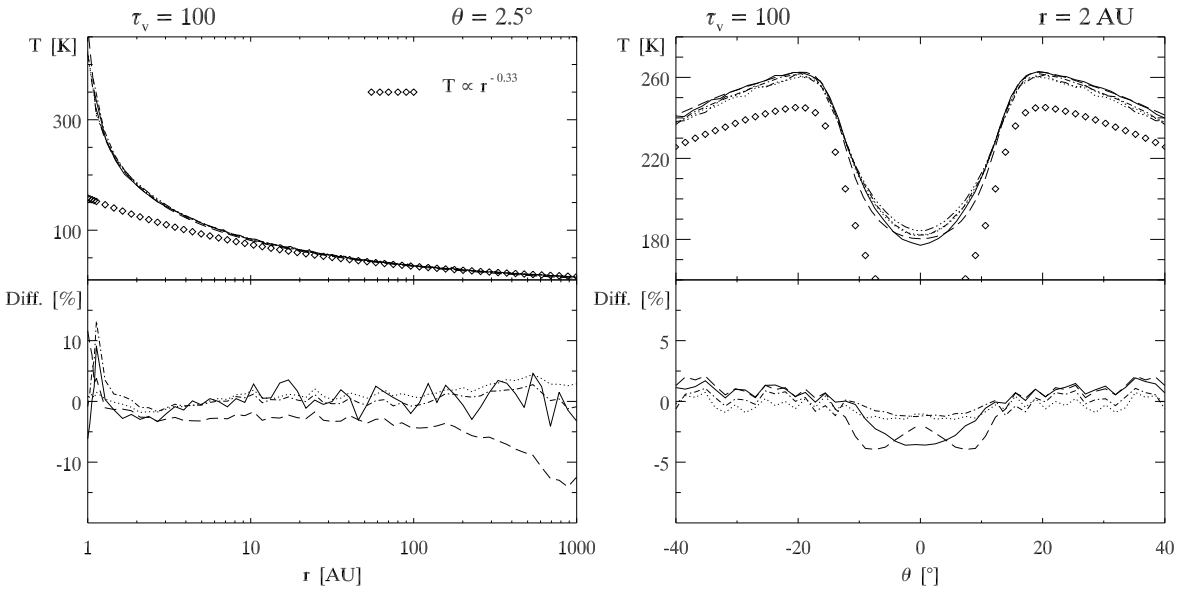

Figure 5.5: Comparison of the temperature distribution for the most optically thick model. Left: Radial temperature (upper panel) and percentage of difference among the codes (lower panel). RADICAL is taken as reference code. The radial cut is made for an angle θ near to the disk midplane. Diamonds give the radial dependence in case of long wavelengths and optically thin emission. In the upper panel, solid lines are the results from MC3D, dot-dashed lines from MCTRANSF, dashed-dot-dot-dot from RADICAL, dotted lines from RADMC and dashed lines from STEINRAY. In the lower panel, solid lines give the difference of MC3D, dot-dashed lines of MCTRANSF, dotted lines of RADMC and dashed lines of STEINRAY from RADICAL. Right: Vertical temperature (upper panel) and percentage of difference among the codes (lower panel). Cuts are made for a distance r in the midplane equal to 2 AU from the central star. The nomenclature is the same as for the left panels except for the diamonds which give the temperature behaviour following the semi-analytical approach described in Sect. 5.4.1. Note that all the RT codes have the same turnover in the temperature distribution at the location predicted by the semi-analytical solution.

In oder to test independently the most optically thin case (highest optical depth in the disk midplane of $\tau_{\rm v} = 0.1$), we use the semi-analytical solution derived in Sect. 5.4.1. The upper panel of Fig. 5.4 shows the percentage of difference[8] between the semi-analytical solution and any other code. Radial cuts are plotted for an angle θ near to the disk midplane where the influence of scattering is the largest. The differences between the semi-analytical solution and the RT codes is always smaller than 1%.
Temperature distributions for the models with $\tau_{\rm v}$ =1 and 10 agree better than 10% for all the cases we examine. The disk model with the highest optical depth is the most difficult to treat for the RT codes. In Fig. 5.5, we show radial and vertical cuts at the disk locations where deviations from the codes are expected to be higher, i.e. near to the disk midplane and close to the central star. The radial temperature is plotted for an angle θ equal to 2.5° from the disk midplane while the vertical temperature is given for a distance equal to 2 AU from the central star. In the upper panel of Fig. 5.5, we also superimpose the temperature dependence for the optically thin regime at long wavelengths. In this regime the temperature distribution depends only on the dust properties and can be approximated by $T(r) \propto r^{-2/(4+\beta)}$ (Evans 1994). Here β corresponds to the index of the dust absorption coefficient at low frequencies ($\kappa_\nu^{abs} \propto \nu^\beta$). For Draine & Lee silicates β is equal to 2, leading to an exponent of -0.33 in the temperature relation.
The upper panel of Fig. 5.5 provides (in diamonds) the vertical temperature profile from the semi-analytical approach described in Sect. 5.4.1. The semi-analytical solution has the turnover point from optically thick to optically thin (the place where the temperature suddenly starts to drop) around 19° from the midplane. Since the solution provided by the RT codes should have the same behaviour, we used the semi-analytical approximation to check the correctness of the density setup. The disk midplane calculated with the semi-analytical approach is naturally cooler than the real disk because the approximation neglects heating of the disk from dust re-emission. The outer regions of the real disks are also warmer because of those photons scattered far from the midplane. At a distance r of 2 AU from the star and exactly in the midplane the real temperature is a factor of about 1.3 higher than that given by the semi-analytical solution.
The lower panels of Fig. 5.5 provide the percentage of difference among the codes taking RADICAL as reference code. The radial temperatures agree better than 5% in most of the disk, going from 1.2 AU to 200 AU. Around 1.1 AU MCTRANSF deviates slightly more than 10%. STEINRAY shows 10% deviations at the inner boundary and slightly higher deviations (but always less than 15%) far from the star, at about 900 AU. The vertical cut at 2 AU shows an agreement better than 2.5% till 10° from the disk midplane. Closer to the disk midplane, deviations are larger for MC3D and STEINRAY but always smaller than 4%.

5.4.3 Emerging spectral energy distributions

The emerging spectra for the four models having different optical depths are shown in Fig. 5.6 at two disk inclinations. The left panel provides the results for an almost face-on disk (disk inclination i equal to 12.5°) while the right panel gives the result for an almost edge-on disk (i = 77.5°). Each curve represents the mean value of the five RT simulations for the specific model, whose optical depth is given in parenthesis above the curve. On the y axis, we plot λF_λ in [W m^{-2}] where F_λ is the flux density at a distance equal to the star radius.

[8] with difference we mean: $\frac{(a-b)}{b}$. Here b stands for the reference solution/code while a for any other code.

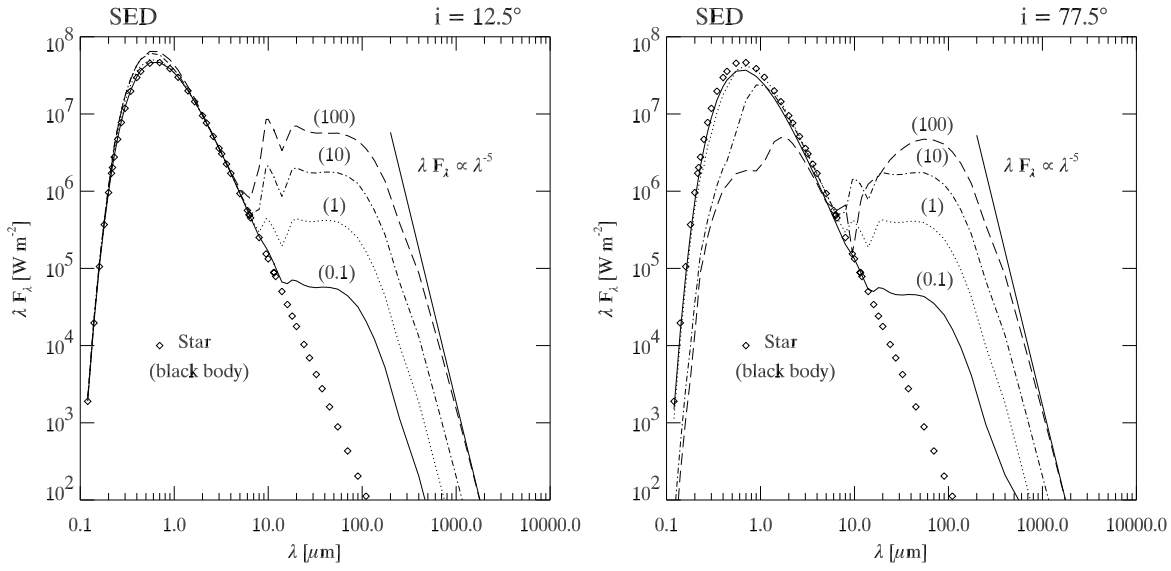

Figure 5.6: SED for two disk inclinations i as given on top of each panel. Each curve provides the mean value of the five RT simulations for the four computed models with different optical depth. The midplane optical depth is given in parenthesis labeling each curve. In both panels solid lines show results for the most optically thin disk, dotted lines for a disk having $\tau_{\rm v} = 1$, dot-dashed lines for a disk with $\tau_{\rm v} = 10$ and dashed lines for the most optically thick model. Diamonds provide the black-body emission from the naked star. The slope of the SED at long wavelengths depends only on the dust properties and is plotted in each panel with a solid line.

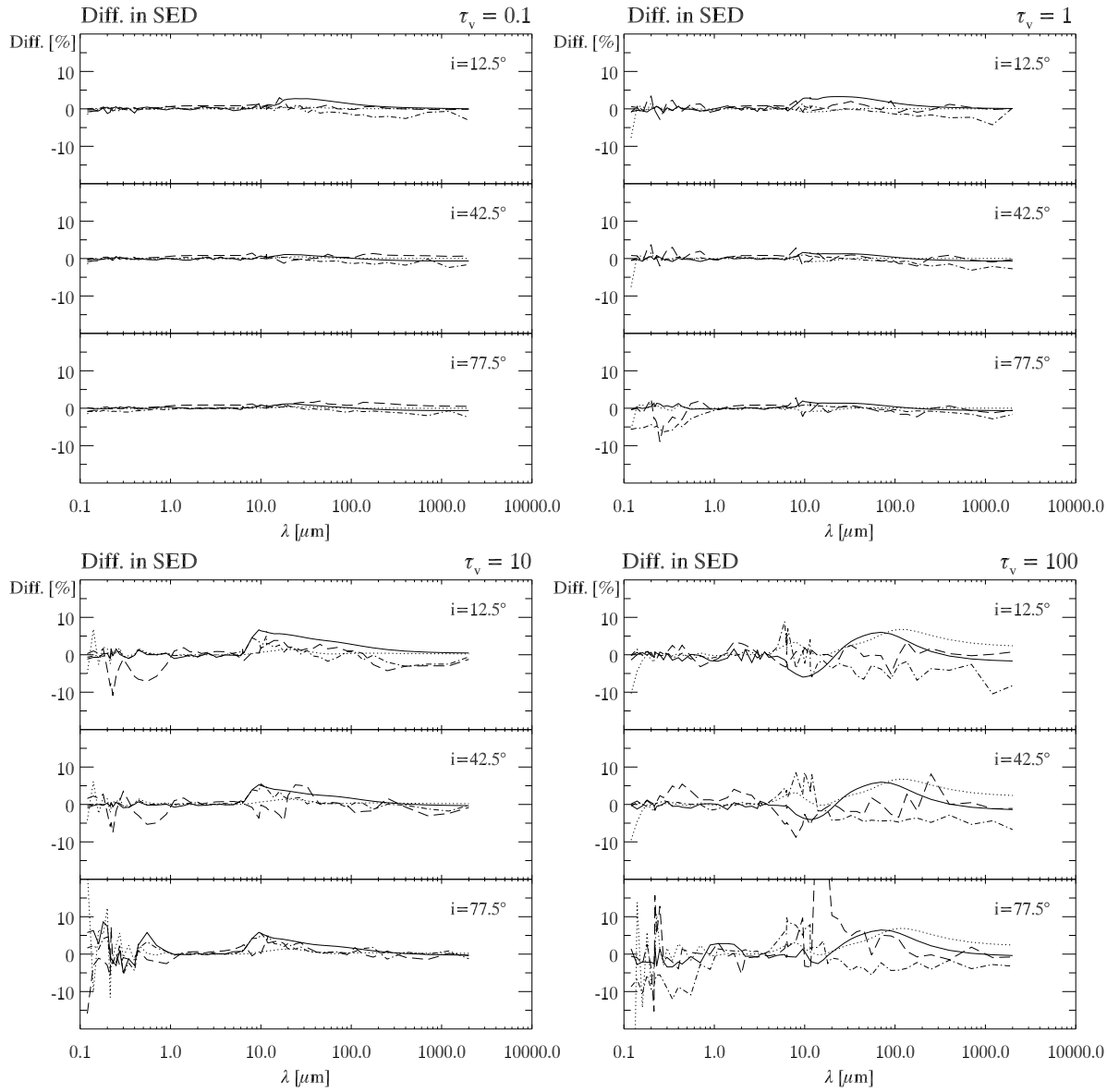

Figure 5.7: Percentage of difference in the SED between the codes. RADICAL is taken as reference code. Solid lines give the difference between MC3D and RADICAL, dot-dashed lines between MCTRANSF and RADICAL, dotted lines between RADMC and RADICAL and dashed lines between STEINRAY and RADICAL.

We also superimpose in diamonds the black body radiation arising from the star in order to visualize how efficiently the circumstellar disk reprocesses the stellar energy. We note that all the codes have the correct slope at long wavelengths. This slope depends only on the dust properties and is plotted as solid line in both panels ($\lambda F_\lambda \propto \lambda^{-5}$). At 0.55 μm the drop in luminosity amounts to about a factor of 20 going from the most optically thin to the most optically thick model and for a disk inclination of 77.5°.
Since the differences among the codes are too small to be visible in a logarithmic plot, we provide separately the percentage of difference for the four models and for three disk inclinations (see Fig. 5.7). RADICAL has been chosen as reference code. For the most optically thin case, we also compare our results with the semi-analytical approach (see Fig. 5.4). We find that the agreement of the codes with the semi-analytical solution is always better than 8%, with the largest deviations around 0.3 and 40 μm. In the range 0.2–0.7 μm all the codes predict higher flux in comparison to the semi-analytical solution, while between 10–200 μm a lower flux is obtained. These deviations arise because the semi-analytical approach includes scattering only as an extinction term. From the numerical RT calculations it is clear that some photons are scattered thus enhancing the flux between 0.2 and 0.7 μm. We note that this wavelength range is exactly where small astronomical silicate grains have the largest scattering efficiency (see Fig. 5.1). Therefore, deviations peaking at 0.3 μm are simply explained by the particular optical data chosen for this benchmark. Those photons which are scattered cannot contribute to heat the disk. This explains why RT codes predict a lack of emission at longer wavelengths. To understand why the largest deficit of photons is around 40–50 μm, we first compute the temperature at which most of the disk mass emits (mass average temperature) and then the corresponding wavelength. For the wavelength calculation we need to take into account the grain emissivity (Evans 1994). We find a mass average temperature of 40 K which translates into a wavelength of 50 μm at the maximum emission. This wavelength is well in agreement with the deviations shown in Fig. 5.4. For comparison, the RT codes agree better than 1.5% at wavelengths shorter than 10 μm for this particular test case ($\theta = 12.5°$). At longer wavelengths the results show a bit more scatter but the agreement is always better than 3%. In Fig. 5.7 first panel, we also show the percentage of difference for two other disk inclinations, namely 42.5° and 77.5°. In both cases the agreement is better than 2% at all wavelengths for all the codes but MCTRANSF, for which slightly higher deviations (about 2.5%) are present at longer wavelengths.
As the optical depth in the midplane increases, the RT problem becomes more difficult to solve. Because of the chosen disk geometry, most of the disk mass is located near to the midplane and close to the disk inner boundary. Our comparison shows that agreement among the codes is always better for an almost face-on case and 42.5° disk inclination (first two panels of Fig. 5.7), than for an almost edge-on disk (lower panels of Fig. 5.7). For the models with $\tau_{\rm v}$ =1 deviations among the codes are smaller than 9%. For the disk with midplane optical depth of 10 and 100 and inclinations of 12.5 and 42.5°, differences do not exceed 10%. For the almost edge-on configurations the most difficult regions to treat are those where scattering dominates and at wavelengths around 10 μm. In the IR, opacities change strongly and the modified Planck emission peaks in the inner disk regions (between 1 and 2 AU). Therefore, the numerical simulations are particularly sensible to the resolution of the inner parts. Deviations in the IR are partly due to the different resolution adopted by the codes (see also Sect. 5.4.4). Scatter at visible and near-infrared wavelengths for MC3D, MCTRANSF, and RADMC is simply statistical noise, typical of MC simulations. This scatter becomes more prominent at high optical depths. We also note that MC3D and RADMC have the same trend for

Table 5.4: Relevant models for the spatial resolution tests

Model	# r	Δr [AU]	# θ	$\Delta\theta$ [$^\circ$]	#Phot [$\times 10^6$]
mod0	55	0.03–141	101	1.8	24.4
mod1	55	0.03–141	31	5.8	24.4
mod2	40	0.3–141	121	1.5	24.4
mod3	35	0.7–141	121	1.5	24.4
mod4	10^3	0.07–4.1	121	1.5	244

wavelengths larger than 10 μm and the model with $\tau_{\rm v}$ =100: they both estimate a larger IR emission than RADICAL with peaks at $\sim$70 μm for MC3D and at $\sim$100 μm for RADMC. A strong deviation from the other codes is shown by STEINRAY just after the 9.8 μm silicate feature. However, one should note that apart from the discussed features *the overall agreement of the SEDs is better than 10% for all the codes even for the almost edge-on disk and the most optically thick test case.*

5.4.4 Tests for various spatial and frequency resolutions

We used the MC code MC3D to *test the dependence of our results on the grid adopted to store the emerging temperature.* Since deviations due to different temperature sampling are expected to be larger for more optically thick configurations, we investigate our most optically thick test case $\tau_{\rm v} = 100$. Different grids, covering radial resolutions from 2.7 AU up to 0.03 AU in the inner disk and vertical resolutions from 1.5° to 5.8°, have been inspected. In Fig. 5.8, we report results for five relevant cases. The number of radial and vertical subdivisions (#r and #θ), as well as the resolution (Δr and $\Delta\theta$) and total number of photons (#Phot) for these cases are provided in Table 5.4. The RT equation is solved for 61 wavelengths, the same assumed in all the previous simulations. The number of photons is set to 4×10^5 per wavelengths to limit the runtime to 2 days on a PC with 4 Gby memory, 2.4 GHz clock. Only in one case (*mod4*) we let the computation run for about two weeks in order to reduce as much as possible the photon noise at short wavelengths. The comparison shows that the vertical spacing does not influence too much the results: we report deviations smaller than 1.5% for the three disk inclinations between the models with vertical resolution 1.5° and 5.8° (solid line in Fig. 5.8). On the other side, changes in the radial grid strongly affects the IR emission: when going from *mod0* to *mod2* results still do not differ more than 5% but the coarse inner grid of *mod3* causes deviations larger than 20%. Model *mod4* is the state-of-the-art for our computer capabilities. The grid has a good resolution also in the outer region of the disk and we use 10 times more photons per wavelengths. The percentage of difference between this model and *mod0* in the IR regime amounts to less than 6%. Deviations of about 10% in the optical range are due to differences in the number of photons.
To *test the influence of the frequency resolution* on our results we run the 2 MC codes MC3D and RADMC doubling the number of walenghts where to solve the RT equation. The other three codes could not take part to the comparison because of not enough computer memory. To have reasonable runtime for MC3D (a couple of days), we restrict ourselves to the case $\tau_{\rm v} = 10$ and we lower the number of photons in comparison to Table 5.3 (half in the case of

RADMC and 4 times lower in the case of MC3D). The lower number of photons introduces larger scatter at short wavelengths. Fig. 5.9 shows the percentage of difference between MC3D and RADMC for the model with 61 wavelenghts (dotted line) and the new model with 122 wavelenghts (dashed line). Apart from the expected larger deviations at short wavelengths, the agreement between the two codes improves not more than 2% around 10μm. Thus, we conclude that the nature of the IR deviations plotted in Fig. 5.7, is not due to coarse frequency sampling but to the different grid resolutions adopted by the codes (especially in radial direction) together with cumulative numerical errors.

5.5 Discussion and conclusions on the 2D benchmark

Before presenting our findings, we briefly discuss the general features of the computed SEDs for different viewing angles (i) and optical depths (τ). As mentioned in Sect. 5.2.2, optical depths are measured in the disk midplane from the inner to the outer boundary. Thus, the optical depths we refer to are the highest in the disk.
Both panels of Fig. 5.6 show clearly that the far-infrared region (longward 100 μm) remains unaffected when varying the viewing angle. On the other hand, the short-wavelength part of the spectrum is strongly modified. When the disk is seen face-on the spectrum is dominated by unattenuated stellar radiation. As the disk inclination increases, more and more of the stellar flux is extincted by the dust in the disk. For the $\tau_{\rm v} = 100$ case at $i = 77.5^\circ$ this reduction amounts to a factor of e^{-100} in the visual. However, due to the high albedo of the dust grains, a large fraction of the stellar radiation is scattered above the disk into the line of sight. Dust scattering is also responsible for the excess of emission at stellar wavelengths seen at small disk inclinations (see left panel of Fig. 5.6 especially for high optical depths). The optical depth also affects the strong 10 μm feature produced by the SI – O stretching. While in most cases the feature appears strongly in emission, for the $\tau_{\rm v} = 100$ test case at $i = 77.5^\circ$ the feature appears in absorption (see Fig. 5.6 right panel). The 20 μm feature is much weaker than the 10 μm, but it is already visible for the model with $\tau_{\rm v} = 1$. All these features are in agreement with earlier radiative transfer computations of disks (e.g. Efstathiou and Rowan-Robinson 1990; Men'shchikov and Henning 1997).
Our aim is to provide benchmark solutions for the 2-D continuum radiative transfer problem in circumstellar disks. The problems we present have optical depths up to 100, which is actually the limit of current computational capabilities for most of the codes. The corresponding total mass in the disk of about 0.01 solar masses covers most of the observed disks around low mass stars. For more massive disks around intermediate and high-mass stars as well as tori obscuring active galactic nuclei, the numerical strategies have to be modified, using e.g. the diffusion approximation for high optical depths.
We used five independent radiative transfer codes that implement different numerical schemes. We compared both the resulting temperature structure and the emerging SEDs. For the lowest optical depth case ($\tau_{\rm v} = 0.1$) we also compared the results against a semi-analytic solution which treat scattering only as extinction term. The other three cases ($\tau_{\rm v} = 1, 10, 100$) cannot be solved in a semi-analytic way, since multiple scattering and absorption-reemission events strongly affect the solution.
We find that the overall shape of the temperature distribution and of the emerging SEDs is well reproduced by all the codes. Differences in the temperature are smaller than 1 % for all the codes in the most optically thin case. Even for the most optically thick model, differences

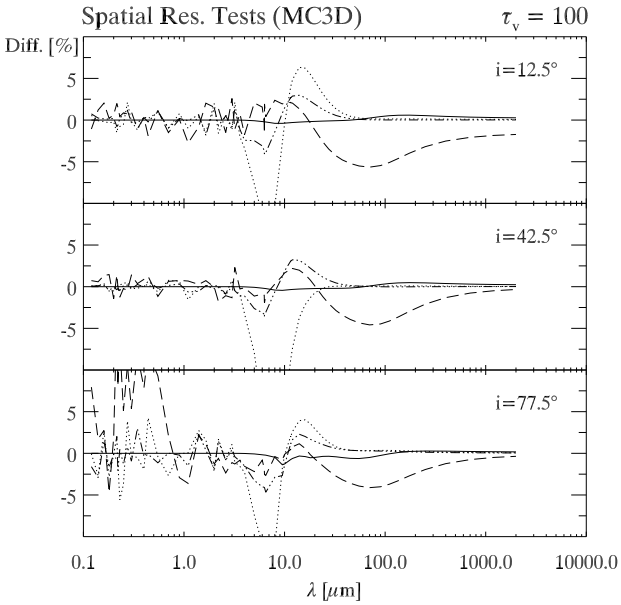

Figure 5.8: Spatial resolution tests using the MC code MC3D. On the y-axis we plot the percentage of difference between the emerging SED of *mod0* and any other model in Table 5.4. Solid line: difference between *mod0* and *mod1*. Dot-dot dahsed line: difference between *mod0* and *mod2*. Dotted line: difference between *mod0* and *mod3*. Dashed line: difference between *mod0* and *mod4*.

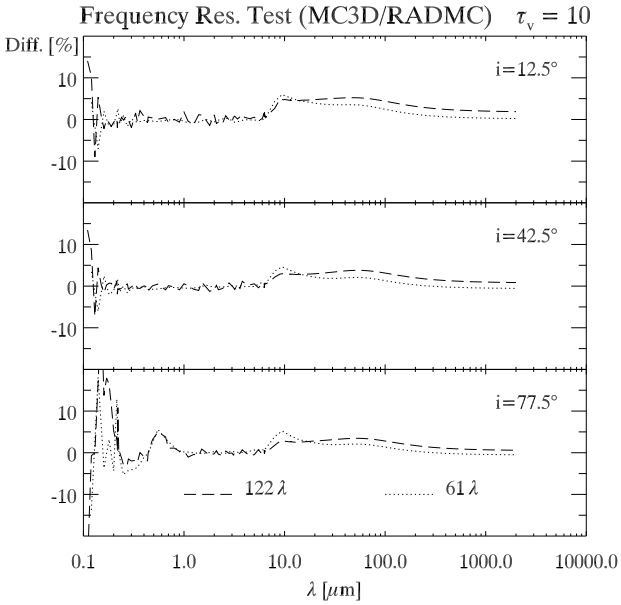

Figure 5.9: Frequency resolution test using the MC codes MC3D and RADMC. On the y-axis we plot the percentage of difference between the emerging SED of the codes for two models, one sampling the frequency space with 61 (dotted line) and the other with 122 (dashed line) logarithmically distributed points.

in the temperature remain below 15%. As for the SEDs, deviations among the codes are smaller than 3% at all wavelengths and disk inclinations for the most optically thin model. For the models with $\tau_{\rm v} = 1$ and 10 at all disk inclinations and for the most optically thick case for disk inclinations of 12.5 and 42.5°, differences do not exceed 10%. Only for the most optically thick case and an almost edge-on disk differences around 10 μm exceed 20% in the case of STEINRAY. We stress that this is the case for which the numerics is the most difficult: the codes have to treat both a very optically thin atmosphere and a thick disk midplane. Independent tests using two of the MC codes show that the frequency resolution cannot account for the infrared deviations among the codes in the almost edge-on disk and the most optically thick model. Grid resolution especially in radial direction together with cumulative numerical errors play a major rule. *The presented results provide a robust way to test other continuum RT codes and demonstrate the possibilities of the current computational capabilities.* Temperature distributions and SEDs for all the test cases are available at the web site: http://www.mpia.de/PSF/PSFpages/RT/benchmark.html
In the next sections of this Chapter, we explore the possibility of using RT codes to interpret and predict interferometric measurements. We also present the first comparison of images/visibilities from two RT codes implementing different numerical schemes.

5.6 An application to interferometric observations

The high resolution and sensitivity of the Very Large Telescope Interferometer (VLTI) will soon improve our knowledge in many fields of astrophysics. However, the first VLTI data will be in form of visibilities that require further analysis to be correctly interpreted. Hence, there is an ample need for multidimensional RT codes, treating complex configurations with high resolution and accuracy. Some 2D and a few 3D dust continuum RT codes have been developed and recently improved (Lopez et al. 1995; Dullemond and Turolla 2000; Wolf 2003; Steinacker et al. 2003). As results most of them provide not only SEDs but also wavelength-dependent images. These images have key importance for the interpretation of observed visibilities (see Sect. 3.1 for an introduction to interferometry).
In the previous sections of this Chapter, we demonstrated the reliability of RT codes by the first 2D dust continuum RT benchmark. Five RT codes implementing different numerical schemes have been compared in a 2D disk configuration: three of the codes apply the Monte-Carlo (MC) technique while the other two are grid-based codes. The two 3D radiative transfer codes participating in the benchmark, namely MC3D (Wolf 2003) and STEINRAY (Steinacker et al. 2002a, 2003), are able to handle complex configurations without severe restriction on optical dust properties or dust distribution. Here, we demonstrate the capabilities of the codes in producing mid-infrared (MIR) images for a distorted disk. We *compare for the first time images and visibilities produced by two different RT codes and we also investigate for which parameters the distortion of the disk can be best detected by the VLTI mid-infrared interferometric instrument MIDI* (for a description of the instrument see Sect. 3.2).

5.6.1 First image/visibility comparison

The 2D radiative transfer benchmark aimed to compare both emerging temperatures and SEDs from defined disk configurations. As a natural step, we extend our comparison to the images. For this purpose we make use of two of the tested codes that apply different methods to solve the dust continuum RT equation: MC3D is a Monte Carlo code while STEINRAY

Table 5.5: Model parameters

Parameter	value
Stellar mass, radius, temperature	$1\,M_\odot$, $1\,R_\odot$, 5800 K
Inner-outer disk radius	1-1000 AU
Grain type, radius	Silicate[a], 0.12 μm
Optical depth at 550 nm (τ_v)	1[b]
Ring location, width	25 AU, 3.5 AU

[a] Draine and Lee (1984)
[b] τ_v is calculated in the disk midplane from the inner to the outer disk radius.

is a grid-based code. Simulated images, and corresponding visibilities, are extremely useful for both the preparation of interferometric observations and for a correct interpretation of interferometric data.
Distorted disks are relevant to understand the formation and evolution of circumstellar disks and for their connection with the formation of low-mass stars and possibly planets. Numerical simulations show that star-disk and disk-disk encounters influence the initial disk density distribution by inducing two-armed spiral structures (Pfalzner et al. 2000). Similar arms are predicted by high-resolution numerical simulations in circumbinary disks surrounding classical T Tauri stars (Günther and Kley 2002). D'Angelo et al. (2002) performed hydrodynamical calculations that clearly show a wave pattern induced by planet-disk interactions.
The interesting question is about the detectability of these disk features. The MIR appears to be a promising spectral region to investigate because it probes those warm regions of the disk that are not contaminated by the stellar atmospheres. Sub-arcsec resolution is mandatory to resolve those inner arms that have higher density contrast. Wolf et al. (2002a) explored the possibility of detecting gaps in circumstellar disks caused by planets. Here, we focus on the detectability of spiral density waves.
As a simplified version of an azimuthally extended distortion, we consider a ring at 25 AU with a density five times larger than the local density taken from one of the the disk models tested in the benchmark. The assumed density contrast is in agreement with the numerical simulations previously cited. These numerical simulations also show that the spiral width varies strongly with the distance from the central object and with the distance and nature of the disturbing object: typical widths range from a few tenths of an AU to several AU. For the presented calculations, we have assumed a width of 3.5 AU. Star and disk parameters are summarized in Table 5.5 for clarity. We compute images at 20 μm for both a face-on and an edge-on case. Visibilities are calculated with the SIMVLTI tool[9] for the longest baseline (UT1-UT4) available at the VLTI, a source distance of 150 pc (typical of T Tauri stars in nearby star-forming regions) and declination of -30^o. In Fig. 5.10 we present the resulting images only for the face-on configuration. To enhance the contrast between the faint disk emission and the ring, we show only the inner 100×100 AU and we scale the intensities to the power of 0.25. The middle panel of Fig. 5.10 provides the corresponding visibilities: dashed line for MC3D and dotted line for STEINRAY. A vertical arrow is drawn to visualize the spatial frequency at which the ring shows up. The ring appears with similar extent and

[9] http://www.mpia-hd.mpg.de/MIDI/SIMVLTI/

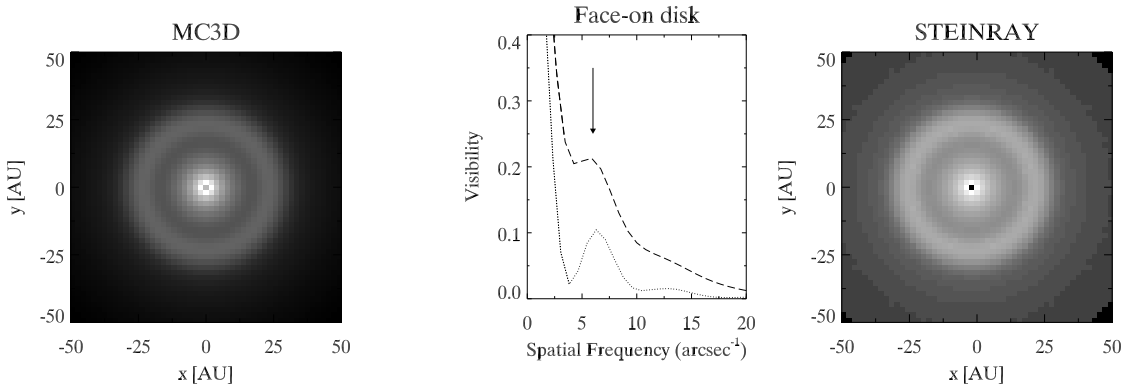

Figure 5.10: Images and visibilities for the face-on disk (model given in Table 5.5). Left panel: 20 μm image obtained with MC3D. Right panel: 20 μm image simulated with STEINRAY. Middle panel: visibility curve computed for the baseline UT1-UT4: dashed line for MC3D, dotted line for STEINRAY.

flux in both simulations. The difference in flux in the entire image is smaller than 20%. The main finding of these simulations is that both RT codes predict a detectable ring. The discrepancy in the overall shape of the visibility curve originates from a different intensity distribution that may be due to the fact that STEINRAY predicts a slightly warmer inner disk in comparison to MC3D. Another source of deviations may be the different temperature grid used by the codes to store the results: an appropriate 2D grid is used in MC3D for these particular simulations while a 3D grid is used in STEINRAY.

5.6.2 Investigating the disk parameters

In this section we investigate for which parameters the ring can be best detected by MIDI. The following RT simulations are performed using MC3D. We always show the inner 200×200 AU in order to have the same scale for all the considered cases. Intensities are scaled to the power of 0.25 as in Fig. 5.10.

At first we inspect the effect of the disk inclination. Among the various computations, the two extreme cases of a face-on and an edge-on disk are presented in Fig. 5.11. The computed visibilities clearly show that the ring detectability is only marginally influenced by the disk inclination. This could be due to the fact that the ring is almost completely optically thin for the chosen disk configuration and the observing wavelength. If we compute the same models for a disk that has a 100 times higher optical depth, we find that the ring is still detectable in the edge-on case but not anymore in the face-on configuration (see Fig. 5.12).

Another important parameter to investigate is the ring location. We consider the original face-on disk having $\tau_{\rm v}$=1 and we compute models for rings that are located in an interval from 10 to 50 AU from the star. Since the disk is resolved, the visibility is small for large spatial frequencies (dashed line of Fig. 5.13). This implies that is easier to detect rings that are farther away than 10 AU from the star, i.e. for spatial frequencies < 15 arcsec^{-1}. On the other hand, rings become undetectable when located too far from the star. At about 50 AU, we are in the region of exponential decrease of the visibility curve and a density increase of a factor of 5 over the local density cannot be seen in the visibility (dotted line of Fig. 5.13). We conclude that rings can be detected by MIDI when located between 10-40 AU. Finally,

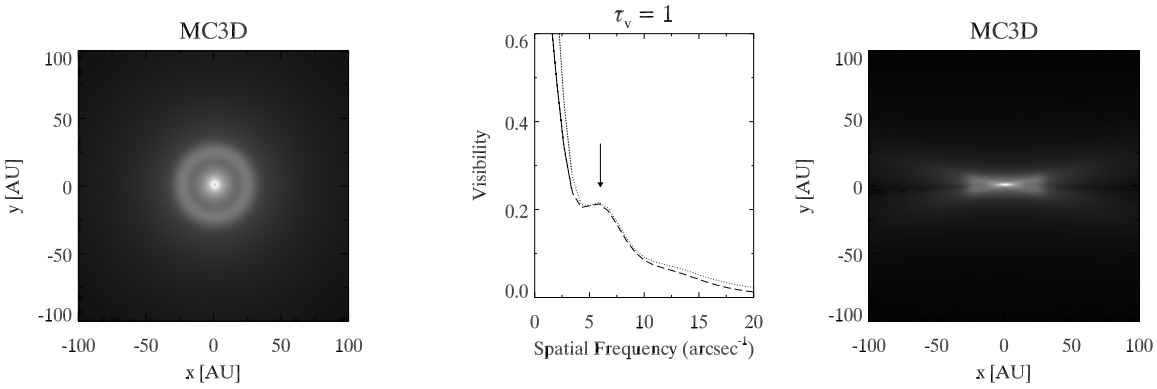

Figure 5.11: Images and visibilities for the thin disk (τ_v=1). Left panel: 20 μm face-on disk. Right panel: 20 μm edge-on disk. Middle panel: visibility curve computed for the baseline UT1-UT4. Dashed line: face-on disk, dotted line: edge-on disk.

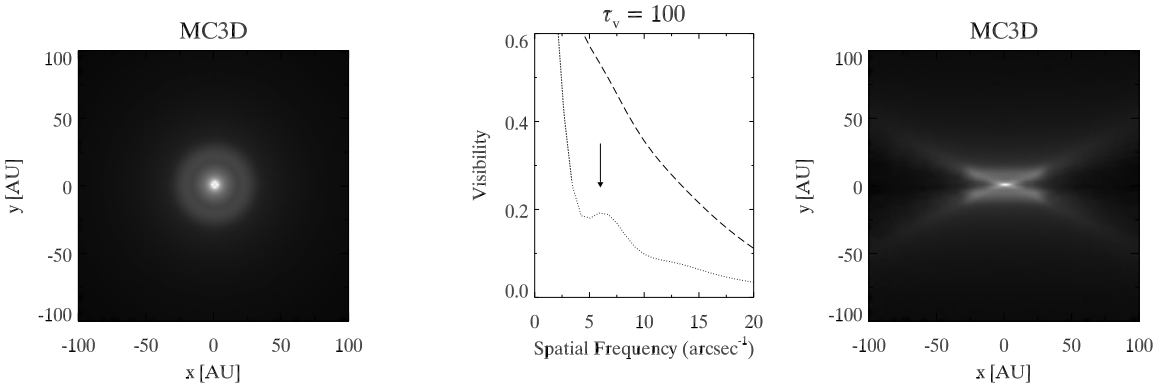

Figure 5.12: Images and visibilities for the thin disk (τ_v=100). Left panel: 20 μm face-on disk. Right panel: 20 μm edge-on disk. Middle panel: visibility curve computed for the baseline UT1-UT4. Dashed line: face-on disk, dotted line: edge-on disk.

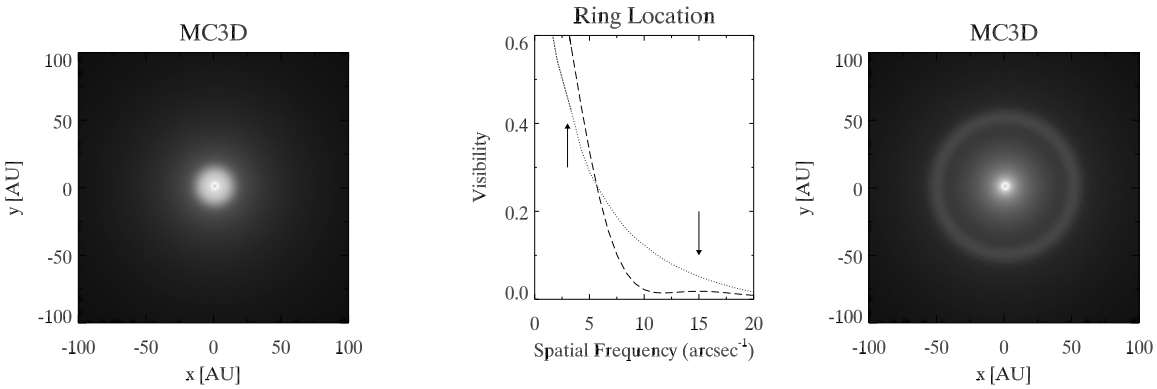

Figure 5.13: 20 μm images and visibilities for a disk with a ring located at 10 AU (left panel) and at 50 AU (right panel). Middle panel: visibility curve computed for the baseline UT1-UT4: dashed line for the ring at 10 AU, dotted line for the ring at 50 AU. At these distances rings become hardly detectable in the visibility curve.

we inspect the minimum density contrast necessary to detect the ring. We cover density contrasts ranging from 2 to 8 and find that for a ring at 25 AU a minimum density contrast of approximately 4 is required. As suggested by the previous results, the minimum density contrast for the ring detectability also depends on its location.

5.6.3 Conclusions

We have presented the first comparison of images/visibilities produced by two three-dimensional dust continuum RT codes based on very different methods. *Both codes predict that features like rings in a disk can be detected in the mid-infrared with MIDI.* Further analysis is necessary to study in detail how many visibilities are required to detect such a ring in a real source with realistic noise.
In addition, we have used the Monte Carlo code to explore for which parameters the ring can best detected with MIDI. We have demonstrated that such a ring is detectable with MIDI even for high optical depth if the disk is close to edge-on and that it is easier to detect rings located between 10–40 AU and have a minimum density contrast of 4. The next step of this work would be to adopt the density distributions predicted from numerical simulations of star/disk encounters, and study in detail which parameters of the spiral-like pattern can be determined with interferometric observations.

Results from the comparison of RT codes in 2D configurations are included in a paper accepted for publication in the Astronomy & Astrophysics Journal. The application of RT codes to interferometric observations has been presented at the JENAM 2002 conference (Pascucci et al. 2003b).

Chapter 6

Conclusions and Prospects

This thesis has investigated the early stages of massive star formation and the impact of high-mass stars on their surroundings. Relevance was given to the potential of new observational techniques and to the tools that can be used to interpret these observations.

The first Chapter presented our mid-infrared campaign conducted to search for the youngest massive (proto)stars. We targeted the two well-known star-forming region G10.47+0.03 and W3(OH) that harbour sources in the hot core and ultra-compact H II phases and aimed to study their relation. In the case of G10.47+0.03, three ultra-compact H II regions are still embedded in the hot molecular core and we demonstrated the importance of establishing an accurate astrometric frame to correctly interpret the mid-infrared data. For the same region, mid-infrared spectroscopy yielded the classification of the massive stars ionizing two of the ultra-compact H II regions. Our deep mid-infrared images detected and resolved the thermal emission from dust surrounding the less embedded ultra-compact H II sources in the G10.47+0.03 and in the W3(OH) regions. However, the protostars heating the hot molecular cores had no infrared counterpart at any wavelengths of our observations. This result implies line-of-sight extinction of at least 230 mag in the optical. We distinguished two components in the spectral energy distribution of W3(OH), with the ultra-compact H II region being the hotter, more evolved object and the hot core emission dominating at far-infrared wavelengths. From the simulated spectral energy distribution of the hot core we predict that deep Q-band images could unveil the massive protostar(s). The MIPS camera on board of SPITZER has the sensitivity to pursue the search for the infrared counterparts of hot molecular cores. However, the poor resolution might not be sufficient to spatially separate any multiple components.

Interferometry is certainly the way to attain resolutions well superior to conventional single-dish observations. In Chapter 3, we presented the first interferometric measurements towards the young massive star M8E IR obtained with MIDI, the new mid-infrared instrument for the VLTI. The choice of M8E IR was motivated by early infrared lunar occultation observations suggesting the existence of a circumstellar disk around the massive B0 star. Our single-dish acquisition images resolved an extended thermal component of about 200 AU slightly elongated in the east-west direction. The interferometric data were obtained with a baseline almost parallel to the direction of the predicted disk and provided a good-quality visibility curve between 8 and 13 μm. The low visibility values demonstrated that the thermal dust emission was well resolved by MIDI in the observed wavelength range. The extension of the

emitting region was estimated to be between 30 and 50 AU assuming a Gaussian distribution as source brightness. The visibility curve of the massive star M8E IR remarkably differs from the visibility curves of Herbig Ae stars. Optical depth effects as well as the geometry of the dust distribution might explain the observed differences. These effects are expected to be disentangled by obtaining new visibility measurements with a perpendicular baseline orientation and by comparing the observed visibilities with simulated visibility curves.

The impact of high-mass stars on their surroundings has been studied in Chapter 4 by high-resolution near-infrared observations of the massive star Θ^1 C Ori in the Orion Nebula. Our images show in great details the interaction of the Lyman-continuum flux and the wind from the massive star with the gas and dust envelopes around pre-main sequence stars (proplyds). We detected at least three near-infrared sources close to Θ^1 C Ori that are likely to be low-mass main-sequence stars based on their near-infrared colours and on the absence of line emission. The binary proplyd Orion 168-326 was well resolved at all the observed wavelengths and the interaction between the components appeared as a prominent arc-like emission in our Brγ continuum-subtracted exposures. We also reported a marginal detection of the microjet from the SE component at 2 μm. The nature of the object Orion 163-323, that lies at only 2$''$ projected distance from Θ^1 C Ori, has been investigated in detail. Its near-infrared colours and the compact line emission points towards a proplyd with the peculiarity of being seen almost face-on. From the inspection of the sizes and flux densities at different wavelengths, we concluded that we probably detected the star in the proplyd at 2 μm. We attributed the excess emission in the J-band to scattering from dust. The very bright and compact mid-infrared emission is explained by thermal dust emission. The presented observations could not decide whether most of the dust emitting in the J- and N-bands is located in the disk or just behind the spherical ionization front caused by the interaction of the stellar wind from Θ^1 C Ori and the disk wind. We suggested that accurate extinction measurements and interferometric observations could resolve and locate the amount of dust in the disk.

In view of the upcoming high-resolution observations towards massive young stars, we investigated the current capabilities of continuum radiative transfer codes in modeling circumstellar disks (Chapter 5). We considered a set of well-defined cases differing in optical depth and viewing angle and compared the emerging temperatures and spectral energy distributions from five independent radiative transfer codes implementing different numerical schemes. Differences in the outputs are in overall less than 10% even for the most optically thick case. Our solutions provide the first benchmark for disk configurations and can be used to test the reliability of other radiative transfer codes. The most optically thick case we considered corresponds to a total disk mass of about 0.01 solar masses and is at the limit of current computational capabilities. Diffusion approximation for high optical depths must be included to model more massive disks. In the last section of this Chapter, we presented an application of radiative transfer codes to interferometric observations. We considered the case of a disk with an azimuthally extended distortion due to star/disk encounters and compared the mid-infrared images and visibilities from two of the codes tested in the benchmark. We have demonstrated that such a distortion is detectable with MIDI even for high optical depth if the disk is close to edge-on and investigated the location and contrast density for which it is easier to detect. A natural continuation of this study is to use the density distributions predicted from numerical simulations of star/disk encounters and study in detail which parameters of the spiral-like pattern can be determined with interferometric observations.

Appendix A

Lyman continuum–Emission line Relation

Here, we derive the equation that links the Lyman continuum flux of an H II region to the emission line flux from any ion in the region. This equation has been used in Sect. 2.5 to derive the spectral type of the embedded ionizing star from the observed prohibited [NeII] line emission.
We start from considering the expression for the non-extincted intensity of an emission line I_λ (see Osterbrock 1974, equation 5.29)

$$I_\lambda = \int n_{\rm ion}\, n_{\rm e}\, \epsilon_\lambda\, ds \tag{A.1}$$

where $n_{\rm ion}$ is density of the ion responsible for the emission, $n_{\rm e}$ is the electron density, ϵ_λ is the emission coefficient of the line. The integral is taken along the line of sight (ds) through the H II region. Assuming that the emission coefficient is constant along the line of sight, we can write

$$I_\lambda = \epsilon_\lambda\, EM\, \left(\frac{n_{\rm ion}}{n_{\rm e}}\right)\, \frac{\Omega}{4\,\pi} \tag{A.2}$$

with Ω being the solid angle, EM the emission measure and $n_{\rm p} \sim n_{\rm e}$ is the proton density. We recall that the emission measure is defined as $EM = \int n_{\rm ion} \times n_{\rm p}\, ds$ that explains how equation A.2 is obtained from equation A.1. The EM of a spherically symmetric, optically thin, homogeneous, ionization bounded H II region is related to the opacity at a given frequency ν by (see Osterbrock 1974, equation 4.32)

$$EM = 12.143\, \tau_\nu\, T_{\rm e}^{1.35}\, \nu^{2.1} \tag{A.3}$$

Here, EM is measured in $\mathrm{pc\,cm^{-6}}$, $T_{\rm e}$ is the electron temperature in K, ν is the frequency in GHz and τ_ν the optical depth at the frequency ν. Following the convention used in radio astronomy, τ_ν is related to the brightness temperature $T_{\rm b}$ by (Osterbrock 1974, equation 4.37)

$$\tau_\nu = T_{\rm b}/T_{\rm e} \tag{A.4}$$

for an isothermal optically thin H II region. The brigthness temperature in the Rayleigh-Jeans approximation can be also expressed as (see e.g. Wood and Churchwell 1989)

$$T_{\rm b} = 1.1 \times 10^{-15}\, S_\nu\, \nu^{-2} \Omega^{-1} \tag{A.5}$$

where S_ν is the radio continuum flux density in Jy at a given frequency ν in GHz and Ω is the solid angle measured in steradian. Substituting equations A.3, A.4 and A.5 in equation A.2, we obtain:

$$I_\lambda = 9.70 \times 10^{13}\, \epsilon_\lambda\, T_{\rm e}^{0.35}\, \nu^{0.1}\, S_\nu \left(\frac{n_{\rm ion}}{n_{\rm e}}\right) \tag{A.6}$$

with I_λ the specific intensity measured in erg s^{-1} cm^{-2}, ϵ_λ in erg s^{-1} cm^3, T$_{\rm e}$ in K, ν in GHz and S_ν in Jy. On the other hand, the number of ionizing photons per second (Q_0) required to maintain the ionization of the H II region is (see e.g. Martín-Hernández et al. 2003, equation 5)

$$Q_0 = 2.489 \times 10^{48}\, T_{\rm e}^{-0.45}\, \nu^{0.1}\, D^2\, S_\nu \tag{A.7}$$

where D is the distance in kpc, $T_{\rm e}$ is the elctron temperature in K, ν the frequency in GHz and S_ν the radio continuum flux density in Jy. Making the ratio of equations A.6 and A.7 allows to express Q_0 as function of the non-extincted emission line from any ion in the H II region

$$Q_0 = 2.566 \times 10^{34}\, T_{\rm e}^{-0.8}\, D^2 \left(\frac{n_{\rm e}}{n_{\rm ion}}\right) \frac{I_\lambda}{\epsilon_\lambda} \tag{A.8}$$

Bibliography

Alcolea, J., Menten, K. M., Moran, J. M., and Reid, M. J. (1993). The proper motions of the H_2O masers near W3(OH). In *Astrophysical masers; Proceedings of the Conference, Arlington, VA, Mar. 9-11, 1992 (A93-52776 23-90)*, pages 225–228.

Allen, C. W. (1973). *Astrophysical quantities*. London: University of London, Athlone Press, —c1973, 3rd ed.

Anglada, G. (1996). Radio Jets in Young Stellar Objects. In *ASP Conf. Ser. 93: Radio Emission from the Stars and the Sun*, pages 3–7.

Apai, D., Pascucci, I., Henning, T., Sterzik, M. F., Klein, R., Semenov, D., Günther, E., and Stecklum, B. (2002). Probing Dust around Brown Dwarfs: The Naked LP 944-20 and the Disk of Chamaeleon Hα 2. *Astrophysical Journal Letters*, 573:L115–L117.

Arens, J. F., Jernigan, J. G., Peck, M. C., Lacy, J. H., and Gaalema, S. (1986). 10 Micrometer Infrared Camera. *Bulletin of the American Astronomical Society*, 18:968–969.

Bally, J., Sutherland, R. S., Devine, D., and Johnstone, D. (1998). Externally Illuminated Young Stellar Environments in the Orion Nebula: Hubble Space Telescope Planetary Camera and Ultraviolet Observations. *Astronomical Journal*, 116:293–321.

Baraffe, I., Chabrier, G., Allard, F., and Hauschildt, P. H. (1998). Evolutionary models for solar metallicity low-mass stars: mass-magnitude relationships and color-magnitude diagrams. *Astronomy and Astrophysics*, 337:403–412.

Beltrán, M. T., Cesaroni, R., Neri, R., Codella, C., Furuya, R. S., Testi, L., and Olmi, L. (2004). Rotating Disks in High-Mass Young Stellar Objects. *Astrophysical Journal Letters*, 601:L187–L190.

Bjorkman, J. E. and Wood, K. (2001). Radiative Equilibrium and Temperature Correction in Monte Carlo Radiation Transfer. *Astrophysical Journal*, 554:615–623.

Bonnell, I. A., Bate, M. R., and Zinnecker, H. (1998). On the formation of massive stars. *Monthly Notices of the Royal Astronomical Society*, 298:93–102.

Brand, J. (1986). The velocity field of the outer galaxy. *Ph.D. Thesis*.

Brandner, W., Grebel, E. K., Chu, Y., Dottori, H., Brandl, B., Richling, S., Yorke, H. W., Points, S. D., and Zinnecker, H. (2000). HST/WFPC2 and VLT/ISAAC Observations of Proplyds in the Giant H II Region NGC 3603. *Astronomical Journal*, 119:292–301.

Campbell, M. F., Lester, D. F., Harvey, P. M., and Joy, M. (1989). High spatial resolution far-infrared scans of W3(OH). *Astrophysical Journal*, 345:298–305.

Carpenter, J. M., Hillenbrand, L. A., and Skrutskie, M. F. (2001). Near-Infrared Photometric Variability of Stars toward the Orion A Molecular Cloud. *Astronomical Journal*, 121:3160–3190.

Cashwell, E. D. and Everett, C. J. (1959). *A practical manual on the Monte Carlo Method for random walk problems.* Pergamon, New York.

Caswell, J. L., Vaile, R. A., and Forster, J. R. (1995). Methanol and hydroxyl maser positions. *Monthly Notices of the Royal Astronomical Society*, 277:210–216.

Cesaroni, R., Hofner, P., Walmsley, C. M., and Churchwell, E. (1998). Sub-arcsecond structure of hot cores in the NH_3 (4,4) line. *Astronomy and Astrophysics*, 331:709–725.

Charnley, S. B. (1995). Hot Core Chemistry. *Astrophysics and Space Science*, 224:251–254.

Chiang, E. I. and Goldreich, P. (1997). Spectral Energy Distributions of T Tauri Stars with Passive Circumstellar Disks. *Astrophysical Journal*, 490:368–376.

Chiang, E. I. and Goldreich, P. (1999). Spectral Energy Distributions of Passive T Tauri Disks: Inclination. *Astrophysical Journal*, 519:279–284.

Chini, R., Kruegel, E., and Kreysa, E. (1986). Dust emission spectra from star-forming regions. *Astronomy and Astrophysics*, 167:315–324.

Churchwell, E. (2002). The Formation and Early Evolution of Massive Stars. In *ASP Conf. Ser. 267: Hot Star Workshop III: The Earliest Phases of Massive Star Birth*, pages 3–16.

Churchwell, E., Walmsley, C. M., and Cesaroni, R. (1990). A survey of ammonia and water vapor emission from ultracompact HII regions. *Astronomy and Astrophysics Supplement Series*, 83:119–144.

Churchwell, E., Wood, D. O. S., Felli, M., and Massi, M. (1987). Solar system-sized condensations in the Orion Nebula. *Astrophysical Journal*, 321:516–519.

Cohen, M., Walker, R. G., Barlow, M. J., and Deacon, J. R. (1992). Spectral irradiance calibration in the infrared. I - Ground-based and IRAS broadband calibrations. *Astronomical Journal*, 104:1650–1657.

Cohen, M., Walker, R. G., Carter, B., Hammersley, P., Kidger, M., and Noguchi, K. (1999). Spectral Irradiance Calibration in the Infrared. X. A Self-Consistent Radiometric All-Sky Network of Absolutely Calibrated Stellar Spectra. *Astronomical Journal*, 117:1864–1889.

Cohen, M., Witteborn, F. C., Walker, R. G., Bregman, J. D., and Wooden, D. H. (1995). Spectral Irradiance Calibration in the Infrared.IV. 1.2-35 micron spectra of six standard stars. *Astronomical Journal*, 110:275–289.

Collison, A. J. and Fix, J. D. (1991). Axisymmetric models of circumstellar dust shells. *Astrophysical Journal*, 368:545–557.

Cotera, A. S., Whitney, B. A., Young, E., Wolff, M. J., Wood, K., Povich, M., Schneider, G., Rieke, M., and Thompson, R. (2001). High-Resolution Near-Infrared Images and Models of the Circumstellar Disk in HH 30. *Astrophysical Journal*, 556:958–969.

D'Angelo, G., Henning, T., and Kley, W. (2002). Nested-grid calculations of disk-planet interaction. *Astronomy and Astrophysics*, 385:647–670.

De Buizer, J. M., Radomski, J. T., Telesco, C. M., and Piña, R. K. (2003). A Search for Mid-Infrared Emission from Hot Molecular Core Candidates. *Astrophysical Journal*, 598:1127–1139.

De Buizer, J. M., Watson, A. M., Radomski, J. T., Piña, R. K., and Telesco, C. M. (2002). Mid-Infrared Detection of a Hot Molecular Core in G29.96-0.02. *Astrophysical Journal Letters*, 564:L101–L104.

de Vicente, P., Martín-Pintado, J., Neri, R., and Rodríguez-Franco, A. (2002). On the Heating Source of the Orion KL Hot Core. *Astrophysical Journal Letters*, 574:L163–L166.

Dorschner, J., Begemann, B., Henning, T., Jaeger, C., and Mutschke, H. (1995). Steps toward interstellar silicate mineralogy. II. Study of Mg-Fe-silicate glasses of variable composition. *Astronomy and Astrophysics*, 300:503–520.

Draine, B. T. and Lee, H. M. (1984). Optical properties of interstellar graphite and silicate grains. *Astrophysical Journal*, 285:89–108.

Dullemond, C. P. and Dominik, C. (2004a). Flaring vs. self-shadowed disks: The SEDs of Herbig Ae/Be stars. *Astronomy and Astrophysics*, 417:159–168.

Dullemond, C. P. and Dominik, C. (2004b). Flaring vs. self-shadowed disks: the SEDs of Herbig Ae/Be stars. To appear in *Astronomy and Astrophysics*.

Dullemond, C. P. and Turolla, R. (2000). An efficient algorithm for two-dimensional radiative transfer in axisymmetric circumstellar envelopes and disks. *Astronomy and Astrophysics*, 360:1187–1202.

Dullemond, C. P., van Zadelhoff, G. J., and Natta, A. (2002). Vertical structure models of T Tauri and Herbig Ae/Be disks. *Astronomy and Astrophysics*, 389:464–474.

Dunn, D. E., Molnar, L. A., and Fix, J. D. (2002). More Microwave Observations of Saturn: Modeling the Ring with a Monte Carlo Radiative Transfer Code. *Icarus*, 160:132–160.

Dyson, J. E. and Williams, D. A. (1980). *Physics of the interstellar medium.* New York, Halsted Press, 1980. 204 p.

Efstathiou, A. and Rowan-Robinson, M. (1990). Radiative transfer in axisymmetric dust clouds. *Monthly Notices of the Royal Astronomical Society*, 245:275–288.

Efstathiou, A. and Rowan-Robinson, M. (1991). Radiative transfer in axisymmetric dust clouds. II - Models of rotating protostars. *Monthly Notices of the Royal Astronomical Society*, 252:528–534.

Egan, M. P., Price, S. D., Moshir, M. M., Cohen, M., and Tedesco, E. (1999). The Midcourse Space Experiment Point Source Catalog Version 1.2 Explanatory Guide. *NASA STI/Recon Technical Report AFRL-VS-TR-1999-1522*.

Elmegreen, B. G. (1991). Cloud formation by combined instabilities in galactic gas layers - Evidence for a Q threshold in the fragmentation of shearing wavelets. *Astrophysical Journal*, 378:139–156.

Evans, A. (1994). *The dusty universe*. Chichester ; New York : J. Wiley ; Chichester : In association with Praxis Pub., Ltd., 1994.

Fischer, O., Henning, T., and Yorke, H. W. (1996). Simulation of polarization maps. II. The circumstellar environment of pre-main sequence objects. *Astronomy and Astrophysics*, 308:863–885.

Fitzpatrick, E. L. (1999). Correcting for the Effects of Interstellar Extinction. *Publications of the Astronomical Society of the Pacific*, 111:63–75.

Günther, R. and Kley, W. (2002). Circumbinary disk evolution. *Astronomy and Astrophysics*, 387:550–559.

Garay, G. and Lizano, S. (1999). Massive Stars: Their Environment and Formation. *Publications of the Astronomical Society of the Pacific*, 111:1049–1087.

Garay, G., Moran, J. M., and Reid, M. J. (1987). Compact continuum radio sources in the Orion Nebula. *Astrophysical Journal*, 314:535–550.

Garay, G., Rodriguez, L. F., Moran, J. M., and Churchwell, E. (1993). VLA Observations of Strong IRAS Point Sources Associated with Compact H II Regions. *Astrophysical Journal*, 418:368–385.

García-Arredondo, F., Henney, W. J., and Arthur, S. J. (2001). Hydrodynamic Simulations of Proplyd Bow Shocks. *Astrophysical Journal*, 561:830–842.

Gibb, A. G., Wyrowski, F., and Mundy, L. G. (2002). Subarcsecond Imaging of Hot Cores with BIMA. In *Chemistry as a Diagnostic of Star Formation*, pages 32–37.

Gonçalves, J., Galli, D., and Walmsley, M. (2004). Monte Carlo radiative transfer in molecular cloud cores. *Astronomy and Astrophysics*, 415:617–625.

Graham, M. F., Meaburn, J., Garrington, S. T., O'Brien, T. J., Henney, W. J., and O'Dell, C. R. (2002). MERLIN Radio Detection of an Interaction Zone within a Binary Orion Proplyd System. *Astrophysical Journal*, 570:222–230.

Grevesse, N. and Sauval, A. J. (1998). Standard Solar Composition. *Space Science Reviews*, 85:161–174.

Hatchell, J., Fuller, G. A., Millar, T. J., Thompson, M. A., and Macdonald, G. H. (2000). SCUBA imaging of high mass star formation regions. *Astronomy and Astrophysics*, 357:637–650.

Hatchell, J., Thompson, M. A., Millar, T. J., and MacDonald, G. H. (1998). A survey of molecular line emission towards ultracompact HII regions. *Astronomy and Astrophysics Supplement Series*, 133:29–49.

Hayward, T. L., Houck, J. R., and Miles, J. W. (1994). Thermal infrared imaging of subarcsecond structure in the trapezium nebula. *Astrophysical Journal*, 433:157–163.

Hayward, T. L., Miles, J. E., Houck, J. R., Gull, G. E., and Schoenwald, J. (1993). SpectroCam-10: a 10-um spectrograph/camera for the Hale Telescope. In *Proc. SPIE Vol. 1946, Infrared Detectors and Instrumentation, Albert M. Fowler; Ed.*, pages 334–340.

Henning, T. (2001). Frontiers of Radiative Transfer. In *IAU Symposium*, pages 567–570.

Henning, T., Schreyer, K., Launhardt, R., and Burkert, A. (2000). Massive young stellar objects with molecular outflows. *Astronomy and Astrophysics*, 353:211–226.

Hillenbrand, L. A. (1997). On the Stellar Population and Star-Forming History of the Orion Nebula Cluster. *Astronomical Journal*, 113:1733–1768.

Hillenbrand, L. A. and Carpenter, J. M. (2000). Constraints on the Stellar/Substellar Mass Function in the Inner Orion Nebula Cluster. *Astrophysical Journal*, 540:236–254.

Hoare, M. G. and Garrington, S. T. (1995). Further Mapping of the Radio Emission from Massive Young Stellar Objects. *Astrophysical Journal*, 449:874–879.

Hofner, P. and Churchwell, E. (1996). A survey of water maser emission toward ultracompact HII regions. *Astronomy and Astrophysics Supplement Series*, 120:283–299.

Hofner, P., Wyrowski, F., Walmsley, C. M., and Churchwell, E. (2000). A C17O Survey toward Ultracompact H II Regions. *Astrophysical Journal*, 536:393–405.

Hollenbach, D. J., Yorke, H. W., and Johnstone, D. (2000). Disk Dispersal around Young Stars. *Protostars and Planets IV*, pages 401–428.

Humphreys, R. M. (1978). Studies of luminous stars in nearby galaxies. I. Supergiants and O stars in the Milky Way. *Astrophysical Journal Supplement Series*, 38:309–350.

Ivezic, Z., Groenewegen, M. A. T., Men'shchikov, A., and Szczerba, R. (1997). Benchmark problems for dust radiative transfer. *Monthly Notices of the Royal Astronomical Society*, 291:121–124.

Kaufman, M. J., Hollenbach, D. J., and Tielens, A. G. G. M. (1998). High-Temperature Molecular Cores near Massive Stars and Application to the Orion Hot Core. *Astrophysical Journal*, 497:276–287.

Keto, E., Proctor, D., Ball, R., Arens, J., and Jernigan, G. (1992). The environments of young stars - Mid-infrared and molecular line imaging. *Astrophysical Journal Letters*, 401:L113–L116.

Kikuchi, N., Nakamoto, T., and Ogochi, K. (2002). Disk-Halo Model for Flat-Spectrum T Tauri Stars. *Publications of the Astronomical Society of Japan*, 54:589–597.

Kunasz, P. and Auer, L. H. (1988). Short characteristic integration of radiative transfer problems - Formal solution in two-dimensional slabs. *Journal of Quantitative Spectroscopy and Radiative Transfer*, 39:67–79.

Kurtz, S., Cesaroni, R., Churchwell, E., Hofner, P., and Walmsley, C. M. (2000). Hot Molecular Cores and the Earliest Phases of High-Mass Star Formation. *Protostars and Planets IV*, pages 299–326.

Kurtz, S., Churchwell, E., and Wood, D. O. S. (1994). Ultracompact H II regions. 2: New high-resolution radio images. *Astrophysical Journal Supplement Series*, 91:659–712.

Kurtz, S. and Franco, J. (2002). Ultracompact H II Regions. In *Revista Mexicana de Astronomia y Astrofisica Conference Series*, pages 16–21.

Löwe, M., Stecklum, B., von der Lühe, O., and Quirrenbach, A. (1997). Pupil Mask Interferometry of M8E-IR. In *Science with the VLT Interferometer*, pages 379–380.

Lada, C. J. and Adams, F. C. (1992). Interpreting infrared color-color diagrams - Circumstellar disks around low- and intermediate-mass young stellar objects. *Astrophysical Journal*, 393:278–288.

Lada, E. A., Dutrey, A., Guilloteau, S., and Mundy, L. (1996). Circumstellar Disks in the Trapezium Cluster. *Bulletin of the American Astronomical Society*, 28:1342.

Laques, P. and Vidal, J. L. (1979). Detection of a new type of condensations in the center of the Orion Nebula by means of S20 photocathode cells associated with a Lallemand electronic camera. *Astronomy and Astrophysics*, 73:97–106.

Leinert, C., Graser, U., Przygodda, F., Waters, L. B. F. M., Perrin, G., Jaffe, W., Lopez, B., Bakker, E. J., Böhm, A., Chesneau, O., Cotton, W. D., Damstra, S., de Jong, J., Glazenborg-Kluttig, A. W., Grimm, B., Hanenburg, H., Laun, W., Lenzen, R., Ligori, S., Mathar, R. J., Meisner, J., Morel, S., Morr, W., Neumann, U., Pel, J.-W., Schuller, P., Rohloff, R.-R., Stecklum, B., Storz, C., von der Lühe, O., and Wagner, K. (2003a). MIDI - the 10 \mum instrument on the VLTI. *Astrophysics and Space Science*, 286:73–83.

Leinert, C., Graser, U., Waters, L. B. F. M., Perrin, G. S., Jaffe, W., Lopez, B., Przygodda, F., Chesneau, O., Schuller, P. A., Glazenborg-Kluttig, A. W., Laun, W., Ligori, S., Meisner, J. A., Wagner, K., Bakker, E. J., Cotton, B., de Jong, J., Mathar, R., Neumann, U., and Storz, C. (2003b). Ten-micron instrument MIDI: getting ready for observations on the VLTI. In *Interferometry for Optical Astronomy II. Edited by Wesley A. Traub . Proceedings of the SPIE, Volume 4838, pp. 893-904 (2003).*, pages 893–904.

Leinert, C., van Boekel, R., Waters, L. B. F. M., Chesneau, O., Malbet, F., Köhler, R., Jaffe, W., Ratzka, T., Dutrey, A., Preibisch, T., Graser, U., Bakker, E. J., Chagnon, G., Cotton, W. D., and al. (2004). Mid-Infrared sizes of circumstellar disks around Herbig Ae/Be stars measured with MIDI on the VLTI. Submitted to *Astronomy and Astrophysics.*

Leung, C. M. (1976). Radiation transport in dense interstellar dust clouds. II - Infrared emission from molecular clouds associated with H II regions. *Astrophysical Journal*, 209:75–93.

Linz, H., Stecklum, B., Henning, T., Hofner, P., and Brandl, B. (2003). The G9.62+0.19-F Hot Molecular Core - The infrared view on very young massive stars . Submitted to *Astronomy and Astrophysics*.

Lopez, B., Mekarnia, D., and Lefevre, J. (1995). Radiative transfer in axisymmetric circumstellar dust shells. *Astronomy and Astrophysics*, 296:752–760.

Lopez, B. and Perrin, J.-M. (2000). A dust envelope modelling of the Egg Nebula. *Astronomy and Astrophysics*, 354:657–666.

Lucy, L. B. (1999). Computing radiative equilibria with Monte Carlo techniques. *Astronomy and Astrophysics*, 344:282–288.

Malbet, F. and Bertout, C. (1991). The vertical structure of T Tauri accretion disks. I - Heating by the central star. *Astrophysical Journal*, 383:814–819.

Manske, V. and Henning, T. (1998). Two-dimensional radiative transfer with transiently heated particles: methods and applications. *Astronomy and Astrophysics*, 337:85–95.

Martín-Hernández, N. L., van der Hulst, J. M., and Tielens, A. G. G. M. (2003). A radio continuum and infrared study of Galactic H II regions. *Astronomy and Astrophysics*, 407:957–985.

Mathis, J. S., Rumpl, W., and Nordsieck, K. H. (1977). The size distribution of interstellar grains. *Astrophysical Journal*, 217:425–433.

Maxia, C., Testi, L., Cesaroni, R., and Walmsley, C. M. (2001). The kinematics of molecular clumps surrounding hot cores in G29.96 -0.02 and G31.41+0.31. *Astronomy and Astrophysics*, 371:287–299.

McCaughrean, M. J. and Stauffer, J. R. (1994). High resolution near-infrared imaging of the trapezium: A stellar census. *Astronomical Journal*, 108:1382–1397.

McKee, C. F. and Tan, J. C. (2002). Massive star formation in 100,000 years from turbulent and pressurized molecular clouds. *Nature*, 416:59–61.

Megeath, S. T. and Tieftrunk, A. R. (1999). The Detection of Outflows in the Infrared-quiet Molecular Core NGC 6334/I(North). *Astrophysical Journal Letters*, 526:L113–L116.

Men'shchikov, A. B. and Henning, T. (1997). Radiation transfer in circumstellar disks. *Astronomy and Astrophysics*, 318:879–907.

Mihalas, D., Auer, L. H., and Mihalas, B. R. (1978). Two-dimensional radiative transfer. I - Planar geometry. *Astrophysical Journal*, 220:1001–1023.

Mihalas, D. and Weibel Mihalas, B. (1984). *Foundations of radiation hydrodynamics*. New York: Oxford University Press, 1984.

Mitchell, G. F., Hasegawa, T. I., and Schella, J. (1992). A CO J = 2 - 1 study of the outflow sources GL 490, GL 2591, M8E-IR, and W3 IRS 5. *Astrophysical Journal*, 386:604–617.

Monnier, J. D. (2003). Optical interferometry in astronomy. *Reports of Progress in Physics*, 66:789–857.

Muench, A. A., Lada, E. A., Lada, C. J., and Alves, J. (2002). The Luminosity and Mass Function of the Trapezium Cluster: From B Stars to the Deuterium-burning Limit. *Astrophysical Journal*, 573:366–393.

Natta, A., Meyer, M. R., and Beckwith, S. V. W. (2000). Silicate Emission in T Tauri Stars: Evidence for Disk Atmospheres? *Astrophysical Journal*, 534:838–845.

Niccolini, G., Woitke, P., and Lopez, B. (2003). High precision Monte Carlo radiative transfer in dusty media. *Astronomy and Astrophysics*, 399:703–716.

O'Dell, C. R. (2001). The Orion Nebula and its Associated Population. *Annual Review of Astronomy and Astrophysics*, 39:99–136.

O'Dell, C. R. and Wen, Z. (1994). Postrefurbishment mission Hubble Space Telescope images of the core of the Orion Nebula: Proplyds, Herbig-Haro objects, and measurements of a circumstellar disk. *Astrophysical Journal*, 436:194–202.

O'Dell, C. R., Wen, Z., and Hu, X. (1993). Discovery of new objects in the Orion nebula on HST images - Shocks, compact sources, and protoplanetary disks. *Astrophysical Journal*, 410:696–700.

O'Dell, C. R. and Wong, K. (1996). Hubble Space Telescope Mapping of the Orion Nebula. I. A Survey of Stars and Compact Objects. *Astronomical Journal*, 111:846–856.

Okamoto, Y. K., Kataza, H., Yamashita, T., Miyata, T., and Onaka, T. (2001). High-Resolution Mid-Infrared Imaging and Spectroscopic Observations of a Massive Star Forming Region W51 IRS 2. *Astrophysical Journal*, 553:254–266.

Okamoto, Y. K., Kataza, H., Yamashita, T., Miyata, T., Sako, S., Takubo, S., Honda, M., and Onaka, T. (2003). K3-50A: An Ultracompact H II Region Ionized by a Massive Stellar Cluster. *Astrophysical Journal*, 584:368–384.

Olmi, L., Cesaroni, R., Neri, R., and Walmsley, C. M. (1996a). High resolution CH_3CN observations towards hot cores. *Astronomy and Astrophysics*, 315:565–577.

Olmi, L., Cesaroni, R., and Walmsley, C. M. (1996b). CH_3CN towards G10.47+0.03 and G31.41+0.31. *Astronomy and Astrophysics*, 307:599–608.

Osorio, M., Lizano, S., and D'Alessio, P. (1999). Hot Molecular Cores and the Formation of Massive Stars. *Astrophysical Journal*, 525:808–820.

Ossenkopf, V. and Henning, T. (1994). Dust opacities for protostellar cores. *Astronomy and Astrophysics*, 291:943–959.

Osterbrock, D. E. (1974). *Astrophysics of gaseous nebulae.* Research supported by the Research Corp., Wisconsin Alumni Research Foundation, John Simon Guggenheim Memorial Foundation, Institute for Advanced Studies, and National Science Foundation. San Francisco, W. H. Freeman and Co., 1974. 263.

Pantin, E. and Starck, J.-L. (1996). Deconvolution of astronomical images using the multiscale maximum entropy method. *Astronomy and Astrophysics Supplement Series*, 118:575–585.

Pascucci, I., Apai, D., Feldt, M., and Henning, T. (2003a). NACO: An Eye-Opener for Massive Star Forming Regions. In *IAU Symposium*.

Pascucci, I., Henning, T., Steinacker, J., and Wolf, S. (2003b). 2D/3D Dust Continuum Radiative Transfer Codes to Analyze and Predict VLTI Observations. *Astrophysics and Space Science*, 286:113–118.

Persson, S. E., Murphy, D. C., Krzeminski, W., Roth, M., and Rieke, M. J. (1998). A New System of Faint Near-Infrared Standard Stars. *Astronomical Journal*, 116:2475–2488.

Pfalzner, S., Henning, T., and Kley, W. (2000). Star-disc and disc-disc encounters. In *IAU Symposium*, pages 193–195.

Plume, R., Jaffe, D. T., and Evans, N. J. (1992). A survey of CS J = 7 - 6 in regions of massive star formation. *Astrophysical Journal Supplement Series*, 78:505–515.

Reid, M. J., Argon, A. L., Masson, C. R., Menten, K. M., and Moran, J. M. (1995). Synchrotron emission from the H2O maser source in W3(OH). *Astrophysical Journal*, 443:238–244.

Relke, H., Sperl, M., Hron, J., Kaeufl, H. U., Linz, H., Reimann, H., and Wagner, R. (2000). Advanced instrument control and data reduction software for TIMMI2: the new midinfrared camera for the ESO 3.6-m telescope. In *Proc. SPIE Vol. 4009, p. 440-448, Advanced Telescope and Instrumentation Control Software, Hilton Lewis; Ed.*, pages 440–448.

Robberto, M., Beckwith, S. V. W., and Panagia, N. (2002). The Infrared Emission of Circumstellar Envelopes, Dark Silhouettes, and Photoionized Disks in H II Regions. *Astrophysical Journal*, 578:897–913.

Roelfsema, P. R., Cox, P., Tielens, A. G. G. M., Allamandola, L. J., Baluteau, J.-P., Barlow, M. J., Beintema, D., Boxhoorn, D. R., Cassinelli, J. P., Caux, E., Churchwell, E., Clegg, P. E., de Graauw, T., Heras, A. M., Huygen, R., van der Hucht, K. A., Hudgins, D. M., Kessler, M. F., Lim, T., and Sandford, S. A. (1996). SWS observations of IR emission features towards compact HII regions. *Astronomy and Astrophysics*, 315:L289–L292.

Rousset, G., Lacombe, F., Puget, P., Hubin, N. N., Gendron, E., Fusco, T., Arsenault, R., Charton, J., Feautrier, P., Gigan, P., Kern, P. Y., Lagrange, A., Madec, P., Mouillet, D., Rabaud, D., Rabou, P., Stadler, E., and Zins, G. (2003). NAOS, the first AO system of the VLT: on-sky performance. In *Adaptive Optical System Technologies II. Edited by Wizinowich, Peter L.; Bonaccini, Domenico. Proceedings of the SPIE, Volume 4839, pp. 140-149 (2003).*, pages 140–149.

Rybicki, G. B. and Hummer, D. G. (1991). An accelerated lambda iteration method for multilevel radiative transfer. I - Non-overlapping lines with background continuum. *Astronomy and Astrophysics*, 245:171–181.

Sandell, G. (2000). (Sub)mm continuum mapping of NGC 6334 I & I(N). A cobweb of filaments and protostars. *Astronomy and Astrophysics*, 358:242–256.

Saraph, H. E. and Tully, J. A. (1994). Atomic data from the IRON project. IV. Electron excitation of the $^2P^0_{3/2}$-$^2P^0_{1/2}$ fine structure transition in fluorine-like ions. *Astronomy and Astrophysics Supplement Series*, 107:29–38.

Schertl, D., Balega, Y. Y., Preibisch, T., and Weigelt, G. (2003). Orbital motion of the massive multiple stars in the Orion Trapezium. *Astronomy and Astrophysics*, 402:267–275.

Siebenmorgen, R., Krügel, E., and Spoon, H. W. W. (2004). *A&A, in press.*

Simon, M., Cassar, L., Felli, M., Fischer, J., Massi, M., and Sanders, D. (1984). Star formation in the M8E region. *Astrophysical Journal*, 278:170–175.

Simon, M., Close, L. M., and Beck, T. L. (1999). Adaptive Optics Imaging of the Orion Trapezium Cluster. *Astronomical Journal*, 117:1375–1386.

Simon, M., Felli, M., Massi, M., Cassar, L., and Fischer, J. (1983). Infrared line and radio continuum emission of circumstellar ionized regions. *Astrophysical Journal*, 266:623–645.

Simon, M., Peterson, D. M., Longmore, A. J., Storey, J. W. V., and Tokunaga, A. T. (1985). Lunar occultation observations of M8E-IR. *Astrophysical Journal*, 298:328–339.

Smith, N., Bally, J., and Morse, J. A. (2003). Numerous Proplyd Candidates in the Harsh Environment of the Carina Nebula. *Astrophysical Journal Letters*, 587:L105–L108.

Sridharan, T. K., Beuther, H., Schilke, P., Menten, K. M., and Wyrowski, F. (2002). High-Mass Protostellar Candidates. I. The Sample and Initial Results. *Astrophysical Journal*, 566:931–944.

Stasinska, G. and Schaerer, D. (1997). Combined stellar structure and atmosphere models for massive stars. IV. The impact on the ionization structure of single star H II regions. *Astronomy and Astrophysics*, 322:615–623.

Stecklum, B., Brandl, B., Henning, T., Pascucci, I., Hayward, T. L., and Wilson, J. C. (2002). High resolution mid-infrared imaging of W3(OH). *Astronomy and Astrophysics*, 392:1025–1029.

Stecklum, B., Henning, T., Feldt, M., Hayward, T. L., Hoare, M. G., Hofner, P., and Richter, S. (1998). The ultracompact H II region G5.97-1.17 - an evaporating circumstellar disk in M8. *Astronomical Journal*, 115:767–776.

Steinacker, J., Bacmann, A., and Henning, T. (2002a). Application of adaptive multi-frequency grids to three-dimensional astrophysical radiative transfer. *Journal of Quantitative Spectroscopy and Radiative Transfer*, 75:765–786.

Steinacker, J., Hackert, R., Steinacker, A., and Bacmann, A. (2002b). The influence of numerical diffusion on the solution of the radiative transfer equations. *Journal of Quantitative Spectroscopy and Radiative Transfer*, 73:557–569.

Steinacker, J., Henning, T., Bacmann, A., and Semenov, D. (2003). 3D continuum radiative transfer in complex dust configurations around stellar objects and active galactic nuclei. I. Computational methods and capabilities. *Astronomy and Astrophysics*, 401:405–418.

Steinacker, J., Thamm, E., and Maier, U. (1996). Efficient integration of intensity functions on the unit sphere. *Journal of Quantitative Spectroscopy and Radiative Transfer*, 56:97–107.

Stolte, A. (2003). Mass functions and mass segregation in young starburst clusters. *Ph.D. Thesis.*

Stone, J. M., Mihalas, D., and Norman, M. L. (1992). ZEUS-2D: A radiation magneto-hydrodynamics code for astrophysical flows in two space dimensions. III - The radiation hydrodynamic algorithms and tests. *Astrophysical Journal Supplement Series*, 80:819–845.

Strömgren, B. (1939). The Physical State of Interstellar Hydrogen. *Astrophysical Journal*, 89:526.

Tapia, M., Persi, P., and Roth, M. (1996). The embedded stellar population in northern NGC 6334. *Astronomy and Astrophysics*, 316:102–110.

Thompson, R. I. (1984). Lyman and Balmer continuum ionization in zero-age main-sequence stas - Applications to the line excess phenomenon. *Astrophysical Journal*, 283:165–168.

Tokunaga, A. T. (2000). *Allen's Astrophysical quantities*. A. N. Cox, ed., Springer-Verlag, p. 143, 4th ed.

Traub, W. A. (2000). Beam Combination and Fringe Measurement. In *Principles of Long Baseline Stellar Interferometry. Edited by P. R. Lawson. Published by National Aeronautics and Space Administration, Jet Propulsion Laboratory, California Institute of Technology, Pasadena, CA, 2000, p.31.*

Turner, J. L. and Welch, W. J. (1984). Discovery of a young stellar object near the water masers in W3(OH). *Astrophysical Journal Letters*, 287:L81–L84.

Vacca, W. D., Garmany, C. D., and Shull, J. M. (1996). The Lyman-Continuum Fluxes and Stellar Parameters of O and Early B-Type Stars. *Astrophysical Journal*, 460:914–931.

van Altena, W. F. and Jones, B. F. (1972). Membership in the extremely young open cluster NGC 6530(M8). *Astronomy and Astrophysics*, 20:425–436.

van Zadelhoff, G.-J., Dullemond, C. P., van der Tak, F. F. S., Yates, J. A., Doty, S. D., Ossenkopf, V., Hogerheijde, M. R., Juvela, M., Wiesemeyer, H., and Schöier, F. L. (2002). Numerical methods for non-LTE line radiative transfer: Performance and convergence characteristics. *Astronomy and Astrophysics*, 395:373–384.

Walsh, A. J., Burton, M. G., Hyland, A. R., and Robinson, G. (1998). Studies of ultracompact HII regions - II. High-resolution radio continuum and methanol maser survey. *Monthly Notices of the Royal Astronomical Society*, 301:640–698.

Watt, S. and Mundy, L. G. (1999). Molecular Environments of Young Massive Stars: G34.26+0.15, G11.94-0.62, G33.92+0.11, and IRAS 18511+0146. *Astrophysical Journal Supplement Series*, 125:143–160.

Watt, S., Mundy, L. G., and Wyrowski, F. (1999). What Heats Hot Cores? A Study of the Positional Relationships of Hot Core Molecular Emission. *Bulletin of the American Astronomical Society*, 31:1477.

Weigelt, G., Balega, Y., Preibisch, T., Schertl, D., Schöller, M., and Zinnecker, H. (1999). Bispectrum speckle interferometry of the Orion Trapezium stars: detection of a close (33 mas) companion of Theta (1) ORI C. *Astronomy and Astrophysics*, 347:L15–L18.

Weingartner, J. C. and Draine, B. T. (2001). Dust Grain-Size Distributions and Extinction in the Milky Way, Large Magellanic Cloud, and Small Magellanic Cloud. *Astrophysical Journal*, 548:296–309.

Wilner, D. J., Reid, M. J., and Menten, K. M. (1999). The Synchrotron Jet from the H_2O Maser Source in W3(OH). *Astrophysical Journal*, 513:775–779.

Wilner, D. J., Welch, W. J., and Forster, J. R. (1995). Sub-Arcsecond Imaging of W3(OH) at 87.7 GHz. *Astrophysical Journal Letters*, 449:L73–L76.

Wink, J. E., Duvert, G., Guilloteau, S., Gusten, R., Walmsley, C. M., and Wilson, T. L. (1994). The molecular surroundings of W3(OH). *Astronomy and Astrophysics*, 281:505–516.

Wolf, S. (2001). Inverse raytracing based on Monte-Carlo radiative transfer simulations. *Astronomy and Astrophysics*, 379:690–696.

Wolf, S. (2003). MC3D-3D continuum radiative transfer, Version 2. *Computer Physics Communications*, 150:99–115.

Wolf, S., Fischer, O., and Pfau, W. (1998). Radiative transfer in the clumpy environment of young stellar objects. *Astronomy and Astrophysics*, 340:103–116.

Wolf, S., Gueth, F., Henning, T., and Kley, W. (2002a). Detecting Planets in Protoplanetary Disks: A Prospective Study. *Astrophysical Journal Letters*, 566:L97–L99.

Wolf, S. and Henning, T. (1999). AGN polarization models. *Astronomy and Astrophysics*, 341:675–682.

Wolf, S. and Henning, T. (2000). Accelerated Self-Consistent Radiative Transfer based on the Monte-Carlo Method. *Computer Physics Communications*, 132:166–188.

Wolf, S., Henning, T., and Stecklum, B. (1999). Multidimensional self-consistent radiative transfer simulations based on the Monte-Carlo method. *Astronomy and Astrophysics*, 349:839–850.

Wolf, S., Padgett, D. L., and Stapelfeldt, K. R. (2003). The Circumstellar Disk of the Butterfly Star in Taurus. *Astrophysical Journal*, 588:373–386.

Wolf, S., Stecklum, B., and Henning, T. (2001). Pre-Main Sequence Binaries with Aligned Disks? In *IAU Symposium*, page 295.

Wolf, S., Voshchinnikov, N. V., and Henning, T. (2002b). Multiple scattering of polarized radiation by non-spherical grains: First results. *Astronomy and Astrophysics*, 385:365–376.

Wood, D. O. S. and Churchwell, E. (1989). The morphologies and physical properties of ultracompact H II regions. *Astrophysical Journal Supplement Series*, 69:831–895.

Wood, K., Wolff, M. J., Bjorkman, J. E., and Whitney, B. (2002). The Spectral Energy Distribution of HH 30 IRS: Constraining the Circumstellar Dust Size Distribution. *Astrophysical Journal*, 564:887–895.

Wright, E. L., Lada, C. J., Fazio, G. G., Low, F. J., and Kleinmann, D. E. (1977). New infrared-CO source in M8. *Astronomical Journal*, 82:132–136.

Wyrowski, F., Hofner, P., Schilke, P., Walmsley, C. M., Wilner, D. J., and Wink, J. E. (1997). Millimeter interferometry towards the ultra-compact H II region W3(OH). *Astronomy and Astrophysics*, 320:L17–L20.

Wyrowski, F., Schilke, P., and Walmsley, C. M. (1999a). Vibrationally excited HC_3N toward hot cores. *Astronomy and Astrophysics*, 341:882–895.

Wyrowski, F., Schilke, P., Walmsley, C. M., and Menten, K. M. (1999b). Hot Gas and Dust in a Protostellar Cluster near W3(OH). *Astrophysical Journal Letters*, 514:L43–L46.

Yorke, H. W. (1986). The dynamical evolution of H II regions - Recent theoretical developments. *Annual Review of Astronomy and Astrophysics*, 24:49–87.

Yorke, H. W. and Sonnhalter, C. (2002). On the Formation of Massive Stars. *Astrophysical Journal*, 569:846–862.

Yusef-Zadeh, F., Shure, M., Wardle, M., and Kassim, N. (2000). Radio Continuum Emission from the Central Stars of M20, and the Detection of a New Supernova Remnant near M20. *Astrophysical Journal*, 540:842–850.

Zeng, Q., Hermsen, W., Wilson, T. L., and Batrla, W. (1984). Ammonia in the W3 region. *Astronomy and Astrophysics*, 140:169–173.

Zhang, Q. (2002). Search for Disks and Outflows in High-Mass Protostellar Candidates: Implications for Formation Mechanism. In *ASP Conf. Ser. 267: Hot Star Workshop III: The Earliest Phases of Massive Star Birth*, pages 145–152.

Acknowledgement

It is nice to have here the opportunity to thank the many people who greatly helped to the completion of this thesis.
First of all, I like to thank my advisor Prof. Thomas Henning for giving me the possibility to work on exciting astrophysical topics, for the helpful scientific discussions, trust and encouragement.
Many thanks to the collaborators of the 2D benchmark Sebastian Wolf, Jürgen Steinacker, Kees Dullemond, Thomas Henning, Gilles Niccolini, Peter Woitke and Bruno Lopez. It was a long and hard work but we managed! Sebastian, thanks also for your patient introductions to the radiative transfer simulations and for providing a flexible code to work with. Kees, I really appreciate your dedication and enthusiasm in the work.
I am grateful to Dániel Apai, Massimo Robberto, Carlos Alvarez, Leticia Martín-Hernández, Elena Puga, Ralf Launhardt, Hendrik Linz, Markus Feldt and Bringfried Stecklum for many discussions on the early (and sometimes "messy") phases of massive star formation. The reduction and interpretation of the MIDI data would not have been possible without the help of Olivier Chesneau, Christoph Leinert, Rainer Köhler and Frank Przygodda. Thank you very much!
I am in debt to Jens Rodmann and Markus Feldt who kindly translated in german the abstract of this thesis. Thanks also to the technical staff in Jena and at the MPIA, in particular to Ulrich Hiller, Frank Richter and Jürgen Weiprecht for their prompt and competent support in any computer problem.
These years in Germany gave me the chance to meet nice people who made pleasant my stay in Jena and Heidelberg. I would like to thank....
Prof. Werner Pfau, Gennaro D'Angelo, Martin Ilgner, Rainer Schraepler, Hendrik Linz and Katharina Schreyer for their warm welcome in Jena;
Klaus and Dorothea Appenroth for their example of life and generosity;
Dmitry Semenov and Roland Vavrek for their friendship;
Belen Lopez-Marti and Lina Mercado for the Italian chats, the nice weekends together and especially for the being there when I most needed;
Nadine Häring, Sebastiano Ligori, Joana Costa, Jakob Walcher, Jens Rodmann, Elena Puga, Olivier Chesneau, Carlos Alvarez, Johny Setiawan and Boris Häussler for creating a very nice and relaxing atmosphere during the coffee break at the MPIA and for the many interesting discussions on the most various topics.
Many thanks to my Italian–Hungarian family for their moral support, encouragement and understanding. Thanks Pál for your wise suggestions, Eva for your hospitality, Márton and Balázs my most reliable translators. Ringrazio i miei genitori e mia sorella per le frequenti visite in Germania, per essermi stati vicini nei momenti di difficoltá (non pochi) e per la fiducia che mi hanno sempre dimostrato. Grazie mamma per le lunghe chiacchierate al telefono anche negli orari piú strani!
A special thank to my husband Dániel Apai, my best collaborator in life and work.